Observed Relationships between Large-Scale Patterns of Variability and Atmospheric Carbon Dioxide

By
Amy K. Hawes

Department of Atmospheric Science
Colorado State University
Fort Collins, Colorado

Colorado State University

Department of Atmospheric Science

Paper No. 772

OBSERVED RELATIONSHIPS BETWEEN LARGE-SCALE PATTERNS OF VARIABILITY AND ATMOSPHERIC CARBON DIOXIDE

Submitted by

Amy K. Hawes
Department of Atmospheric Science

Colorado State University
Fort Collins, Colorado
Spring 2006

ABSTRACT

OBSERVED RELATIONSHIPS BETWEEN LARGE-SCALE PATTERNS OF VARIABILITY AND ATMOSPHERIC CARBON DIOXIDE

Atmospheric carbon dioxide (CO_2) has been steadily increasing for the last two hundred years, largely due to the burning of fossil fuels. The impact of increasing CO_2 on global climate change has been studied extensively, but uncertainties about the effects of climate change on the sources and sinks of the global carbon cycle continue to impede our abilities to accurately predict future CO_2 concentrations, and thus to fully understand the global carbon cycle.

The intent of this thesis is to examine how three major patterns of large-scale variability impact changes in atmospheric CO_2. Most previous studies on this topic have focused on the relationships between the El Niño Southern Oscillation (ENSO) and the global carbon cycle. However, far fewer studies have focused on the carbon cycle impacts of the other two major patterns of variability in the atmosphere, the so-called Northern and Southern Annular Modes. These patterns have substantial influences on surface conditions in their respective hemispheres, and thus are likely to have an impact on the flux of carbon at the Earth's surface. Furthermore, both patterns have also exhibited trends over the past few decades and therefore may play a role in driving long-term changes in atmospheric CO_2 concentrations.

We examine the impact of the Northern and Southern Annular Modes on monthly and daily mean concentrations of atmospheric CO_2 at stations around the world. The results suggest both annular modes are, in fact, coupled to variations in atmospheric CO_2 in a manner consistent with their climate impacts, but that the amplitudes of the relationships are generally small, particularly in the Southern Hemisphere. In the Northern Hemisphere, correlations and regressions suggest that the wintertime Northern Annular Mode (NAM) affects the springtime CO_2 flux in boreal land regions. On shorter time scales, advection may largely be driving variations in local CO_2 time series. In the Southern Hemisphere, the relationships are much weaker, but the results suggest that the Southern Annular Mode (SAM) is associated with variations in concentrations of CO_2 over the Antarctic Peninsula.

All findings are compared with results derived from surface flux estimates from the Atmospheric Tracer Transport Model Intercomparison Project (TransCom). The TransCom results are broadly consistent with the findings based on observations but show some unexpectedly strong relationships in regions far from the centers of action of the annular modes.

Amy Kathleen Hawes
Department of Atmospheric Science
Colorado State University
Fort Collins, CO 80523
Spring 2006

ACKNOWLEDGEMENTS

This research was supported by a graduate fellowship from the American Meteorological Society (AMS) and the United States' Department of Energy (DOE). It was also funded by NASA grant #NNG04GH53G.

Many people have helped me on the road to this paper. First and foremost, I would like to thank Dave Thompson, who has been a wonderful mentor and someone I truly look up to. Dave has given me honest advice and helpful suggestions throughout my time at CSU, and I appreciate everything he has done for me. He has really inspired me to continue in the atmospheric science field.

Scott Denning and Kevin Gurney have also provided great insight into the carbon cycle and inversion flux models, without which I would be totally lost. I know they are both very busy and I am grateful that they took some time to meet with me, because I know I learned a lot from both of them. I was also fortunate to meet Jeff Hicke and he offered good suggestions as well as his time.

I would also like to thank my group members- Laura Ciasto, Jason Furtado, Michelle L'Heureux, Kevin Grise, and Jillian L'Ecuyer. They have been wonderful resources as well as friends. Other friends have really made me feel at home in this department, including Sarah Y., Kelley, Laura S., Courtney, Gavin, and Matt. Thank you

all for your friendship, the fun times, and the many trips to Walrus for some much needed ice cream.

Finally, I would like to thank my family. My mom and dad both have characteristics that I aspire to attain. I am forever indebted to them for encouraging me to achieve my dreams and for being the most supportive parents a daughter could ask for, even though I've been in school for so long! My brother Andrew and sister Erin have also always been there for me. They are both truly wonderful friends. I feel blessed every day for such a wonderful family.

Most of all, I would like to thank my fiancé, Kevin, for being my best friend for the last 6 years, and for being my future.

TABLE OF CONTENTS

CHAPTER 1: INTRODUCTION

1.1 Overview

Atmospheric carbon dioxide (CO_2) has been steadily increasing for the last two hundred years, largely due to the burning of fossil fuels [*Intergovernmental Panel on Climate Change (IPCC),* 2001]. Because CO_2 is a greenhouse gas which selectively absorbs infrared radiation, the increasing trend will likely impact Earth's radiative energy budget, driving changes in the surface climate. Increasing the concentration of greenhouse gases in the atmosphere results in the reduction of outgoing infrared radiation to space as long as the atmosphere is colder than the surface [*Harvey*, 2000]. A doubling of atmospheric CO_2 is believed to cause a global radiative surplus of ~4 W/m^2 [*Cess et al.*, 1993], necessitating a surface temperature increase of about 1K to restore radiative balance [*Harvey*, 2000]. This temperature increase will likely induce many different feedbacks (such as water vapor, cloud, ice, and vegetation feedbacks) that influence global warming scenarios.

While the impact of increasing CO_2 on global climate change has been studied extensively, uncertainties about the effects of climate change on the sources and sinks of the global carbon cycle impede our abilities to accurately predict future CO_2 concentrations. Large-scale climate patterns, such as the Northern Annular Mode (NAM), the Southern Annular Mode (SAM), and the El Niño Southern Oscillation (ENSO) all have substantial influence on surface air temperatures (SATs) and precipitation, and thus these patterns likely have important impacts on the fluxes of CO_2.

Additionally, two of the major patterns of large-scale climate variability, namely the NAM and the SAM, have exhibited trends over the past few decades. Increasing greenhouse gases such as CO_2 are thought to influence trends in both the NAM and the SAM [*Fyfe et al.*, 1999; *Shindell et al.*, 1999, 2004; *Cai et al.*, 2003; *Toggweiler et al.*, in review]. Nevertheless, it remains unknown to what extent the climate impacts of these patterns feedback onto the global carbon cycle. Understanding fluctuations in the carbon cycle driven by these large-scale climate patterns, as well as possible feedbacks between increasing CO_2 and these patterns, is an important step in improving global warming prediction scenarios that are based on future levels of atmospheric CO_2.

In this chapter, we first give an overview of three major patterns of large-scale variability: the El Niño Southern Oscillation and the Northern and Southern Annular modes. Next, we discuss the major features of the global carbon cycle. Finally, we examine previous research concerning relationships between large-scale climate patterns and the carbon cycle using both observational measurements of CO_2 as well as inversion flux estimates.

1.2 Large-scale patterns of variability

1.2.1 The Northern and Southern Annular Modes

Two major patterns of climate variability discussed in this thesis are the Northern Annular Mode (NAM), also known as the Arctic Oscillation or North Atlantic Oscillation, and the Southern Annular Mode (SAM), also known as the Antarctic Oscillation. These patterns reflect planetary-scale fluctuations in the extratropical circulation that are characterized by zonally-symmetric, meridional "seesaws" in atmospheric mass between high latitudes and mid-latitudes [*Thompson and Wallace*,

1998, 2000]. The NAM and the SAM emerge as the leading empirical orthogonal function (EOF) of the sea level pressure, zonal wind, or geopotential height fields, as shown in Figure 1.1 (from *Climate Prediction Center, NCEP, NOAA*) [*Hartmann and Lo*, 1998; *Gong and Wang*, 1999; *Thompson and Wallace*, 2000]. The positive polarity of both the NAM and SAM is defined by westerly wind anomalies in the mid- to high-latitudes and easterly wind anomalies in subtropical latitudes and an associated anomalous poleward shift in the mid-latitude jet. The NAM is slightly less zonally symmetric than the SAM, consistent with the more pronounced land-sea contrast and topography in the Northern Hemisphere. However, the remarkable similarities in the amplitude and structure of the Northern and Southern annular modes suggest they are driven by atmospheric dynamics that transcend the contrasting land-sea differences of the two hemispheres.

A theory for the persistence and dominance of the annular modes involves the positive feedback between eddy momentum flux anomalies and zonal mean zonal flow anomalies, described as follows [*Lorentz and Hartmann*, 2001, 2003]. Baroclinic eddies tend to be generated in regions of pronounced meridional temperature gradients. As these waves grow, they propagate vertically and then equatorward in the atmosphere [*Thorncroft et al.*, 1993]. The equatorward wave propagation implies poleward eddy flux of westerly momentum in the upper troposphere, transferring momentum flux into the latitude of baroclinic eddy generation and creating upper tropospheric westerly wind anomalies at mid- to high-latitudes and easterly wind anomalies at subtropical latitudes. The Coriolis force acting on the anomalous upper tropospheric westerly wind anomalies induces an anomalous mean meridional circulation (MMC) with sinking motion

equatorward of the region of eddy generation and rising motion at higher latitudes. The induced MMC reinforces the original temperature gradient and thus successive baroclinic eddies tend to form along the same latitude band as the original wave packet. This positive feedback is thought to account for the selection of the annular modes as the leading patterns of variability in their respective hemispheres [*Robinson*, 2000; *Lorentz and Hartmann*, 2001, 2003].

Thompson and Wallace [2000] investigated the seasonality of the annular modes. The authors found that both the NAM and the SAM are present throughout the year in the troposphere but amplify with height into the stratosphere during their respective "active" seasons: Norther Hemisphere (NH) winter months for the NAM, and Southern Hemisphere (SH) late spring for the SAM. This amplification occurs when the annular modes are coupled with the Lagrangian mean meridional circulation in the stratosphere, otherwise known as the Brewer-Dobson circulation. The seasonality of the annular modes has important implications for this thesis, because when the stratosphere is coupled to the troposphere during the active seasons, changes in the stratosphere can propagate downward, potentially allowing stratospheric signals to be used as a predictive tool for surface conditions [*Baldwin and Dunkerton*, 2001].

We examine the NAM and the SAM in this thesis because they account for a substantial percentage of the variance in surface conditions, such as temperature, precipitation, and wind, that influence the carbon cycle over both the land and the oceans. As demonstrated in Figure 1.2 (left; from *Wallace*, 2000), the positive polarity of the NAM is associated with warmer than normal surface air temperatures (SATs) over Eurasian and North-American high-latitudes, and colder than normal SATs over eastern

Canada and the Middle East [*Hurrell*, 1995; *Thompson and Wallace*, 2000]. The risk of cold events, which may be accompanied by frost damage and frozen precipitation, decreases during the positive phase of the NAM over Europe, North America, and Siberia. There are also colder than normal sea surface temperatures (SSTs) in the Labrador Basin near Greenland and warmer than normal SSTs along the eastern coast of North America, throughout the mid-latitude Atlantic Ocean, and within the North Sea. Strong winds over Northern Europe and the Pacific Northwest occur more frequently and the intensity of mid-latitude storm tracks increases. Precipitation is also affected (Figure 1.2, right), with higher than normal precipitation over northern Europe and western Canada, and lower than normal precipitation over Southern Europe, the western United States, and eastern Canada [*Hurrell*, 1995; *Thompson and Wallace*, 2001].

The positive polarity of the SAM is associated with colder than normal SATs over most of Antarctica and warmer than normal SATs over the Antarctic Peninsula (Figure 1.3, left; from *Thompson and Wallace*, 2000), where enhanced westerlies increase the advection of warm oceanic air over cold land [*Thompson and Wallace*, 2000]. The advection of warmer air around the Antarctic peninsula and colder air over the Amundsen and Ross Seas causes a decrease in sea ice area near the Peninsula and an increase in sea-ice in the Amundsen and Ross Seas [*Lefebvre et al.*, 2004]. Figure 1.3 (right; from *Lovenduski and Gruber*, 2005; adapted from *Hall and Visbeck*, 2002) depicts the upper ocean processes that are associated with the positive phase of the SAM (note that these processes are based on model results only, and have yet to be observed). The intensification of the surface westerlies over the Antarctic Circumpolar current (around 60°S) induces equatorward Ekman drift at all longitudes of the Southern Ocean, while the

weakening of surface westerlies (anomalous easterlies) farther north induces poleward Ekman drift around 30°S. Due to mass continuity, anomalous upwelling of cold, nutrient rich water occurs along the Antarctic coast, while anomalous downwelling occurs around 45°S. Moreover, the anomalous divergence of water away from the Antarctic continent increases the vertical tilt of the isopycnals in the Southern Ocean so that a stronger circumpolar current is observed [*Hall and Visbeck*, 2002].

Another important point to consider is that both the SAM and NAM have exhibited trends toward positive polarity over the last few decades [*Hurrell*, 1995; *Chen and Yen*, 1997; *Thompson et al.*, 2000; *Thompson and Solomon*, 2002]. A large fraction of recent climate trends in the Northern and Southern Hemispheres are linearly congruent with the trends in the NAM and SAM, respectively. For the ~30 years between 1969-1997, ~50% of the observed JFM warming over Eurasia, nearly all of the JFM cooling over Greenland, and ~30% of the JFM warming over the NH poleward of 20°N were linearly congruent with the trend in the monthly time series of the NAM [*Thompson et al.*, 2000]. From 1969-2000, ~50% of the observed warming over the Antarctic Peninsula, ~90% of the cooling over the stations in eastern Antarctica, and much of the changes in SH westerlies were linearly congruent with the trend in the SAM index [*Thompson and Solomon*, 2002]. These trends may have influential effects on the global carbon cycle.

1.2.2 The El Niño Southern Oscillation

The other major climate pattern examined in this thesis is the El Niño Southern Oscillation (ENSO), a disruption of the coupled atmosphere-ocean system in the tropical Pacific that lasts 18-24 months and recurs on an interval of 3-7 years, generally peaking

in amplitude during NH winter months [*Trenberth*, 1976; *Rasmusson*, 1985]. As shown in Figure 1.4 (top; from *NOAA/PMEL/TAO*), during normal conditions, cold, nutrient-rich water upwells along the western boundary currents of the eastern tropical Pacific Ocean while much warmer water is found in the western tropical Pacific. The gradient in sea surface temperatures (SSTs) across the Pacific generally leads to relatively high surface pressure over the eastern tropical Pacific and low surface pressure over the western tropical Pacific, driving the trade winds westward across the Pacific Ocean. The air moistens and warms as it moves over progressively warmer water, eventually forming large convection clouds near Indonesia where the moisture is condensed out of the air. This circulation cell, also known as the Walker cell, is completed in the upper troposphere with an eastward return flow near 200 hecto-Pascals (hPa) [*Bjerknes*, 1969; *Rasmusson*, 1985; *Philander,* 1990].

During El Niño conditions (Figure 1.4, bottom), the westward trade winds weaken, causing a decrease in the east-west thermocline gradient and leading to anomalously high SSTs in the eastern Pacific Ocean. The eastward shift in warmer SSTs causes the Walker cell to contract eastward, giving rise to more subsidence over Indonesia and thus less rainfall in that region [*Bjerknes*, 1969]. The change in the location of the atmospheric heat source in the tropics drives changes in the global circulation, allowing ENSO to affect climate far from the tropical Pacific [*Hoskins and Karoly*, 1981; *Horel and Wallace*, 1981]. La Niña conditions are marked by anomalies in the opposite sense.

1.3 The Global Carbon Cycle

Thus far, we have noted that the annular modes and ENSO impact surface climate over the ocean and land of their respective hemispheres. In this section, we review the different sources and sinks of atmospheric CO_2 in order to better understand how climate variability may affect both oceanic and biospheric CO_2 fluxes. Figure 1.5 (from *IPCC,* 2001) illustrates the estimated sources, sinks, and reservoirs of CO_2 due to natural processes (top) and anthropogenic impacts (bottom). The main balance of natural processes (top) occurs between the photosynthesis and respiration of the terrestrial biosphere and the air-sea flux. These fluxes are nearly balanced each year, but imbalances due to factors such as ENSO or the annular modes can affect atmospheric CO_2 concentrations for years or centuries. Over longer time-scales, other fluxes contribute to the natural carbon cycle, such as the export of dissolved organic carbon by rivers, weathering of calcium carbonate, and volcanism [*IPCC*, 2001].

The anthropogenic impacts on the carbon cycle (bottom) include fossil fuel burning and land-use change. In general, atmospheric CO_2 concentrations have risen from about 280 parts per million (ppm) in the year 1800 to about 380 ppm today [*IPCC,* 2001]. This increase, unprecedented for at least the last 20,000 years, can be mostly attributed to fossil fuel burning (the rest of the increase is due to land-use change). However, of the 5.4 ± 0.3 gigatons of carbon (GtC) released by fossil fuel burning on average every year, only about half (3.3 ± 0.1 GtC yr^{-1}) is observed to remain in the atmosphere; the rest must be taken up by the ocean and the terrestrial biosphere [*IPCC,* 2001]. The exact allocation into oceanic uptake and biospheric uptake remains uncertain,

but it appears that the "missing" carbon is divided nearly equal between them [*Sarmiento and Gruber*, 2002].

1.3.1 Ocean Fluxes

In the ocean, air-sea flux exchange (which occurs on the order of 90 GtC yr^{-1}) occurs when there is an imbalance in CO_2 partial pressure across the air-sea interface, and is dependent upon solubility and the gas transfer velocity (a strong non-linear function of wind speed) [*Wanninkhof and McGillis*, 1999]. The uptake of anthropogenic CO_2 into the oceans can occur via the solubility pump or the biological pump. CO_2 solubility increases with decreasing SSTs such that net cooling of SSTs leads to CO_2 uptake and net warming leads to CO_2 outgassing [*IPCC*, 2001]. This temperature dependence implies that CO_2 uptake occurs at cold, high-latitude zones where bottom waters are formed, causing CO_2 to sink with the dense cold water and be transported as part of the thermohaline circulation. However, the rate of vertical exchange between the surface and ocean interior is on the order of 1000 years [*Sarmiento and Gruber*, 2002]. The biological pump occurs when short-lived oceanic micro-organisms transform CO_2 from the atmosphere and nutrients from seawater into soft organic tissues and calcareous skeletons; when these organisms die, their soft tissue and skeletal material sink into lower depths so that CO_2 is drawn down into the deep ocean. This process causes the dissolved inorganic carbon (DIC) concentration to be higher at depth than at the surface, so diffusion transfers DIC upward to balance the cycle [*Harvey*, 2000; *Feely et al.*, 2001]. Both the solubility and biological pumps, as well as gas transfer velocity, are considered potentially important mechanisms in regards to the affect of large-scale climate patterns on oceanic CO_2 flux.

1.3.2 Terrestrial Biosphere Fluxes

Ocean fluxes may account for some of the uptake of anthropogenic CO_2, but inversion models suggest that over half of the "missing" anthropogenic carbon sink must occur in the Northern Hemisphere, and that most likely, this NH sink is due largely to the terrestrial biosphere [*Tans et al.*, 1990]. In the biosphere, plants convert atmospheric CO_2 to carbohydrates during photosynthesis and release CO_2 during respiration (either by the plant itself or by organisms in the soil that help to decompose organic matter) [*Harvey*, 2000]. While the mechanisms are somewhat uncertain, uptake of anthropogenic CO_2 is thought to occur via CO_2 fertilization, nutrient fertilization, land-use change, or climate change. CO_2 fertilization is the idea that the observed rising levels of atmospheric CO_2 should enhance plant photosynthesis and growth and thus allow an uptake of CO_2 into the biosphere [*Joos et al.*, 2002], although the effectiveness of this process in the real world is debatable [*Caspersen et al.*, 2000; *Oren et al.*, 2001]. Nutrient fertilization, particularly nitrogen deposition, can also enhance plant growth and lead to CO_2 uptake [*Vitousek et al.*, 1997; *Bergh et al.*, 1999]. Land-use change, particularly over North America, almost certainly plays a role in CO_2 uptake due to the re-growth of forests in farmlands that have been abandoned as more people retreat to cities, as well as the re-growth of trees in fire suppression areas [*Pacala et al.*, 2001]. Finally, changes in climate factors such as solar radiation, temperature, and available water can affect plant photosynthesis, respiration, and decomposition [*IPCC*, 2001]. For example, recent warming trends in the NH high-latitude boreal regions appears to have led to longer growing seasons there, perhaps enhancing the CO_2 sink [*Keeling et al.*,

1996; *Myneni et al.*, 1997; *Lucht et al.*, 2002]. Changes in climate factors induced by the three major patterns of variability is the main mechanism considered in this thesis.

1.3.3 Atmospheric CO_2

Atmospheric CO_2 is non-reactive and fairly well-mixed over constant latitude due to the slowness of the sources and sinks of CO_2 compared to the time it takes the atmosphere to mix thoroughly (~7-10 days around a given latitude band; on the order of months for north-south transport). However, there are variations about the mean in CO_2 that may depend on local sources and sinks or on changes in advection. In this thesis we focus on these deviations, or anomalies, of atmospheric CO_2.

Atmospheric CO_2 has a strong seasonal cycle that is mainly due to the drawdown into plants in the NH spring when photosynthesis exceeds respiration and the subsequent release in NH autumn when the opposite occurs [*Machta*, 1972; *Dettinger and Ghil*, 1998; *Harvey*, 2000]. A component of the seasonal cycle may also be due to the seasonality in the oceanic carbon cycle caused by SST variations. The seasonal cycle has the greatest amplitude over NH land regions and the lowest amplitude in the SH, where it is out of phase with the NH seasonal cycle by ~6 months [*Heimann et al.*, 1989].

1.4 Previous studies

1.4.1 Relationships between climate patterns and observed atmospheric CO_2

Most previous studies have focused on the relationship between ENSO and the global carbon cycle. Initial studies by Bacastow and coworkers [*Bacastow*,1976; *Bacastow et al.*, 1980] suggested that negative atmospheric CO_2 concentration anomalies at Mauna Loa led warm ENSO (El Niño) events by 6 months. This finding does not meet the requirement of a causal relationship, because we expect large-scale circulation

changes to drive the change in atmospheric CO_2 level and not vice versa. In other words, it is not likely that the anomaly in CO_2 concentration drives ENSO since CO_2 fluctuations are on the order of 1 ppm out of a total concentration of about 380 ppm. *Bacastow* [1976] reasoned that changes in circulation phenomenon such as ENSO should affect the rate of change of the CO_2 concentration, or the derivative (here, called the tendency of the concentrations), instead of the concentration level itself. The author found that roughly 2.5 months after a warm ENSO event occurs, CO_2 tendencies at Mauna Loa are anomalously high. Several studies find that an initial decrease in atmospheric CO_2 tendencies occurs near the beginning of a warm ENSO event followed by a large increase in CO_2 tendencies several months later [*Keeling et al.*, 1989; *Elliot et al.*, 1991; *Conway et al.,* 1994; *Rayner et al.*, 1999]. The initial decrease is thought to be due to the reduction in oceanic upwelling during a warm ENSO event, leading to a decrease in outgassing of CO_2 to the atmosphere [*Feely et al.*, 1987, 1999; *Winguth et al.*, 1994]. The subsequent increase in the CO_2 tendency is thought to be a result of warmer temperatures and decreased precipitation following a warm ENSO event, leading to higher soil and plant respiration and an increase in forest fires, and thus a terrestrial biosphere source of CO_2 [*Keeling and Revelle*, 1985; *Siegenthaler*, 1990; *Yang and Wang*, 2000]. Biomass burning in particular is thought to be responsible for the large increase in CO_2 to the atmosphere after a warm ENSO event [*Russell and Wallace*, 2005, in review].

Far fewer studies have been published concerning relationships between the Northern and Southern Annular Modes and atmospheric CO_2. In theory, a high-index NAM would imply a stronger polar vortex, leading to less cold outbreaks over high-

latitude Northern Hemisphere land regions and warmer temperatures over much of Siberia, northern Europe, and parts of Canada, allowing an advance of spring budburst and a longer growing season and thus anomalously higher annual CO_2 drawdown by the terrestrial biosphere [*Russell and Wallace*, 2004]. While there are several observations of a lengthening of the growing season in the Northern Hemisphere in the last few decades [*Keeling et al.*, 1996; *Myneni et al.*, 1997; *Lucht et al.*, 2002], consistent with the observed trend toward the high-index polarity of the NAM [*Hurrell*, 1995; *Thompson et al.*, 2000], *Russell and Wallace* [2004] observed no trend in the annual drawdown of CO_2. *Schaefer et al.* [2002] used a land surface model of leaf- and canopy-level photosynthesis and ecosystem respiration and found that NH temperature effects due to the NAM on net ecosystem exchange (NEE, or the net flux of CO_2 from the terrestrial biosphere) dominated over precipitation effects. The authors also noted that temperature advection due to the NAM does not seem to significantly influence NEE variability except in northern Europe (because competing effects between respiration and photosynthesis were observed to cancel the effect of the NAM everywhere else). *Buermann et al.* [2003] found spatially coherent patterns in the correlations of the springtime vegetation index (the Normalized Difference Vegetation Index) to the wintertime NAM index, showing enhanced greenness in Eurasia and decreased greenness in eastern North America following a high-index NAM event.

Due to lack of nearby land regions with significant vegetation in the Southern Hemisphere, the SAM is thought to impact atmospheric CO_2 via air-sea flux exchange. The mechanism is unclear, but one major hypothesis is described here for the high index SAM scenario [*Lovenduski and Gruber*, 2005]: increased westerly winds south of 50°S

lead to anomalous equatorward Ekman drift and increased upwelling along the Antarctic coast, thereby increasing the CO_2 outgassing and resulting in an anomalous source of atmospheric CO_2 by the ocean south of 50°S. Moreover, enhanced westerly winds south of 50°S lead to more air-sea gas exchange [*Wanninkhof and McGillis*, 1999]. However, this anomalous source may be diminished due to the anomalously cold and iron-rich water being drawn up to the surface, which increases CO_2 solubility as well as phytoplankton productivity. Above 50°S, anomalous easterly winds drive poleward Ekman drift, increasing the convergence and downwelling of surface water near 50°S and reducing upwelling, leading to an anomalous CO_2 sink. There are opposing influences in this region as well, as the increased downwelling causes deeper mixed layers and increased light limitation, which reduces phytoplankton productivity, and tends to reduce CO_2 uptake [*Hall and Visbeck*, 2002; *Lovenduski and Gruber*, 2005]. Clearly, there are many factors involved in the process. The cancellation between mechanisms implies that changes in the CO_2 flux driven by the SAM may be hard to observe [*Lovenduski and Gruber*, 2005].

On much longer time scales, recent model results by *Toggweiler et al.* [submitted for review] suggests that the observed reduction in CO_2 during previous ice ages [*Delmas et al.*, 1980] is a result of equatorward-shifted westerlies in the SH that allow more respired CO_2 to accumulate in the deep ocean. Likewise, interglacial time periods like the present have poleward-shifted westerlies (in agreement with the trend toward the positive polarity of the SAM) that lead to more upwelling along the Antarctic coast that flushes respired CO_2 out of the deep ocean and into the atmosphere. A positive feedback is thought to occur due to the increased CO_2 being associated with warmer temperatures,

leading to a further poleward shift in the westerlies and more upwelling. Note that this theory agrees with the hypothesis described above [*Hall and Visbeck*, 2002; *Lovenduski and Gruber*, 2005], even though this theory is based on total CO_2, rather than CO_2 at a particular latitude, and much longer time scales.

Another climatic influence on CO_2 that we briefly consider is the impact of volcanic eruptions. Major eruptions in the last half century include Mt. Agung (March 1963), Mt. Fuego (October 1974), El Chichón (April 1982), and Mt. Pinatubo (June 1991). In general, a decrease in atmospheric CO_2 is observed after a volcanic eruption. This decrease is hypothesized to be caused by either: (a) increased aerosols from eruption lead to a reduction in global solar radiation, causing a cooling of surface temperature and thus a reduction in plant respiration, and ultimately leading to CO_2 uptake by the biosphere [*Jones and Cox*, 2001], or (b) increased aerosols from eruption lead to an increase in diffuse radiation, enhancing photosynthesis, and again leading to CO_2 uptake by the biosphere [*Gu et al.*, 2003]. Potentially, both mechanisms play some role in the observed decrease in CO_2.

1.4.2 Relationships between climate patterns and inversion model flux estimates of CO_2

Inverse modeling of CO_2 flux estimates using atmospheric tracer transport models is a useful way of approximating regional carbon sources and sinks. The Atmospheric Tracer Transport Model Intercomparison Project (TransCom) seeks to compare multiple transport models in order to asses how differences in the various models affect the inversion results and to estimate carbon sources and sinks at regional scales [*Gurney et al.*, 2002, 2003, 2004]. The results from this project indicate a consistent carbon sink over the continents of the Northern Hemisphere that is distributed relatively evenly across

North America, Europe, and Asia. The tropical land regions, as well as the tropical Eastern Pacific Ocean, are sources of carbon to the atmosphere; however, the tropical regions are found to be poorly constrained. The Southern Ocean is found to be an overall sink of CO_2 but may be a source during SH winter [*Roy et al.*, 2003].

Other individual inverse models have examined the variability and trends in the CO_2 flux estimates [*Bousquet et al.*, 2000; *Rodenbeck et al.*, 2003]. One result is that the variability of terrestrial fluxes is nearly double the variability of ocean fluxes, which suggests that terrestrial processes dominate global CO_2 flux anomalies. A weak trend towards larger oceanic uptake with time is observed, which is consistent with the theory that ocean uptake will be enhanced when atmospheric CO_2 increases [*Le Quere et al.*, 2003]. No long-term trend over land is found.

Some inversion models have been used to verify relationships between the interannual variability of CO_2 sources and sinks and ENSO [*Rayner et al.*, 1999; *Bousquet et al.,* 2000; *Rodenbeck et al.*, 2003]. These studies find that land fluxes dominate the interannual variability of global CO_2 fluxes at a pace set by the ENSO cycle, with the exception being the 2-3 years following the Mt. Pinatubo eruption [*Rodenbeck et al.*, 2003]. The largest flux differences between El Niño and La Niña events tend to occur in tropical land regions. As expected from observations, there are large fluxes from the biosphere to the atmosphere during warm ENSO events with fluxes in the opposite sense during cold ENSO events [*Rodenbeck et al.*, 2003].

Little research has been done on the relationship between CO_2 flux estimates from inversion models and the SAM or NAM. *Patra et al.* [2005] recently examined the correlations between inversion flux estimates and the NAM from 1994-2001. The

authors found a significant positive correlation between the boreal North American flux anomalies and the NAM, and a significant negative correlation between the boreal Asia flux anomalies and the NAM, at a lag of 5 months for each correlation.

1.5 Objectives

While a decent understanding of the impact of ENSO on the global carbon cycle exists, much less research has been done to understand the relationship of the carbon cycle to the NAM or the SAM. In this work, we examine the observed relationships between monthly mean and weekly variations in atmospheric CO_2 concentrations and the Northern and Southern Hemisphere Annular Modes. We also consider relationships with the El Niño Southern Oscillation as a means of comparison with previous findings. The observed relationships are compared with results derived from TransCom surface flux estimates. Chapter 2 describes the data that was used and gives background information about the analysis techniques. Chapter 3 explores the relationships between monthly mean CO_2 concentrations and tendencies and the three climate patterns discussed above. The concept of "departure" data is also introduced. Chapter 4 examines daily CO_2 concentrations and the potential influence of advection on the relationship between the carbon cycle and CO_2. Chapter 5 first gives background information on TransCom monthly mean flux estimates, and then investigates the capability of these estimates to reveal relationships with climate patterns. Chapter 6 includes a summary of the findings and presents possibilities for future research.

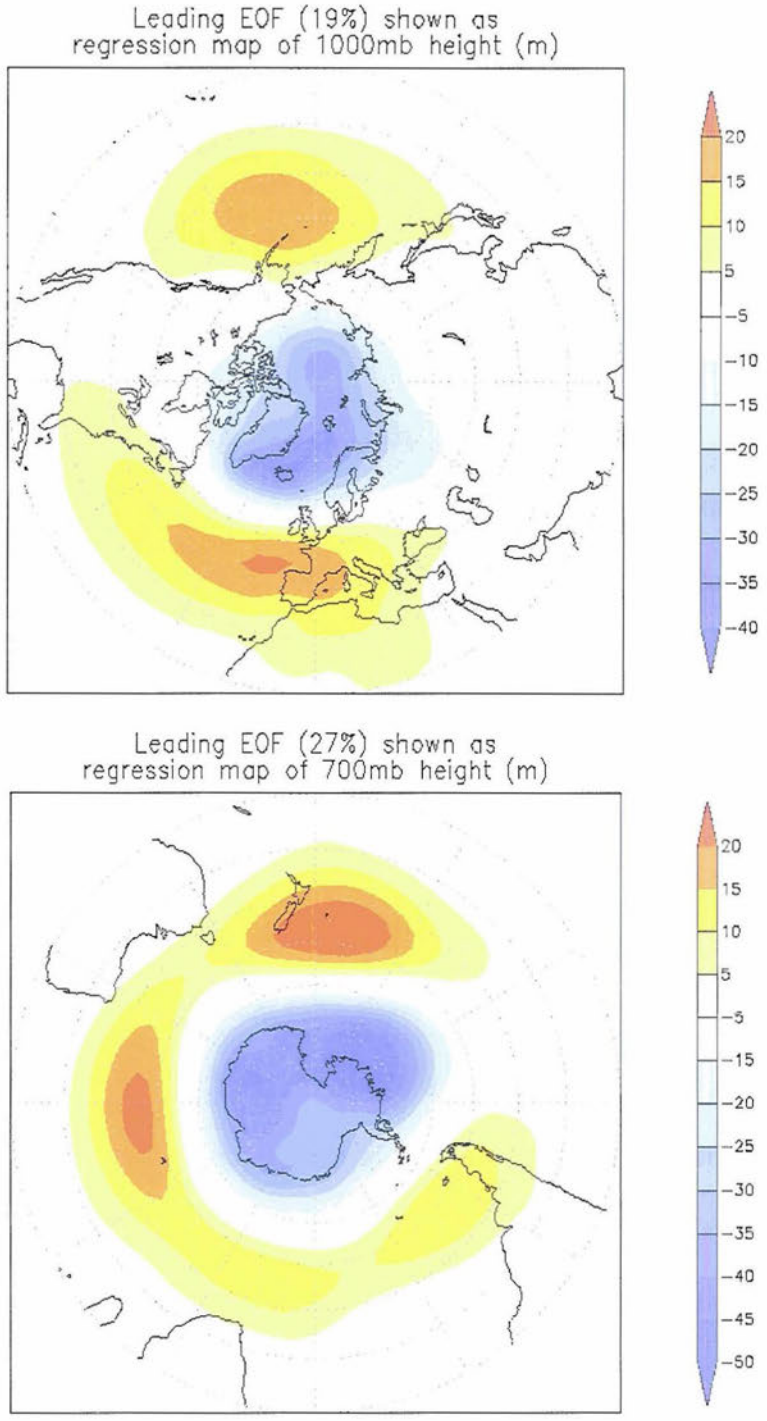

Figure 1.1 (top) The Northern Annular Mode (NAM), defined as the leading empirical orthogonal function (EOF) of monthly mean 1000 mb heights poleward of 20°N from 1979-2000. The percent variance explained is 19%. (bottom) The Southern Annular Mode (SAM), defined as the leading EOF of monthly mean 700 hPa height poleward of 20°S for 1979-2000. The percent variance explained is 27% (from Climate Prediction Center, NCEP, NOAA).

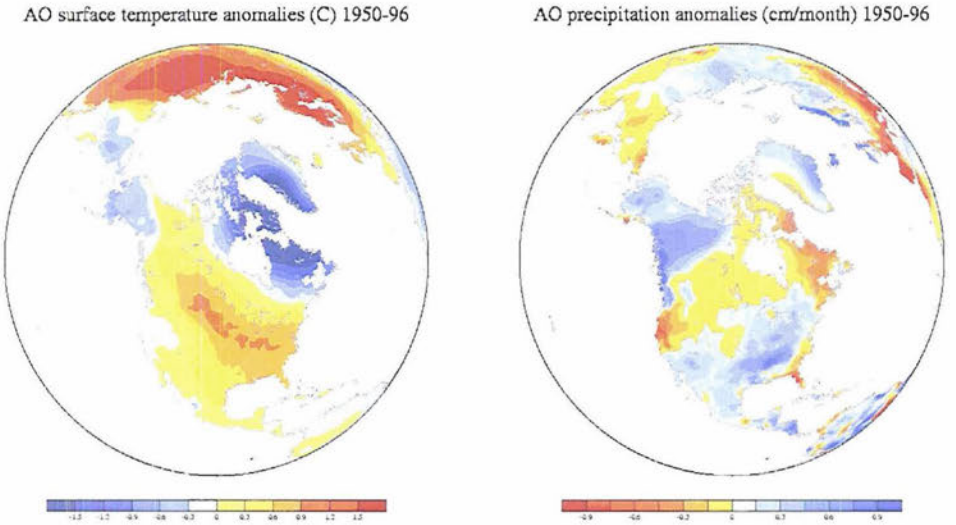

Figure 1.2 (left) NAM surface temperature anomalies (C) for 1950-1996. (right) NAM precipitation anomalies (cm/month) for 1950-1996 (from *Wallace*, 2000).

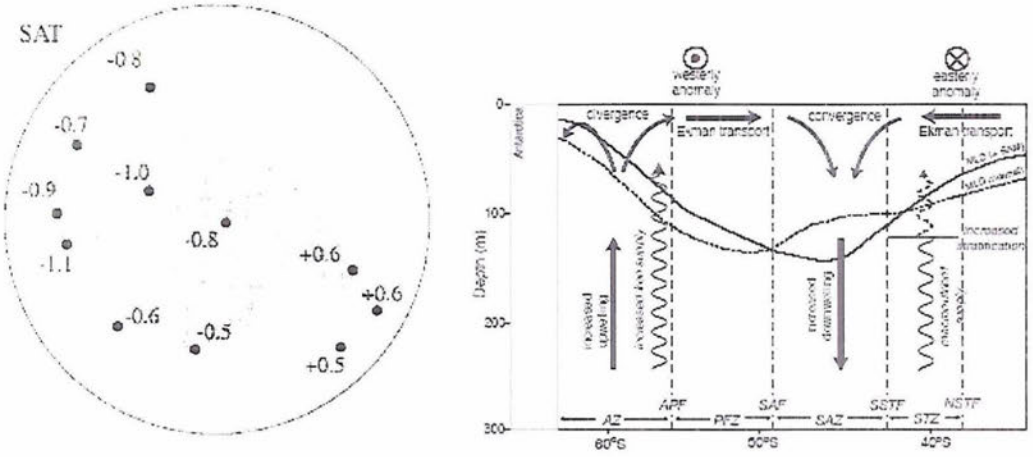

Figure 1.3 (left) Surface air temperature (K) regressed upon the SAM for all calendar months (from *Thompson and Wallace*, 2000). (right) Schematic diagram of upper ocean processes associated with the positive phase of the SAM (from *Lovenduski and Gruber*, 2005; adapted from *Hall and Visbeck*, 2002).

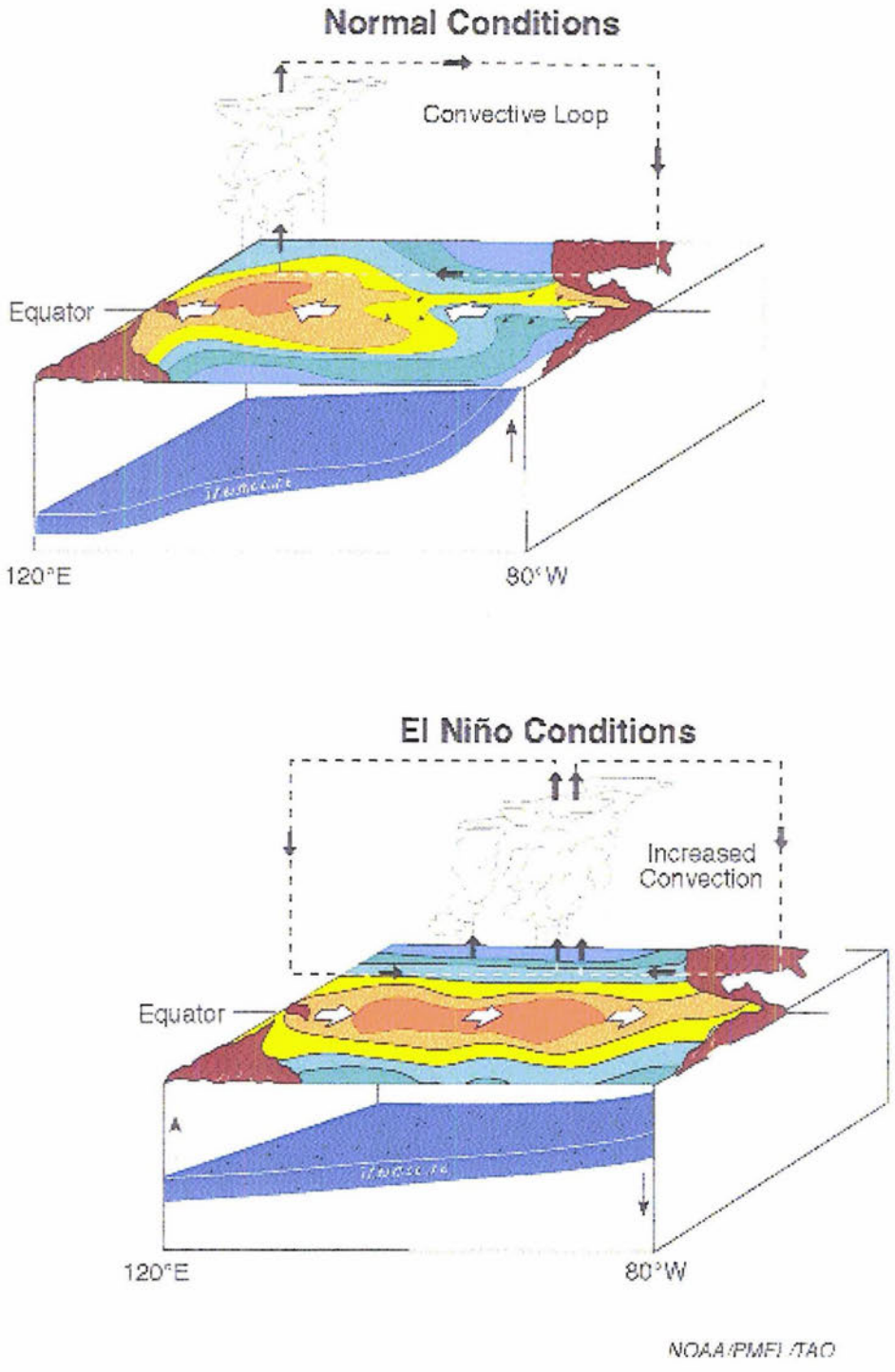

Figure 1.4 (top) Normal conditions in the tropical Pacific Ocean from longitudes 120°E to 80°W. (bottom) El Niño conditions in the tropical Pacific Ocean (120°E-80°W) (from NOAA/PMEL/TAO).

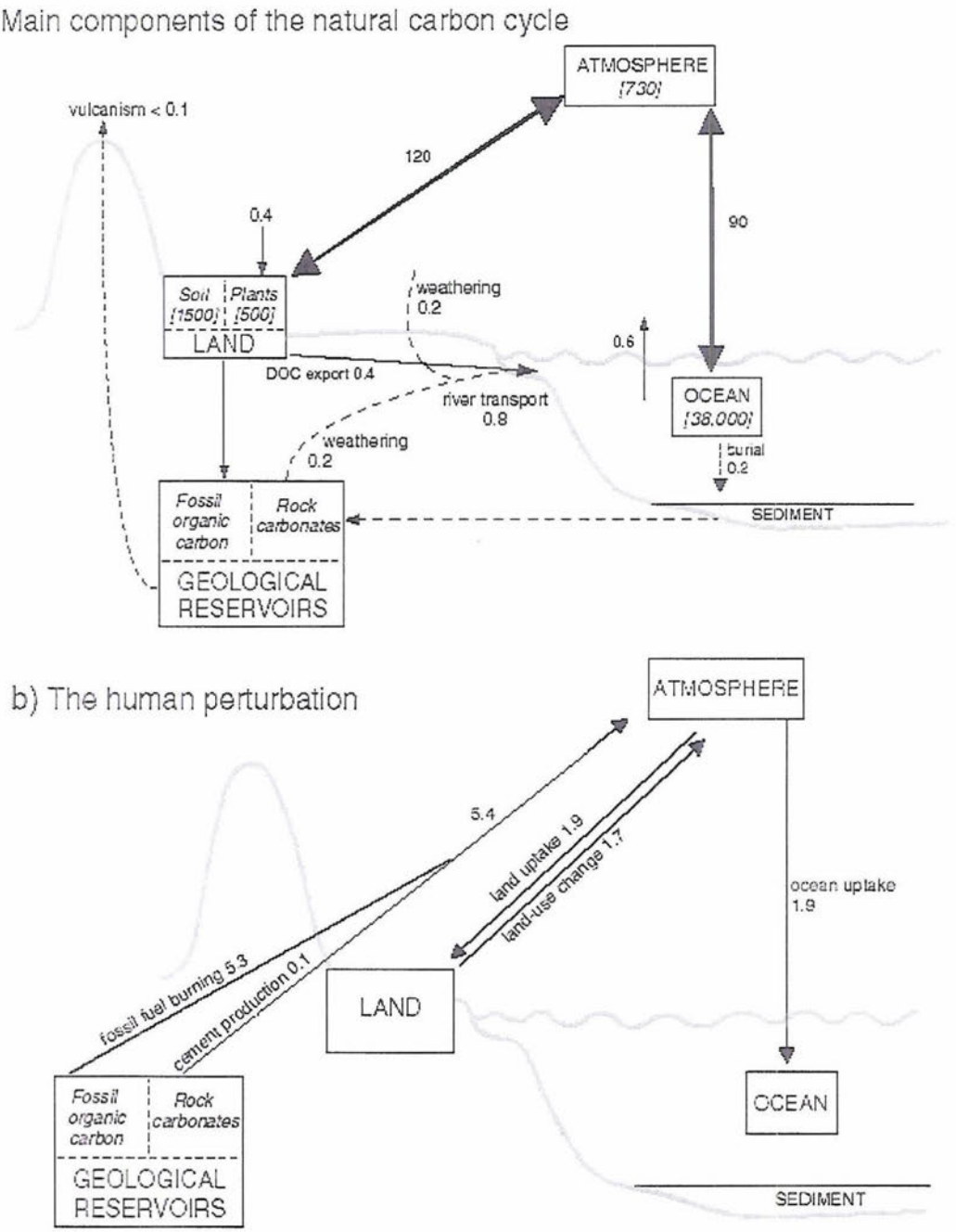

Figure 1.5 The reservoirs (GtC) and fluxes (GtC/yr) of the global carbon cycle. (top) The main natural components of the carbon cycle. The thick arrows indicate the most important fluxes in terms of CO_2 balance of the atmosphere: gross primary production and respiration of the biosphere and air-sea flux. Smaller arrows indicate additional natural fluxes, which are important on longer time scales. (bottom) The anthropogenic components of the carbon cycle (from *IPCC* , 2001).

CHAPTER 2: DATA AND METHODOLOGY

In this chapter, we describe the observational data and model flux estimates used in the analysis of the relationships between atmospheric CO_2 and the three patterns of variability introduced in Chapter 1. Furthermore, we describe the various statistical techniques utilized in this thesis.

2.1 Data

2.1.1 CO_2 Measurements from Station Records

We use observational atmospheric CO_2 mixing ratios (in parts per million) measured by the Climate Monitoring and Diagnostics Laboratory (CMDL) at the National Atmospheric and Oceanic Administration (NOAA) in Boulder, Colorado. The CMDL stations that measure CO_2 (as well as methane, carbon monoxide, and other chemical compounds) make up the Carbon Cycle Cooperative Global Air Sampling Network, and include over 50 stations around the world as shown in Figure 2.1 (from *NOAA CMDL*, 2003). The locations of the stations tend to be biased toward the NH, and there is a lack of stations in the interior of most of the continents. There are several stations located on remote islands (where it is easier to measure CO_2 unaffected by local sources and sinks), while some samples are collected on ship tracks across the Pacific and Atlantic Oceans.

The measurements are made using a non-dispersive infrared absorption technique in air samples collected in glass flasks at each station [*Komhyr et al.*, 1983]. The air

samples can be collected by one of two methods: flushing and then pressurizing the glass flasks with a pump, or opening a stopcock on an evacuated flask [*Conway et al.*, 1994]. Two flasks are filled during each sampling event. The flasks are then sent back to Boulder to be analyzed in a uniform manner. The measurement of CO_2 in these flasks is made relative to reference standards whose CO_2 mixing ratio is determined with high precision and accuracy. These standards are traceable to the World Meteorological Organization (WMO) CO_2 mole fraction scale adopted for CO_2 monitoring [*Thoning et al.*, 1987; *Zhao et al.*, 1997].

Sampling frequencies are approximately weekly for most of the stations used in this thesis. Monthly means are also produced by CMDL for each site by averaging all valid measurement results that share a sample date and time and then extracting values at weekly intervals from a smooth curve fitted to the averaged data [*Thoning et al.*, 1989]. These weekly values are then averaged for each month to obtain the monthly means. If the difference between the pair of flasks collected during each sampling event is greater than 0.5 ppm, the data are flagged. Flagged data are excluded from the curve fitting process, and some stations lack too much data for the monthly mean to be calculated. If there are 3 or more consecutive months without data, the monthly means are not calculated for these months and the time series will be marked by "Not A Number" (NaN) instead of a value for these months [*NOAA CMDL*, 2003].

In our analysis of the daily CO_2 data (Chapter 4), we average all data from the same day to create daily averages. All flagged data have been removed. Note that in some cases, these flagged outliers may be valid measurements that represent local anthropogenic sources or nearby biospheric fluxes [*NOAA CMDL*, 2003]. Measurement

accuracy based on repeated analyses of CO_2 in reference gas cylinders is ~0.2 ppm and measurement precision based on repeated analysis of the same air is ~0.1 ppm [*NOAA CMDL*, 2003]. Average agreement between pairs of flasks throughout the global network is ~0.2 ppm [*NOAA CMDL*, 2003].

We focus on the station data from Mauna Loa (MLO), Palmer Station (PSA), and Barrow, Alaska (BRW), described in more detail in Table 2.1. Other stations were also examined, but no station with missing values comprising more than 50% of the time record was used. For these three stations, we look at the time period 1979-2002 because it is the longest continuous period for all 3 stations (some data gaps still exist in this time frame). Note that not all stations have records dating back to 1979, as many stations were introduced in the 1990s. We also mention that corrections have been made to CO_2 mixing ratios measured on the flask analysis apparatus that was used from July 1987 to April 1998, detailed in the NOAA CMDL update notes [*NOAA CMDL*, 2003].

Although data for MLO are available back to 1959 from the Scripps Institute of Oceanography (SIO), we do not use that data in this analysis because we want to maintain consistency and not mix data from two different research groups (the two groups have similar measurement methods but not identical selection criteria for data representative of "background" air [*Elliot et al.*, 1991]). Moreover, we chose to use CMDL because they had measurements at more stations; SIO, for example, does not make measurements at PSA.

2.1.2 GLOBALVIEW CO_2 Product

We use the GLOBALVIEW product to find the global mean CO_2 concentration and tendency anomalies, as well as the global mean linear trend (whose calculation is

discussed later in this chapter). The GLOBALVIEW product, which is coordinated and maintained by the Carbon Cycle Greenhouse Gases Group (CCGG) of the NOAA CMDL, is based on atmospheric CO_2 measurements made by institutions and organizations around the world [*GLOBALVIEW-CO_2*, 2004]. The measurements are smoothed, interpolated, and extrapolated to produce records with evenly spaced time increments; however, the actual data may be lost in this manipulation [*Masarie and Tans*, 1995]. Gaps in the data are filled by extrapolating measurements from the marine boundary layer.

The major goal of the GLOBALVIEW product is to integrate many measurements from different research groups in a consistent manner in order to facilitate use with carbon cycle modeling studies [*GLOBALVIEW-CO_2*, 2004]. Temporal discontinuity and spatial sparseness in the sampling site network make modeling the sources and sinks of carbon much more difficult, so GLOBALVIEW was created in order address these issues. Most of the laboratories contributing to GLOBALVIEW report their data relative to the WMO CO_2 mole fraction scale and calibrate their calibration scales based on the same reference standards. A few laboratories, however, have their own reference scales or have not maintained a routine recalibration schedule, which may lead to inconsistencies in the data. Fortunately, the majority of participating laboratories agree to within ~0.2 ppm [*GLOBALVIEW-CO_2*, 2004].

The major differences between the station CO_2 measurements and GLOBALVIEW are that (1) GLOBALVIEW is based on measurements from multiple research groups, whereas we use station data from CMDL only, and (2) GLOBALVIEW has been manipulated to get "synchronized" time steps at every location while the station

data has widely varying times of measurement at each station. For this thesis, we use the station data for most of the analysis because it has been less manipulated than GLOBALVIEW and because we typically focus on regional rather than global climate impacts; however, we use GLOBALVIEW for finding the global trend and global anomalies because the data has already been interpolated into a convenient global grid with equal temporal and spatial scales throughout the data record.

In this thesis, we only use the GLOBALVIEW reference marine boundary layer matrix, which runs from January 1st, 1979 to January 1st, 2004. This matrix contains CO_2 mixing ratios as a function of time and sine of latitude and may be missing a significant amount of information from the actual data due to data manipulation [*GLOBALVIEW-CO_2*, 2004]. This manipulation arises from the fact that there are not CO_2 measurements at every location and time period, so a lot of data interpolation must be performed to derive this matrix. The time column of the reference matrix is composed of 48 "weekly" time steps per year, while the space columns are composed of 41 even intervals of 0.05 sine of latitude from 90°S to 90°N [*GLOBALVIEW-CO_2*, 2004].

2.1.3 TransCom CO_2 Flux Estimates

In the Atmospheric Tracer Transport Model Intercomparison Project 3 (TransCom 3), the world is discretized into 11 land regions (by vegetation type) and 11 ocean regions (by circulation features) shown in Figure 2.2 [*Gurney et al.*, 2002, 2003, 2004]. A tracer with unit flux is released from each region during each month into a set of 13 different transport models. A time series of tracer concentrations at each observing station can then be produced. Using Bayesian synthesis inversion methods [*Enting*, 2002] and the "observed" CO_2 concentrations and their uncertainties (from

GLOBALVIEW CO_2, see previous section), the unknown surface flux time series for each region is found. The TransCom 3 project seeks to generate these time series of CO_2 flux (Gt C yr^{-1}) and average over all models, in order to measure the sensitivity of the flux estimates to differences in the models as well as to estimate regional sources and sinks of CO_2 and their uncertainties. Monthly flux estimates are available from 1980 to 2002 [*Baker et al.*, 2005].

Annual mean, seasonal, or interannual inversions can be performed. In this thesis, we focus on the interannual flux estimates. Interannual results are sensitive to the particular stations used, and spurious jumps may occur if new stations are introduced in the middle of a model run. Therefore, a particular network of stations with continuous measurements is chosen for a given time period. For the case of 1980-2002, 23 stations qualify as being continuously operating [*Gurney et al.*, 2005]. Of course, any uncertainties resulting from data manipulation in the GLOBALVIEW product will carry over to the inversion.

Fossil fuels are pre-subtracted from measured concentrations, so that the flux estimates lack the strong positive trend of the observational data and the estimated fluxes reflect net exchange with the terrestrial biosphere and ocean. The spatial pattern of the fossil fuel emissions field is based on an interpolation in time between the 1990 and the 1995 fields [*Baker et al.*, 2005]. Also pre-specified are seasonally-varying (but spatially constant) air-sea gas exchange and seasonally-varying flux due to terrestrial photosynthesis and respiration [*Gurney et al.*, 2002]. The models do not include interannual variability (IAV) of the transport fields in order to reduce computational time, so some error exists due to assuming that the models are driven by the same winds and

vertical mixing every year. Since there is no IAV in the transport fields, the IAV in the estimated fluxes is due solely to the IAV in the observed CO_2 concentrations [*Baker et al.*, 2005]. More explicit information on how these flux estimates are derived can be found in *Baker et al.* [2005].

2.1.4 The ENSO, NAM, and SAM Indices

The ENSO index is based on SSTs and is calculated by the NOAA/National Weather Service (NWS) National Centers for Environmental Prediction (NCEP) Climate Prediction Center (CPC). In this thesis, we use the Niño 3.4 index, which is a measure of the SST anomalies about the long-term mean (1971-2000) for the region 5° North to 5° South latitude and 170° to 120° West latitude.

The monthly and daily NAM and SAM indices used in this thesis are also calculated by the NOAA/ NWS NCEP CPC and are based on geopotential height. The geopotential height field at different pressure levels is obtained from the National Centers for Environmental Prediction/National Center for Atmospheric Research (NCEP/NCAR) reanalysis dataset with a horizontal resolution of 2.5° x 2.5°. The reanalysis is composed of data from land surface, ship, rawinsonde, satellite, and aircraft measurements which are all quality controlled and then assimilated in a data assimilation system [*Kalnay et al.*, 1996]. Geopotential height is one of the variables of the reanalysis product that is heavily influenced by observations and hence more reliable; it is also available on both daily and monthly time scales. Besides being used by the CPC for calculating the NAM/SAM index, the NCEP/NCAR reanalysis geopotential height product is also used in this thesis during composite analysis in Chapter 4.

To calculate the NAM (SAM) index, the seasonal cycle is first removed from the 1000-hPa (700-hPa) geopotential height field and this gridded data is weighted by the square root of the cosine of the latitude in order to provide equal area weighting for the covariance matrix [*NOAA CPC*]. Then the leading Empirical Orthogonal Function (EOF) is found for these weighted geopotential height anomalies poleward of 20° latitude for the Northern (Southern) Hemisphere [*NOAA CPC*]. The daily and monthly NAM (SAM) index is obtained by projecting the daily and monthly mean 1000-hPa (700-hPa) height anomaly field onto the leading EOF of 1000-hPa (700-hPa) geopotential height field. We standardize all of the indices by subtracting the long-term mean of the time series and dividing by the long-term standard deviation.

2.1.5 Other data

We also use the 1-degree resolution gridded Normalized Difference Vegetation Index (NDVI) data from the National Aeronautics and Space Administration (NASA) Advanced Very High Resolution Radiometer (AVHRR) from 1981-2001 [*Tucker et al.*, 2005]. The NDVI quantifies the amount of photosynthetically absorbed radiation, or the concentration of green leaf vegetation, over land regions. The index is calculated as the difference in reflectance between the AVHRR near-infrared bands and visible bands divided by the sum of these two bands [*Tucker*, 1980]. The NDVI can be sensitive to band calibrations or to natural changes in column water vapor or atmospheric aerosols, such as for time periods following volcanic eruptions. Frequent cloud cover also produces numerous gaps in the data [*Tucker et al.*, 2005]. We remove the seasonal cycle from the data in our analysis.

2.2 Methodology

2.2.1 Data Preparation

For analyses involving the monthly mean CMDL station CO_2 data, we first remove the global mean GLOBALVIEW linear trend from the raw data. Then, the seasonal cycle is removed by (1) creating long-term average values for each calendar month and (2) subtracting the resulting climatological mean seasonal cycle from every year in the data. Analyses using the daily station CO_2 data are done in a similar manner, although in this case we first remove flagged data and then average any data from the same sample date. The linear trend is also removed from the daily station data by subtracting the GLOBALVIEW global mean trend, interpolated to have the same resolution as the station CO_2 data. The climatological mean seasonal cycle is found by averaging the same days from each year (for example: January 1st, 1979 with January 1st, 1980). As some days only have one or two values over the course of 23 years, individual daily values in the resulting annual cycle may be strongly impacted by sampling variability. In order to minimize this impact, we apply a 15-point running mean filter (chosen because it provides the optimal balance between reducing spurious data and maintaining resolution) to the climatological mean seasonal cycle before subtracting it from the de-trended daily CO_2 data, which results in the daily CO_2 anomaly time series. The monthly CO_2 flux estimates from TransCom have no major trend to remove, but the seasonal cycle is removed in the same manner as the monthly CMDL station CO_2.

For the remainder of this section we discuss the statistical tools of correlation and regression, used frequently in this thesis, as well as composite analysis. We also describe how the global mean linear trend is calculated from the GLOBALVIEW-CO_2 reference matrix and how the 12-month tendency is calculated.

2.2.2 Linear Regression and Correlation

Linear regression involves minimizing the sum of the squared differences between the data "y" and a linear estimate of the data based on values of "x":

$$\hat{y} = a_1 * x + a_0$$

where $\hat{y}$ is the estimate of the data and x is the predictor. The variable "x" is assumed known with precision; in the case of finding a trend, x generally corresponds to time. The parameters a_1 and a_0 are found by minimizing the error Q, defined as the sum of the squares of $\hat{y}$(estimate) $- y$ (actual):

$$Q = \sum_{i=1}^{N} (\hat{y} - y_i)^2 = \sum_{i=1}^{N} (a_1 * x_i + a_0 - y_i)^2$$

This process is called linear least-squares fitting. The slope of the resulting best fit line to the data is called the regression coefficient and corresponds to:

$$a_1 = \frac{\overline{x' y'}}{\overline{x'^2}}$$

where $()' = () - \overline{()}$, so that the primes denote variations about the mean (shown with the overbar). The regression coefficient is thus equal to the covariance between x and y divided by the variance of x. When x is standardized, its variance is 1, so that the regression of y onto x is just the covariance between x and y. Standardizing x allows the units of the regression coefficient to be "change in y per standard deviation of change in x."

The correlation coefficient is closely related to the regression coefficient, and provides a dimensionless measure of the "goodness of fit" between x and y. The correlation coefficient ranges from -1 to 1 and is given as:

$$r = \frac{\overline{x'y'}}{\sqrt{\overline{x'^2} * \overline{y'^2}}}$$

r^2 corresponds to the fraction of variance explained by a linear least squares fit between the variables x and y. The correlation and regression coefficients are related by the equation:

$$a_1 = r * \frac{\sqrt{\overline{y'^2}}}{\sqrt{\overline{x'^2}}}$$

such that the regression coefficient of y on x is equal to the correlation coefficient multiplied by the ratio of standard deviations of x and y. If x and y are both standardized, then the regression and correlation coefficients are equal. The major conceptual difference between correlation and regression is that correlation shows the significance of a relationship between two variables while regression gives its amplitude.

The significance of a correlation is found using the t-statistic:

$$t = \frac{r\sqrt{N_{eff} - 2}}{\sqrt{1 - r^2}}$$

where N_{eff} is the number of independent samples. To determine the effective sample size N_{eff}, which takes into account the persistence of the data, we refer to *Bretherton et al.* [1999]:

$$N_{eff} \sim N * \frac{1 - a_1 a_2}{1 + a_1 a_2}$$

where N is the number of data points, "a_1" is the lag-one autocorrelation of the first time series, and "a_2" is the lag-one autocorrelation of the second time series. As persistence increases, the effective sample size decreases.

2.2.3 Compositing

The concept behind composite analysis is to isolate a signal in the data from the background noise by averaging the data in relation to an event. For example, in our analysis we use the ENSO index, choosing only those events when the index exceeds +/- 1 standard deviation. Then we find the corresponding CO_2 flux estimates for the times corresponding to those events and compute the mean. This analysis may tell us whether there is a significant difference between the mean CO_2 flux for high index events and the mean CO_2 flux for low index events. We also composite the 500-hPa height field for times when CO_2 measurements exceed +/- 1 standard deviation.

The significance of composites is generally assessed using the t-statistic for the difference in means:

$$t = \frac{\overline{x_1} - \overline{x_2}}{\sigma\sqrt{\frac{1}{N_1} + \frac{1}{N_2}}} \text{ where } \sigma^2 = \frac{N_1 s_1^2 + N_2 s_2^2}{N_1 + N_2 - 2}$$

where σ^2 is the pooled variance, N_1 (N_2) is the sample size of sample 1 (2), and s_1 (s_2) is the sample standard deviation of samples 1 (2). Monte Carlo tests, which involve randomly picking out subsets of the data and re-doing the analysis using only the subset of the data and then repeating this process many times, can also be performed to test the robustness of the composite result.

Compositing and regression are two different analysis techniques that reveal nearly the same information about the data, as demonstrated in Figure 2.3. For a set of measurements (red dots), regression measures the slope of the best fit line to the data (black line), whereas compositing groups the data y according to values of x (in this case, for x<-1 and x>+1, shown in blue circles). Finding the difference between the means of

these two groups will give a sense of how much y varies between extremes in x. Regression will also indicate the amplitude of the relationship, but will include all data points, not just those beyond some threshold. Regression maps and composite maps will both reveal the same features, although regression maps will be in units of change in y per change in x whereas composite maps won't have physically meaningful units.

2.2.4 Removing the global mean GLOBALVIEW trend via linear regression

Removing trends involves linear regression in the sense that linear least-squares fitting is being used to find the best fit line to a temporal trend in the data. The best fit line is the fraction of the variable y that is linearly congruent with the time record x. Subtracting this fitted line, which represents the temporal trend, from the original data y removes any component in y that is linearly congruent to x. The residual data will thus have no trend over time.

A time series can be fitted to any polynomial equation (such as $\hat{y} = a_2 * x^2 + a_1 * x + a_0$), but in our analysis we mostly use the simple linear case (e.g. a_2=0) except where otherwise noted. The type of fit used does make small differences in the results, but generally not enough to alter the results significantly (a notable exception occurs in Chapter 4). In order to maintain consistency throughout the analysis, we use the GLOBALVIEW reference marine boundary layer matrix [*GLOBALVIEW-CO_2*, 2004] in order to compute a global mean linear trend. This trend is used to remove the trends from all station data, under the assumption that the observed trend is due largely to fossil fuels and should be well-mixed across the globe. While this assumption may not be true for stations close to industrial areas where fossil fuels are produced, the particular trend used does not seem to impact our results in a significant way.

To get the monthly global trend from the daily GLOBALVIEW CO_2 reference matrix product, which is a time by space matrix, we first cosine weight and average the "weekly" CO_2 matrix. This results in the global mean time series. The global mean trend is found by finding the linear best fit line to this time series. If we remove this trend as well as the seasonal cycle, we are left with global mean anomalies, which are used in the calculation of the departure CO_2 (refer to Chapter 3). The "weekly" fit (48 weeks per year) and "weekly" anomalies are each averaged every 4 weeks to produce monthly versions of these time series.

2.2.5 12-month CO_2 tendency

The 12-month CO_2 tendency is a derivative of the monthly CO_2 concentration time series, calculated by subtracting the value 6 months prior to time 't' from the value 6 months after time 't'. For example, to calculate the June 1980 tendency, we subtract the January 1980 value from the January 1981 value. To find the change in ppm per year, the resulting value is divided by 12 months.

We use the 12-month tendency rather than the month-to-month tendency because the signal-to-noise ratio is small in the case of month-to-month tendencies. Thus, the 12-month tendency essentially serves as a "smoother" to the month-to-month tendencies. Since a large fraction of the variability in the CO_2 concentrations is at lower (interannual) frequencies, it makes sense to examine the rate of change of concentrations between years, rather than between individual months. The daily CO_2 concentrations will be examined to look at higher frequency variability in Chapter 4.

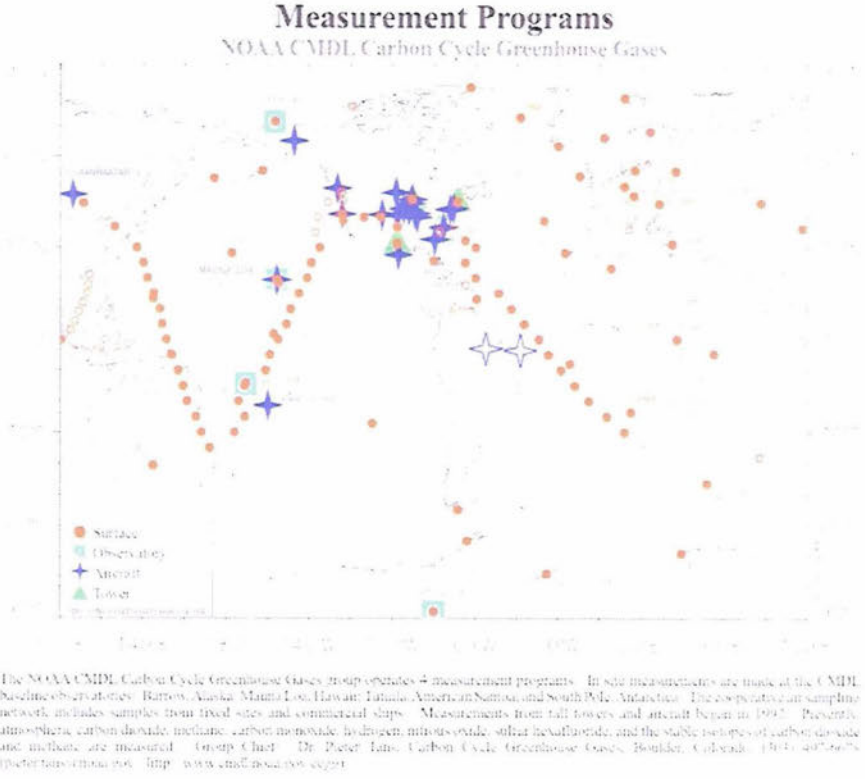

Figure 2.1 NOAA CMDL stations. Description included in the figure.

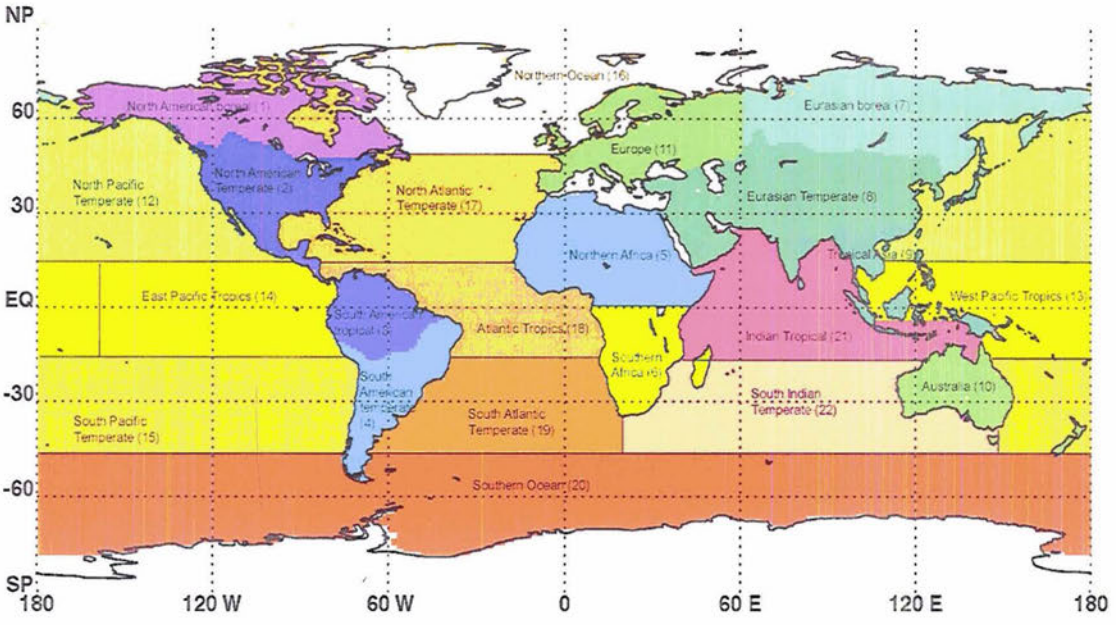

Figure 2.2 The 22 TransCom regions.
http://transcom.colostate.edu/TransCom_3/transcom_3.html

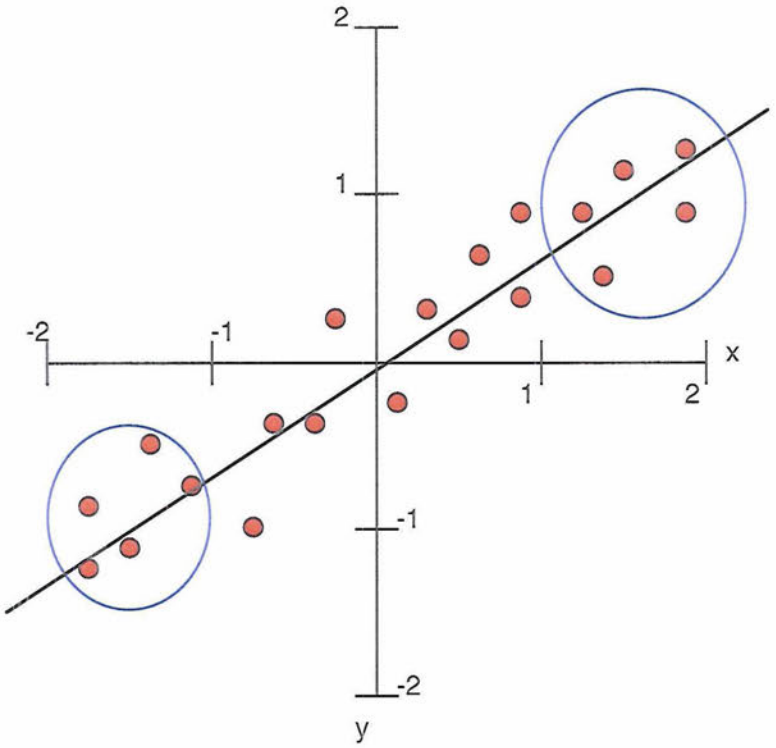

Figure 2.3 Differences between compositing and regression.

Table 2.1 CMDL stations used most frequently in this thesis (from *Conway et al.*, 1994). *Elevation above mean sea level.

Station	Latitude	Longitude	Elevation* (m)	Site Type
MLO	19°32' N	155°35'W	3397	Barren volcanic mountain slope
PSA	64°55' S	64°00' W	10	Barren island seashore
BRW	71°19' N	156°36' W	11	Arctic coastal seashore

CHAPTER 3: MONTHLY MEAN CO_2 CONCENTRATIONS AND RELATIONSHIPS TO ENSO, NAM, and SAM

This thesis applies multiple methods of statistical analysis in order to find physical relationships between large-scale patterns of climate variability and variations in atmospheric CO_2. The purpose of this chapter is to apply simple statistical techniques such as correlation and regression in order to examine relationships between three climate patterns and monthly mean CO_2 concentrations and tendencies measured at CMDL stations. Although links between atmospheric CO_2 and ENSO have already been well-studied, we reconsider these relationships here in order to provide a sense of the reliability of the results for the other climate patterns. We also introduce the concept of "departure" CO_2, or the departure of CO_2 tendency anomalies from global mean CO_2 tendency anomalies.

We note that the correlations found here are based on pure statistics and give no information about the physical basis of the relationship. Therefore, although we hypothesize potential physical mechanisms throughout this thesis, we recognize that a lag correlation will not reveal whether a relationship is due to a localized change in flux (where the lag may represent the time it takes for the change in climate to impact a change in CO_2 concentration), or to the transport of CO_2 from another region that is more strongly affected by the climate pattern (where the lag would indicate the length of time required for transport), or some combination of local fluxes and advection.

3.1 Relationships between monthly mean CO_2 concentrations and patterns of large-scale variability

3.1.1 Monthly mean CO_2 concentrations and ENSO

This section explores the correlations between monthly mean atmospheric CO_2 concentrations at Mauna Loa and ENSO, and compares the results to previous research. Mauna Loa (MLO) station records of atmospheric CO_2 provide a reasonable approximation of the global mean CO_2 concentrations because the station is isolated on an island far from major anthropogenic emissions and high on a mountain above the trade wind inversion [*Machta*, 1972]. Thus, the CO_2 concentration records at Mauna Loa can be useful for examining the relationships to the global ENSO signal. This analysis was also performed using various other station CO_2 data (such as the South Pole), but similar results were found and are not included here.

Monthly mean CO_2 concentrations are dominated by an increasing trend thought to be mostly caused by the burning of fossil fuels [*IPCC*, 2001]. Figure 3.1a shows the "raw" monthly mean CO_2 concentrations (solid line) at MLO with an obvious positive trend, increasing from about 335 ppm in 1979 to almost 375 ppm in 2003. Also apparent is the strong seasonal cycle caused by the uptake of atmospheric CO_2 by the terrestrial biosphere in the NH spring and the subsequent release in the NH autumn. The global, linear trend (discussed in Chapter 2) is also shown in Figure 3.1a (dashed line), and when this trend is subtracted from the "raw" monthly mean concentrations, the seasonal cycle becomes the dominant feature (Figure 3.1b). The seasonal cycle at Mauna Loa has a peak-to-peak amplitude of ~6 ppm, which is smaller than the amplitude of the seasonal cycle over NH land regions but larger than the amplitude over the SH high-latitudes.

After the seasonal cycle is removed from the Mauna Loa CO_2 record, we are left with the so-called CO_2 concentration anomalies (Figure 3.1c). The peak-to-peak amplitudes of the anomalies are on the order of ~2 ppm, and clearly have some variability on interannual timescales. Several visual observations about the relationships between major ENSO events and volcanic eruptions (marked on the figure) and the CO_2 anomalies can be made. In general, an anomalous increase in CO_2 concentrations occurs several months after a warm ENSO event, such as those in 1986-1987, 1997-1998, and 2002-2003. This observation agrees with previous findings demonstrating that atmospheric CO_2 tends to increase after a warm ENSO event due to increased temperatures and decreased precipitation, leading to increased plant and soil respiration, more frequent forest fires, and thus a biospheric source of CO_2 [*Keeling and Revelle*, 1985; *Siegenthaler*, 1990; *Yang and Wang*, 2000]. The 1983-84 and 1991-92 El Niño were exceptions to this observation, as CO_2 concentrations remained below normal following these events. However, both these warm ENSO events were preceded by volcanic eruptions. El Chichón erupted in April 1982, while Mt. Pinatubo erupted in June 1991, leading to decreased atmospheric CO_2 concentrations for almost 3 years after each eruption, which may have dominated any ENSO effects in the respective time frames. The decreased CO_2 after each eruption agrees with the theory that increasing volcanic aerosols will either cool surface temperatures and reduce plant and soil respiration, and/or lead to more diffuse radiation and enhance photosynthesis [*Jones and Cox*, 2001; *Gu et al.*, 2003].

In order to more quantitatively examine the relationship between ENSO and CO_2 concentration anomalies, we find the lag correlation between the ENSO index and the

CO_2 concentration anomalies at Mauna Loa for 1979-2002. Figure 3.2 (top) shows the same CO_2 concentrations shown in Figure 3.1(c), only standardized (solid line). Also, the standardized ENSO index is shown for comparison (dashed line), with peaks greater than 1 standard deviation representing the warm ENSO events marked in Fig. 3.1(c). Again, warm ENSO events visually appear to lead a positive CO_2 concentration anomaly. However, when the lag correlation is calculated (Figure 3.2 (bottom)), the best correlation occurs with negative CO_2 concentration anomalies leading a warm ENSO event by 4 months. Note that this correlation is not significant at the 95% level, according to the *t*-statistic. Previous studies found that CO_2 at MLO leads ENSO by 6 months, which agrees to some extent with our result considering the different time frames and data used [*Bacastow*,1976; *Bacastow et al.*, 1980; *Rayner et al.*, 1999]. This result is difficult to interpret physically since we expect large-scale circulation changes to drive the change in atmospheric CO_2, and not vice versa.

3.1.2 Monthly mean CO_2 concentrations and the SAM and NAM

Lag correlations between CO_2 concentration anomalies and the NAM and the SAM were also calculated. Stations nearest to areas likely affected by the NAM and the SAM were chosen, since we assume that these patterns have the largest influence nearest their respective centers of action. Therefore, CO_2 concentration data from Palmer Station, Antarctica (PSA), was chosen to look for relationships to the SAM, and CO_2 data from Barrow, Alaska (BRW), for relationships to the NAM. While other stations in similar latitudes were also examined with similar results, these two stations had some of the longest and least interrupted data sets in each hemisphere from 1979-2002.

The PSA CO_2 concentration anomalies and the SAM index are shown in Figure 3.3 (top). Clearly, the SAM index (dashed line) has much more high-frequency variability than the ENSO index shown in Fig. 3.2 (top). It is also much more difficult to visually observe relationships between the two time series. The lag correlation (Figure 3.3 (bottom)) confirms that little relationship exists between the PSA concentration anomalies and the SAM for any lag. The best correlation occurs with CO_2 concentrations leading the SAM by 6 months, but no correlations are significant at the 95% level.

The BRW CO_2 concentration anomalies and the NAM index are shown in Figure 3.4 (top). Once again, the NAM index has much more high-frequency variability than the ENSO index. The BRW CO_2 and the NAM seem to share more variability in time than the PSA CO_2 and the SAM, but relationships are still not obvious by looking at the time series. The lag correlation (Figure 3.4 (bottom)), however, does show a significant correlation with CO_2 leading the NAM by 1 month, suggesting that a positive NAM event follows an increase in CO_2 concentration at BRW. However, we expect a positive lag between the NAM and CO_2 due to the time between NH winter (when stronger NAM events tend to occur) and spring budburst, so this correlation is difficult to explain physically.

3.2 Relationships between monthly mean CO_2 tendencies and patterns of large-scale variability

As explained by *Bacastow* [1976], changes in circulation phenomenon, such as ENSO or the annular modes, should affect the rate of change of the CO_2 concentration instead of the concentration level itself. For this reason, we examine the 12-month

derivative of the concentration anomaly curve (what we term the "tendency") for the remainder of this chapter.

3.2.1 Monthly mean CO_2 tendencies and ENSO

Figure 3.5 (top) illustrates the CO_2 tendency time series for Mauna Loa (solid line) as well as the ENSO index time series (dashed line) for 1979-2002. Compared to Figure 3.2 (top), the peaks in CO_2 tendency clearly match up with the peaks in the ENSO index, except after the El Chichón and Mt. Pinatubo eruptions. This stronger relationship is also apparent in the lag correlation (Figure 3.5 (bottom)), where a 95% significant correlation occurs with ENSO leading the CO_2 tendency by 3-7 months. Bacastow [1976] found ENSO leading the derivative of CO_2 concentrations by 2.5 months, but as mentioned previously, we are using entirely different time frames of the data, so some differences are expected. Note that the best correlation occurs with CO_2 tendency leading ENSO by 12 months, but this correlation most likely arises from the inherent periodicity of ENSO on the order of 18-24 months.

The lag relationship suggests that a warm ENSO event is associated with a CO_2 flux to the atmosphere (defined as a positive flux) ~5 months later. This result agrees with the concept that ENSO will drive changes in temperatures and precipitation that eventually affect plant photosynthesis and respiration, leading to an overall biosphere source of CO_2 following a warm ENSO event. Some amount of time is also required for the tropical influences of ENSO on CO_2 to be transported poleward (which is why we find, for example, a longer time lag relationship between ENSO and the South Pole CO_2 tendencies than between ENSO and the MLO tendencies). The fact that we get a physically plausible result suggests that using the CO_2 tendency rather than CO_2

concentrations may provide more realistic results when looking for relationships to the NAM and the SAM.

3.2.2 Monthly mean CO_2 tendencies and the SAM and NAM

The CO_2 tendency at Palmer Station (solid line) and the SAM index (dashed line) time series are shown in Figure 3.6 (top), and the lag correlation between these two time series is shown in Figure 3.6 (bottom). Note that the CO_2 tendency still has noticeably lower frequency variability than the SAM index, most likely due to the influence of ENSO. The best correlation occurs when the CO_2 tendency leads the SAM by 4 months, but no correlations are significant at the 95% level. Significant correlations also do not occur with CO_2 tendencies at other SH stations. Unfortunately, no new information is obtained by using the tendency rather than the concentration in this case.

Examining the relationship between the NAM and the CO_2 tendency at Barrow reveals a more robust result. Figure 3.7 shows the two time series from 1979-2002 (top) and their lag correlation (bottom left). In this case, the NAM leads the CO_2 tendency by 6 months, which agrees remarkably well with the theory that the NAM's influences on northern boreal climate will take several months to affect the carbon cycle through changes in the terrestrial biosphere. The correlations are significant at the 95% level for the period of 4-7 months after the NAM event, and suggest that a positive NAM event is associated with an anomalous uptake of atmospheric CO_2 about 4-7 months later. This uptake is hypothesized to be due to less frequent cold outbreaks over the boreal regions following a positive NAM, leading to an earlier growing season [*Russell and Wallace*, 2004]. We note that this relationship may be due to either local fluxes (caused by local changes in climate at BRW) or to the advection of lower-than-normal CO_2 air into BRW

(caused by anomalous biospheric uptake of CO_2 likely upwind of BRW). Either way, for this particular hypothesis to hold, a lag time of several months is expected due to the time it takes the NAM to influence the start of the spring budburst through climate changes.

One thing to recognize is that these correlations are based on the full, year-round time series. To focus on the effects of the wintertime NAM only, we took an average of the January, February, and March (JFM) values for every year (so there is only one value per year) from 1979-2002. This new time series is then correlated to tri-monthly averages of the BRW CO_2 tendency, and the results are shown in the bottom right of Figure 3.7. The wintertime NAM is negatively correlated at the 95% significance level to the July/August/September (JAS) mean CO_2 tendency, which agrees with our findings based on the full year of data. The fact that the correlations peak in JAS rather than April/May/June (AMJ) may be due to the later onset of spring at higher northern latitudes, as well as the potential delay between the initial plant growth and a noticeable change in CO_2 mixing ratio. We also note that only the JFM NAM (not the AMJ or JAS NAM) has significant correlations with the tri-monthly means of the BRW CO_2 tendency.

A few other NH stations were also examined in order to test the robustness of this result. Cold Bay, Alaska (CBA) JAS CO_2 tendency also had significant correlations with the JFM NAM. However, Alert, Canada (ALT) had significant correlations only in JFM and AMJ. ALT is located at ~84°N, where plant growth may be minimal, so other processes (such as advection) may be influencing the correlations with the JFM NAM in this location. A few stations (Station "M", Shemya Island) had no significant correlations with the JFM NAM. The fact that the BRW and CBA CO_2 tendencies, which are from stations located fairly close to each other, have similar correlations and

lags to the NAM is encouraging, but we recognize that there are a lot of factors that may influence the relationship with the NAM at each NH station.

3.2.3 Removing the ENSO signal from the CO_2 tendency

The ENSO signal tends to dominate the low-frequency variability of the CO_2 tendency time series from stations around the world. Removing this signal may help to illuminate relationships between the annular modes and the CO_2 tendencies that were previously hidden. The ENSO signal is removed by linearly regressing the CO_2 tendency onto the ENSO index at the best lag, and then subtracting this "fit" from the original CO_2 tendency time series. Note that the NAM and SAM may also derive a fraction of their variability from ENSO; however, for our purposes, we assume that the annular modes and ENSO are independent of one another.

Figure 3.8 (top) shows the SAM index and the new PSA CO_2 tendency with ENSO removed at the best lag via linear fitting (the best lag occurs with ENSO leading the PSA CO_2 tendency by 5 months). Thus, this time series is now completely uncorrelated to the ENSO index at a lag of 5 months. The lag correlation between the SAM and the PSA CO_2 tendency is shown in Figure 3.8 (bottom). The correlation is significant, which is an improvement over Figure 3.6 (bottom) when ENSO was included, and the best correlation occurs at lag zero. It is possible that we are observing the effects of advection: a positive SAM would increase westerlies, potentially blowing in CO_2-rich air and causing an increase in CO_2 flux at PSA almost immediately. This possibility will be explored in Chapter 4 of the thesis.

This correlation may also be a result of CO_2 fluxes, since higher wind speeds and anomalous upwelling associated with the SAM are thought to lead to CO_2 outgassing,

although it's difficult to assess how long it takes for the SAM to affect these factors (however, it seems unlikely to be instantaneous). Whatever the physical explanation, we should remember that we arrived at this result only after some manipulation, which could imply that either the relationship between the PSA CO_2 tendency and the SAM is almost non-existent or non-linear, or else it's too weak to be observed when the time record is still dominated by volcanic events.

Removing the ENSO signal from the BRW CO_2 tendency, or any NH station CO_2 tendency, does little to enhance the statistical relationships between these tendencies and the NAM, and thus are not shown here. This may be because the NH boreal stations have more local forcing from the terrestrial biosphere than the SH stations, and so the NAM signal is already fairly strong.

3.3 Departure CO_2 tendency

3.3.1 Definition and concept of "departure" tendency

In the last section, the ENSO signal was removed by linearly fitting the ENSO index to the CO_2 tendency and subtracting from the original CO_2 tendency time series. Just removing ENSO did seem to suggest some relationship between the SAM and CO_2 tendency. However, the volcanic signal remained in the CO_2 tendency time series, possibly causing the relationship between the annular modes (in particular, the SAM) and the CO_2 tendency to be blurred.

With this problem in mind, we derived the concept of the "departure" CO_2 tendency. The idea is that every CO_2 station record has low-frequency variability that is dominated by what we term the "global mean", composed mostly of ENSO and volcanic events. Note that "global mean" is a misnomer as it is based only on available station

records, which are located mostly in the NH and over land. Figure 3.9 (a) demonstrates the large fraction of variability in the CO_2 tendency time series explained by the global mean, particularly at SH stations where local influences are small. In this figure, we compare the PSA CO_2 tendency to the global mean CO_2 tendency (solid line; see Chapter 2 for method of computation). Clearly, the global mean comprises the majority of the signal; however, the deviations about this mean may be the result of a more regional driving mechanism, the SAM. All other stations in the SH are also dominated by the global mean signal (not shown).

Therefore, to isolate the regional variations in the CO_2 tendency time series, we subtract the global mean from the CO_2 tendency to create a new time series that is a "departure" from the global mean. This new time series will be referred to as the departure tendency for the remainder of the thesis, and can be viewed as variations in local CO_2 relative to the global mean CO_2.

3.3.2 Relationships between the departure CO_2 tendency and the SAM

Figure 3.9 (b) shows the standardized PSA departure CO_2 tendency (solid line) and the SAM index (dashed line) for 1979-2002. While a correlation between the two time series is hard to visualize, it can be observed that the two time series have variability on similar time scales. The PSA departure CO_2 tendency has a peak-to-peak amplitude of ~0.1 ppm/year (not shown).

In performing this analysis, we assume that the effects of the SAM on the carbon cycle will be strongest closer to the SAM's centers of action and decrease farther equatorward. For this reason, we examine the average departure CO_2 tendency for stations south of 30°S (7 stations) and for stations from 0-30°S (7 stations), with the

expectation that the stations farther south will be more strongly influenced by the SAM. No station records with more than 50% missing data were used. An average of station data is used simply because this analysis was initially performed individually on all 7 stations in each grouping and similar results were found for each station, as shown in Table 3.1. Palmer Station (PSA) is actually the most unique, with a best lag occurring with SAM leading the departure CO_2 tendency by 7 months rather than the more typical 3 months.

Figure 3.9 (c) displays the lag correlation between the SAM and the departure CO_2 tendency for stations from 0-30°S (circles) and for stations south of 30°S (crosses). The best correlation for the stations south of 30°S occurs with the SAM leading the departure CO_2 tendency by 3 months. Only the correlations for stations below 30°S are significant at the 95% level, suggesting that stations south of 30°S have a stronger association with the SAM than those further north, as predicted. The lag correlation implies that 3 months after a high-index SAM event, there is an uptake of CO_2 relative to the global mean at all stations south of 30°S. While this result agrees with the hypothesis that a high-index SAM is associated with anomalous easterly winds and reduced upwelling, producing CO_2 uptake [*Hall and Visbeck*, 2002; *Lovenduski and Gruber*, 2005] for stations between 50°S and 30°S, it does not explain the uptake of CO_2 relative to the global mean also observed for stations south of 50°S. Also note that compared to Figure 3.8, this relationship is of the opposite sign. It is possible that the uptake observed south of 50°S is caused by the transport of anomalously low CO_2 from the region between 50°S and 30°S, but the similar time lags over all latitudes suggest that this is not the case. Another possible explanation for the discrepancy is that we lack understanding

as to what exactly the departure tendency represents physically; perhaps as hypothesized there is outgassing of CO_2 south of 50°S following a high-index SAM event, but uptake of CO_2 *relative to the global mean.*

Besides the difficulty in understanding the physical meaning of departure data, NH departure tendencies had little relationship to the NAM (not shown here), which suggests that this technique also removes some of the NAM or SAM signal inherent in the global mean. With these problems in mind, we remain cautious about these findings.

3.4 Discussion

This chapter examined the relationships between three major patterns of large-scale atmospheric variability and the monthly mean CO_2 concentration, tendency, and departure anomalies. Several results are reviewed in this section.

First, the relationships between the three climate patterns and the CO_2 concentrations lacked causality, so we decided that because a change in the circulation pattern would drive a change in the time rate of change of CO_2 rather than CO_2 itself, we would use the CO_2 tendency instead. Secondly, we found that an El Niño event leads positive CO_2 tendencies at Mauna Loa by 5 months, in agreement with the theory that forest fires caused by less precipitation and higher temperatures following a warm ENSO event will lead to a biospheric source of CO_2 to the atmosphere. We also found that a high-index NAM leads a negative CO_2 tendency at Barrow, Alaska by 6 months. This is also in agreement with the theory that a high-index NAM will lead to fewer cold outbreaks over boreal NH high latitudes, resulting in earlier growth seasons and thus an anomalous biospheric uptake of CO_2 from the atmosphere.

Less robust results were found for the relationship between the SAM and the CO_2 tendency at Palmer Station, Antarctica. Simple correlations between the SAM and the CO_2 tendency failed to highlight a causal relationship. Removing the ENSO signal via linear fit improved the significance of the correlations. However, volcanic signals (in particular, the Mt. Pinatubo eruption) interrupt a significant portion of the available time record, possibly making the relationship between the SAM and CO_2 flux difficult to perceive.

In order to account for this large "global mean" signal that includes volcanic and ENSO events, we created a new "departure" CO_2 tendency time series that subtracts the global mean CO_2 tendency from the original CO_2 tendency station data. The departure time series can be viewed as variations in local CO_2 relative to the global mean CO_2. With the global mean removed, we found that a high-index SAM leads a negative departure CO_2 tendency (or an atmospheric CO_2 uptake greater than the global mean) by 3 months. While this result agrees with the hypothesis that a high-index SAM produces CO_2 uptake due to reduced outgassing for stations between 50°S and 30°S, it does not explain the uptake of CO_2 relative to the global mean also observed for stations south of 50°S at similar lags, where a CO_2 source is predicted. Moreover, NH departure tendencies did not significantly correlate with the NAM, suggesting that the departure data may not be applicable to the problem of isolating the NAM/SAM signals.

In the next chapter, we continue exploring these relationships using CO_2 data resolved on daily time scales rather than data that has been averaged to form a monthly mean. This is done in order to more closely examine whether day-to-day variations in

large-scale circulation patterns may affect CO_2 measurements at the surface, as well as to exploit the high temporal resolution of the CO_2 data.

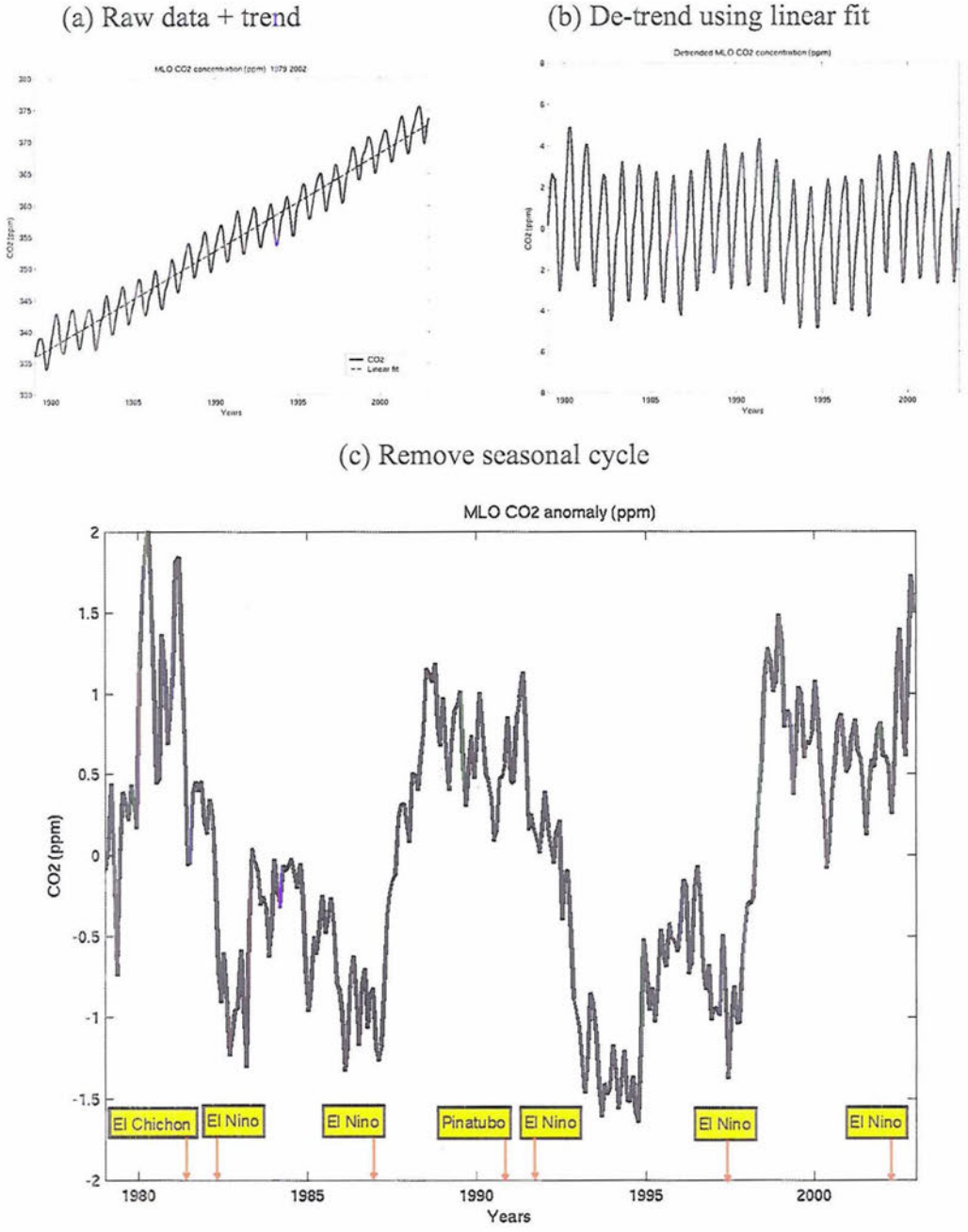

Figure 3.1 Monthly mean CO_2 concentrations from Mauna Loa (MLO). (a) Raw monthly data (solid) from 1979-2002 with global linear trend (dashed), (b) the de-trended data, and (c) the anomalies (seasonal cycle removed) in parts per million. Major El Niño events and volcanic eruptions are marked on the timeline.

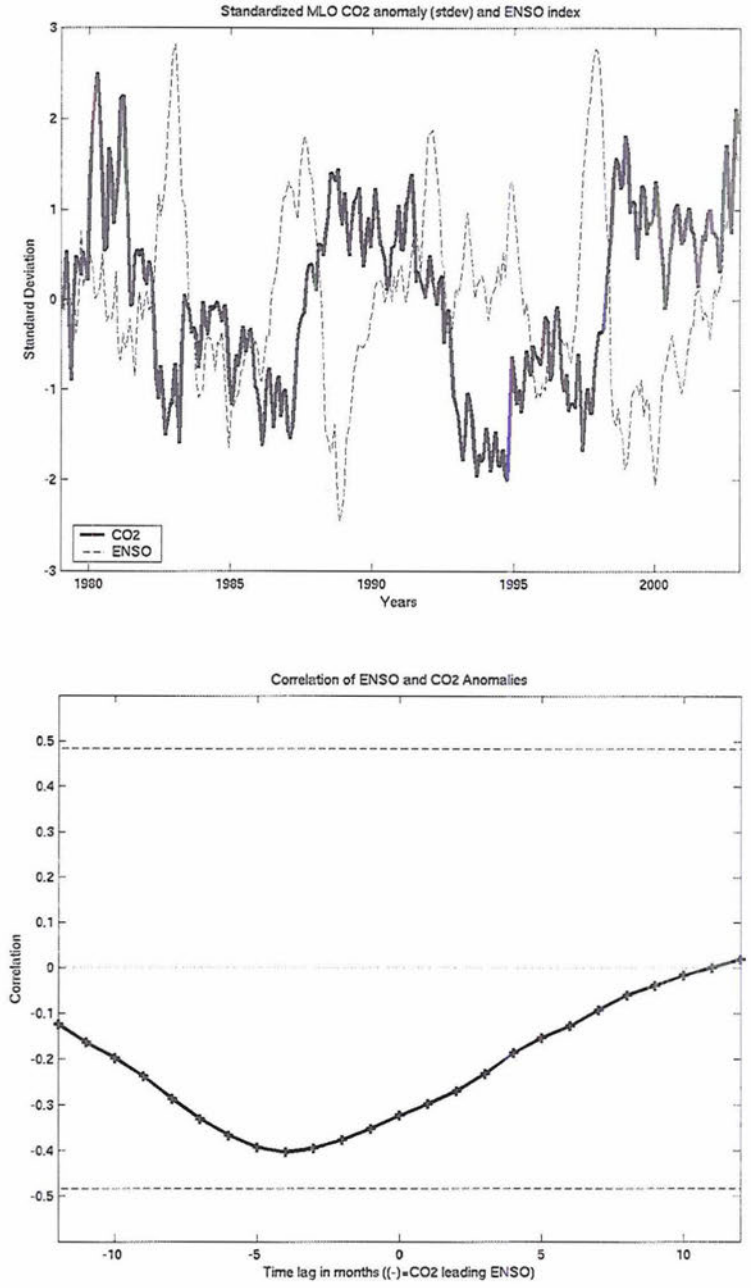

Figure 3.2 (top) Standardized time series of monthly mean CO_2 anomalies at MLO (solid) and the ENSO index (dashed) and (bottom) The lag correlation between the two time series. Negative lags imply CO_2 leading ENSO. The 95% significant level is marked (dashed lines).

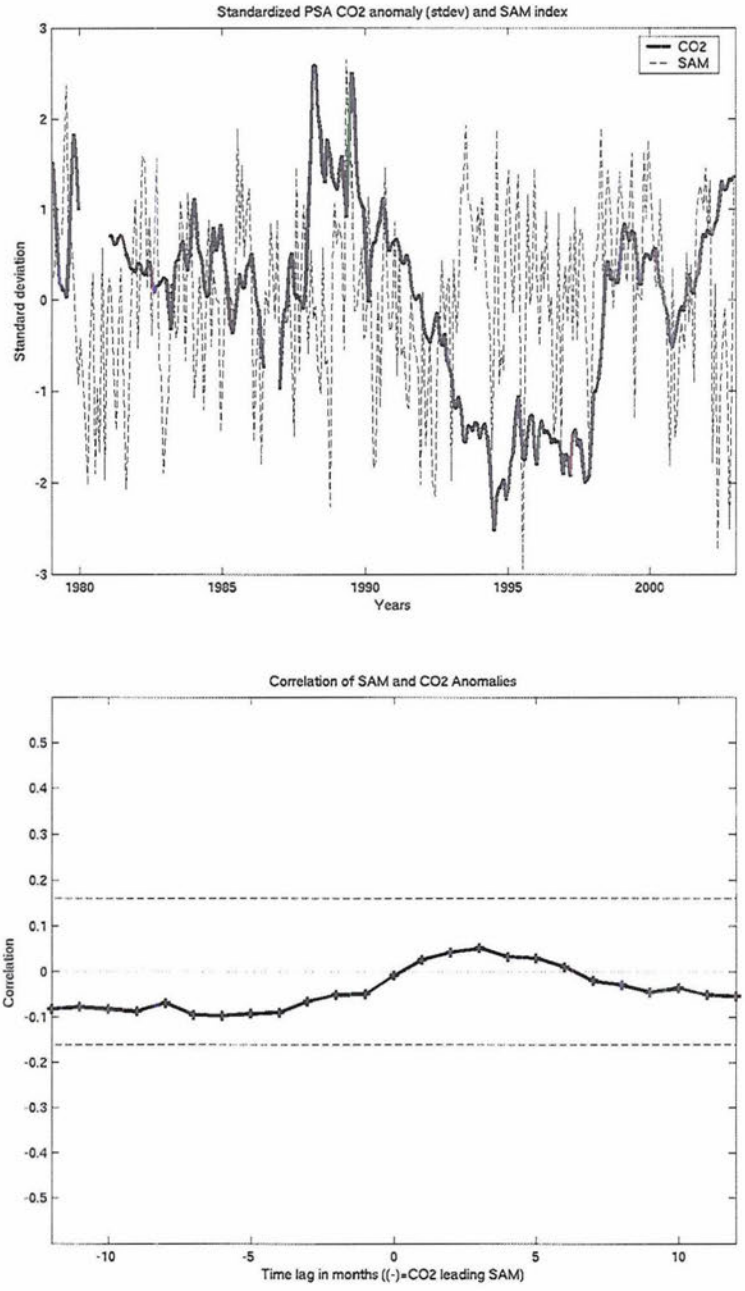

Figure 3.3 (top) Time series of monthly mean CO_2 anomalies (solid) for Palmer Station (PSA) and the SAM index (dashed) and (bottom) The lag correlation between the two time series. Negative lags imply CO_2 leading ENSO. No correlations are significant at the 95% level (dashed lines).

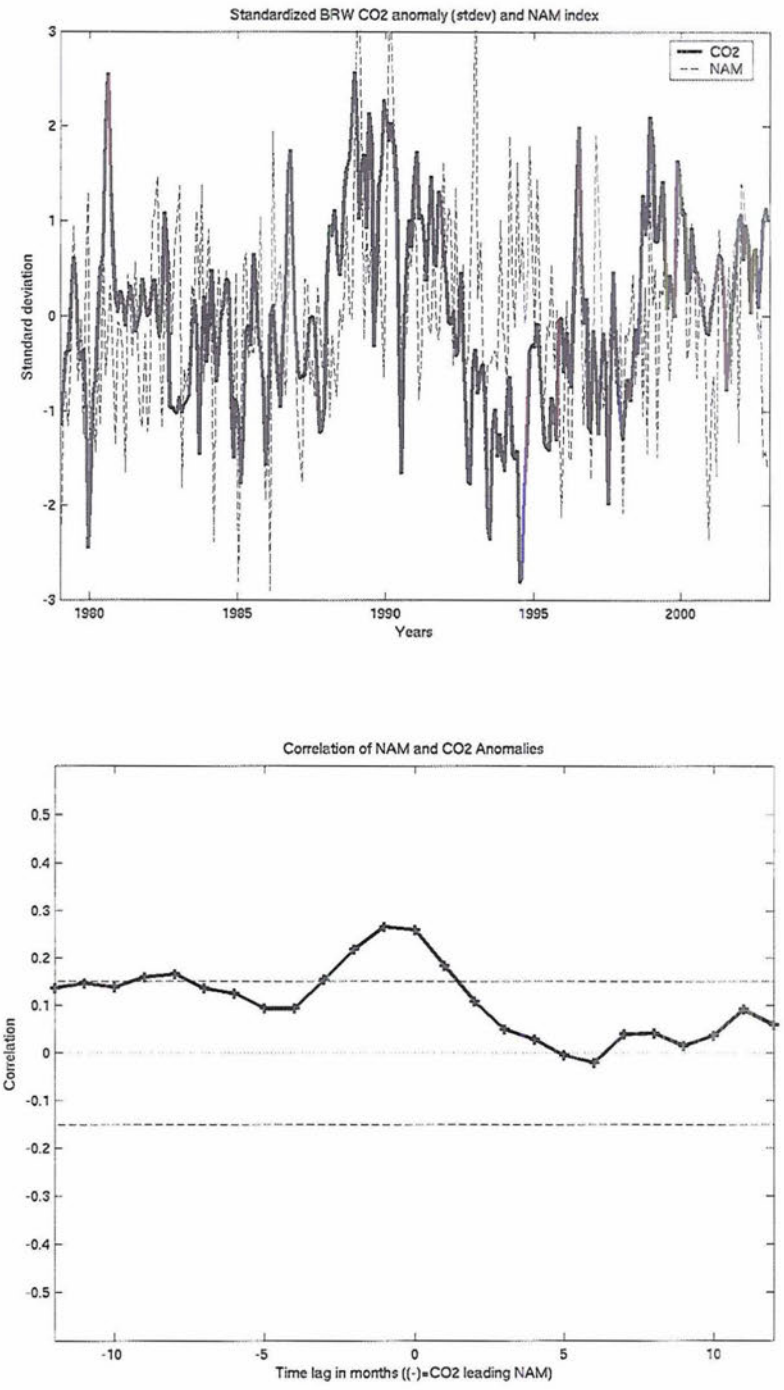

Figure 3.4 (top) Time series of monthly mean CO_2 anomalies (solid) for Barrow, Alaska (BRW) and the NAM index (dashed). (bottom) The lag correlation between the two time series. Negative lags imply CO_2 leading ENSO. The 95% significance level is marked (dashed lines).

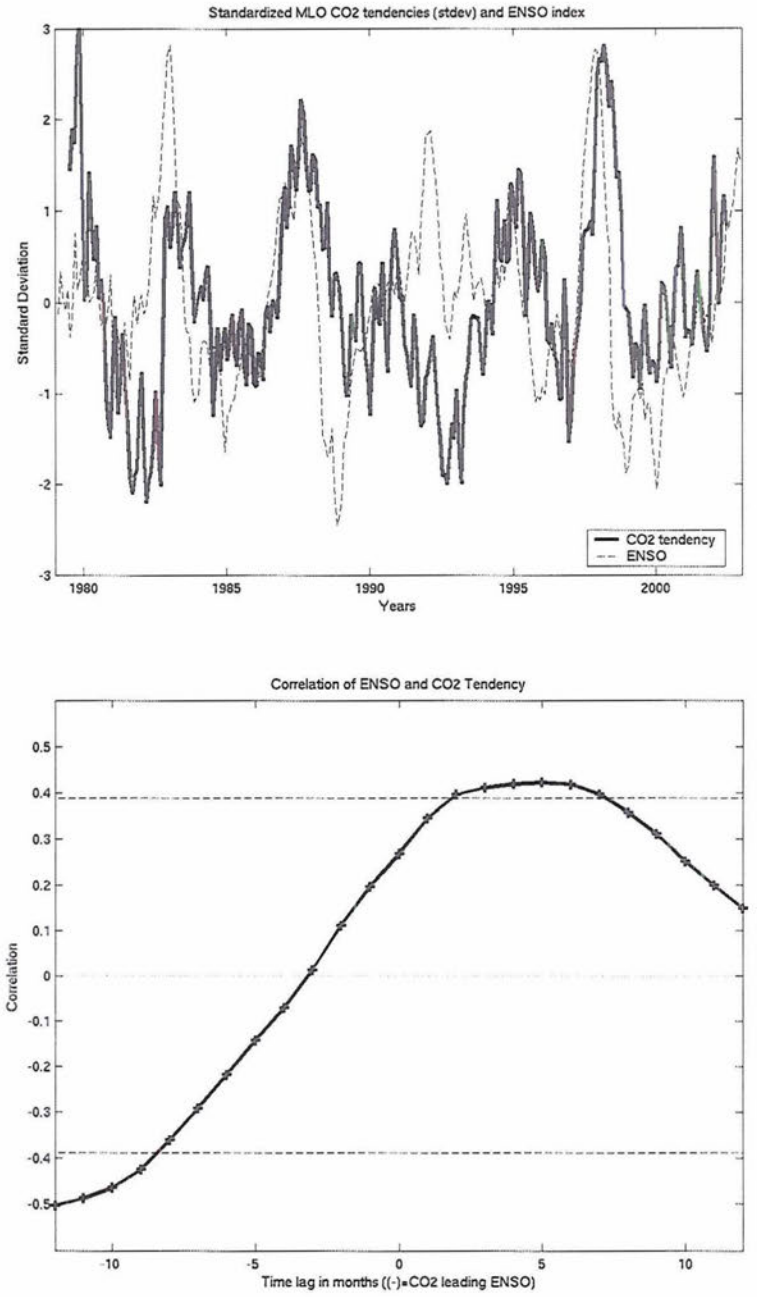

Figure 3.5 (top) Time series of monthly mean CO_2 tendencies for MLO (solid) and ENSO (dashed). (bottom) The lag correlations between the two time series. Negative lags imply CO_2 leading ENSO. These correlations are 95% significant (dashed lines).

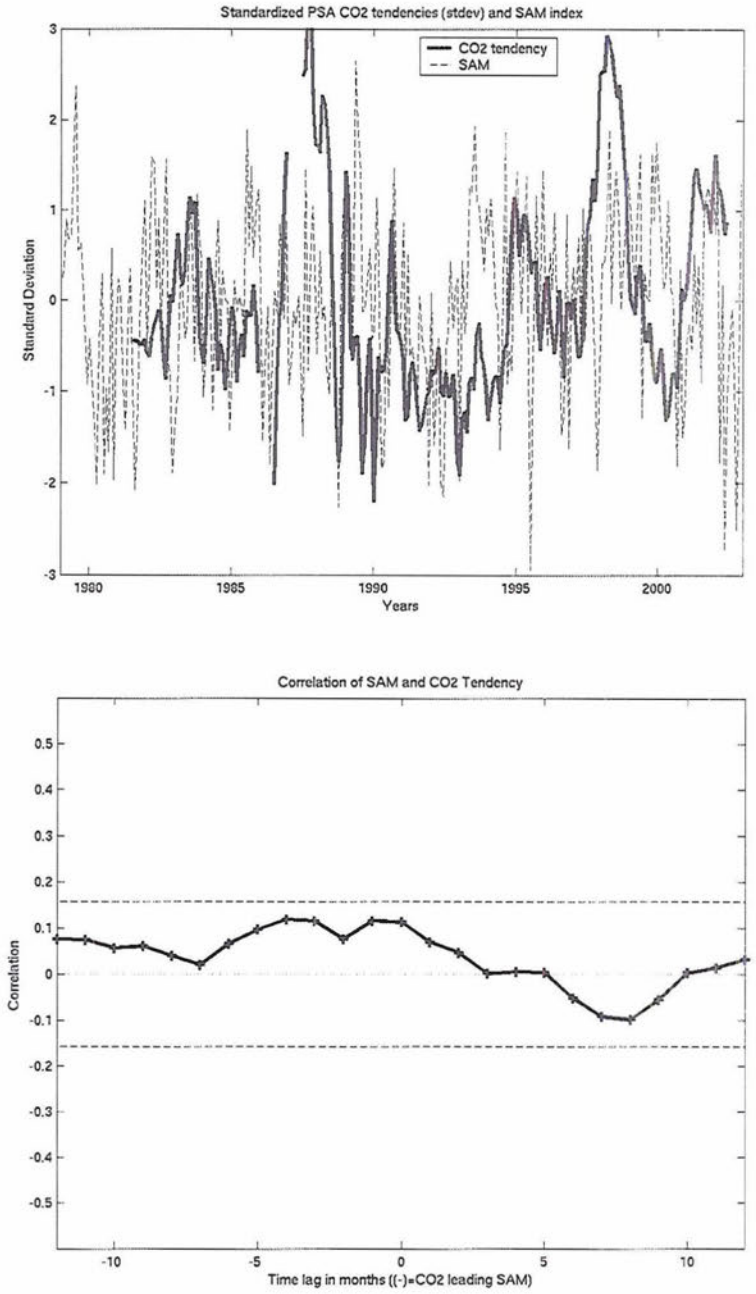

Figure 3.6 (top) Time series of PSA monthly mean CO_2 tendencies (solid) and SAM (dashed). (bottom) The lag correlations between the two time series. Negative lags imply CO_2 leading SAM. 95% significant lines are marked (dashed lines).

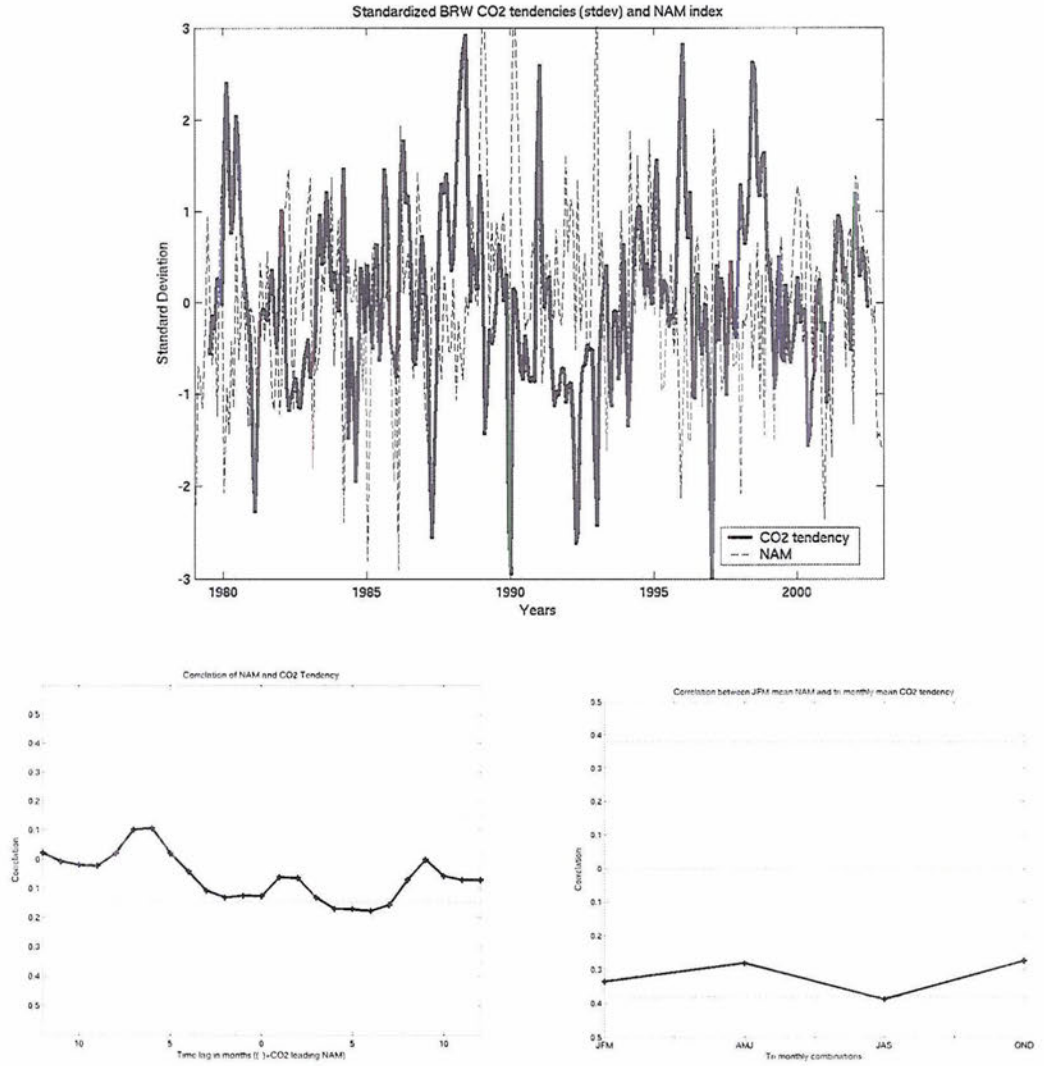

Figure 3.7 (top) Time series of BRW monthly mean CO_2 tendencies (solid) and NAM (dashed). (bottom left) The lag correlations between the two time series. Negative lags imply CO_2 leading the NAM. These correlations are 95% significant (dashed lines). (bottom right) The correlations between the JFM-mean NAM and the tri-monthly mean CO_2 tendency. 95% significant levels are marked (dashed lines), and are based on the JAS CO_2 tendency autocorrelation.

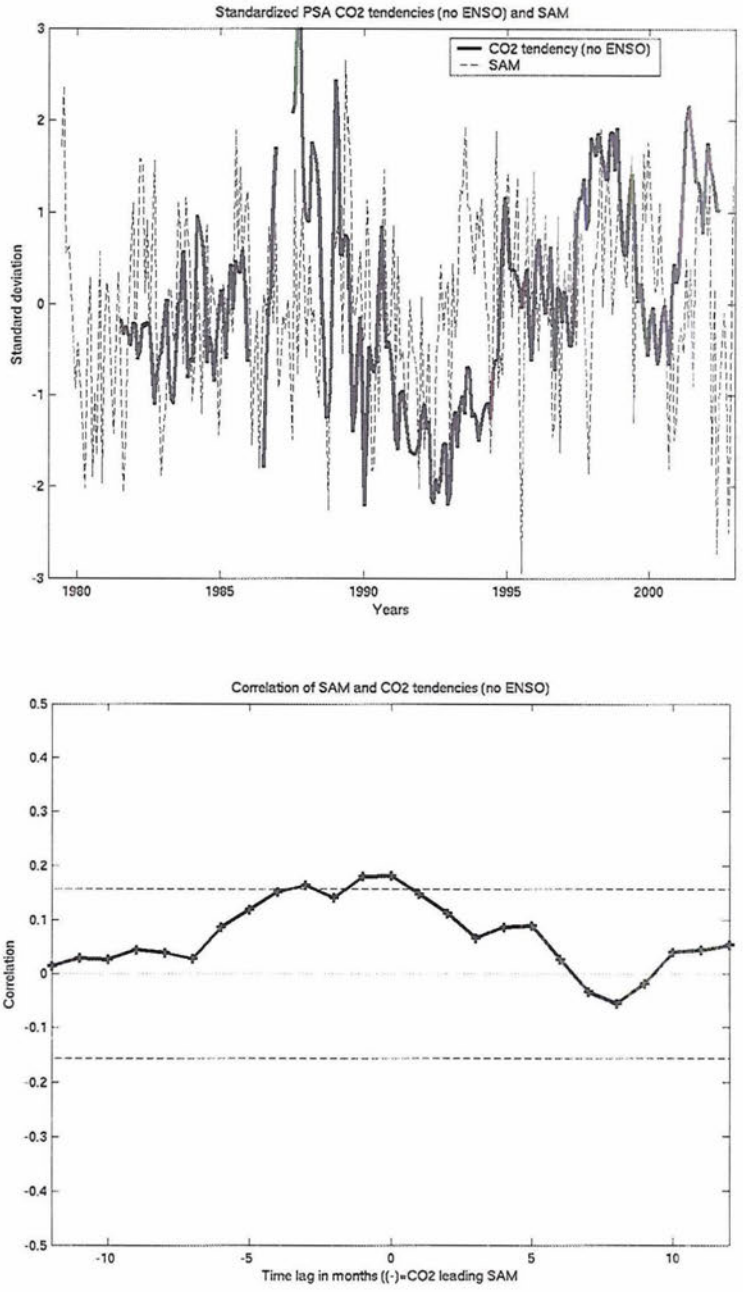

Figure 3.8 (top) Time series of PSA monthly mean CO_2 tendencies (solid) and SAM index (dashed) with ENSO removed from the tendencies using a linear least-squares fit at the best lag between PSA and ENSO. (bottom) The lag correlations between the two time series. Negative lags imply CO_2 leading SAM. These correlations are 95% significant (dashed lines).

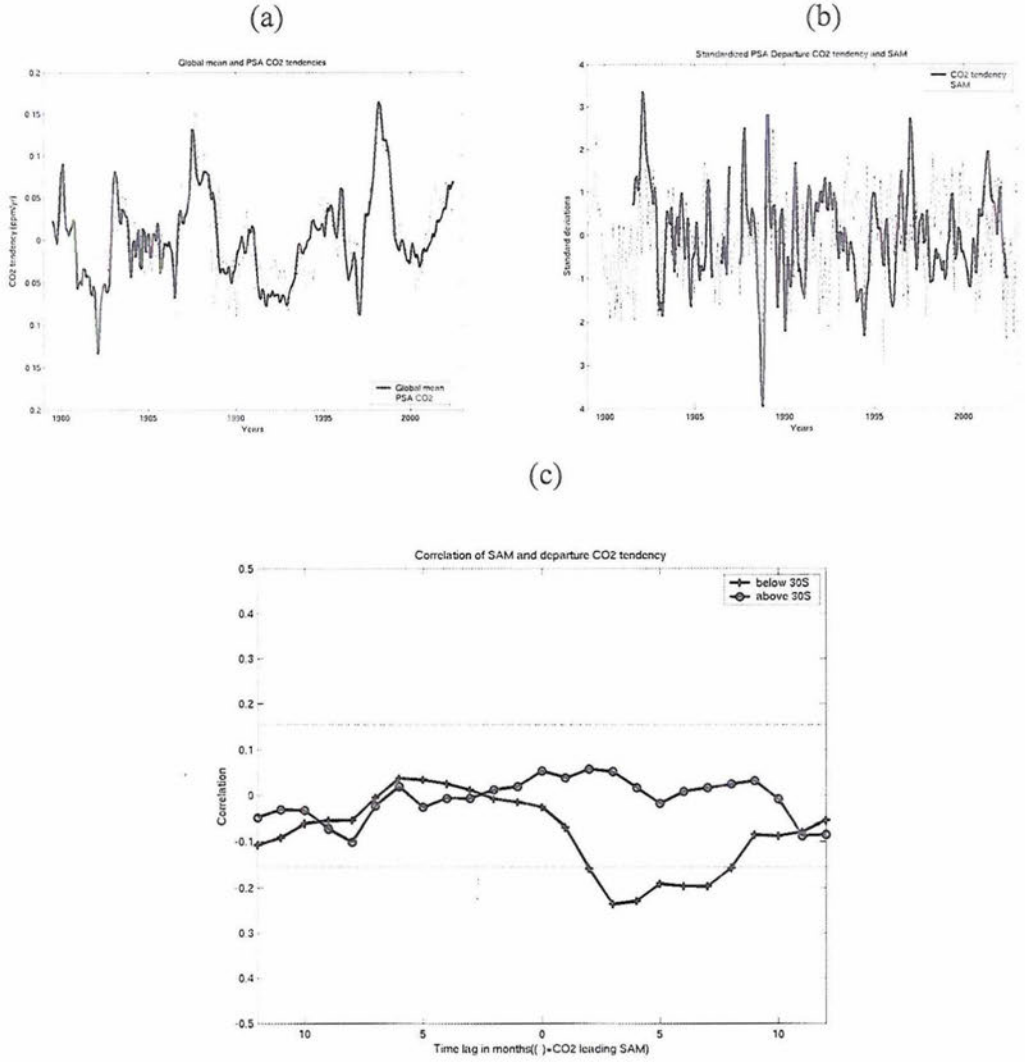

Figure 3.9 (a) Time series of the global mean tendencies (solid) and PSA CO_2 tendency (dashed). (b) Time series of PSA departure tendencies (solid) and SAM (dashed). (c) The lag correlations between SAM and the departure tendencies south of 30°S (crosses) and from 0-30°S (circles). 95% significant lines are marked.

Table 3.1 Best lags (SAM leading departure CO_2 tendency) for all stations south of 30°S with less than 50% NaNs. All correlations are significant at the 95% level for the 2-tailed t-statistic.

Station of CO_2 departure tendency	Best Lag when correlated to SAM index (with SAM leading the departure tendency)	Correlation at best lag
Cape Grim, Australia (CGO)	**3 months**	**-0.23**
Halley Bay, Antarctica (HBA)	**3 months**	**-0.26**
POCS30 (ship track)	**3 months**	**-0.20**
POCS35 (ship track)	**2 months**	**-0.27**
Palmer Station, Antarctica (PSA)	**7 months**	**-0.25**
South Pole, Antarctica (SPO)	**3 months**	**-0.18**
Syowa Station, Antarctica (SYO)	**1 month**	**-0.21**

CHAPTER 4: DAILY OBSERVATIONAL CO_2 CONCENTRATIONS AND RELATIONSHIPS TO THE NAM AND SAM

The main purpose of this chapter is to utilize the highest available temporal resolution of the observational NOAA CMDL CO_2 station data. While the "daily CO_2" generally only has weekly sampling frequency (Chapter 2), we denote this data as "daily" because there are generally several measurements per day, which we averaged together to form mean "daily" values. Using this data allows us to obtain a greater sample size and thus gain more degrees of freedom than we have in the monthly record. Variations in CO_2 on these shorter time scales potentially reflect advection along latitude bands in addition to fluxes from the ocean or biosphere.

We compare the daily CO_2 at Barrow, Alaska (BRW) and Palmer Station, Antarctica (PSA) to the NAM and the SAM indices, respectively, and also use composite and regression analysis to look for robust patterns in the 500-hPa height field (seasonal cycle removed) that occur for high or low CO_2 days. Other stations were also examined, but we focus on these two stations because of their lengthier time records and locations near the NAM/SAM centers of action. We also only look at concentrations in this chapter, rather than tendencies as in Chapter 3, because the tendencies of the daily CO_2 concentrations have a low signal-to-noise ratio.

4.1 Daily CO_2 concentrations and relationships to the NAM

4.1.1 Analysis using global mean linear trend

In this section we examine the relationship of the daily CO_2 concentrations at BRW to the NAM. Figure 4.1 (top) shows the daily CO_2 concentrations for BRW and the global mean linear trend. We create daily CO_2 anomalies by subtracting the global mean linear trend and then removing the seasonal cycle, using the method described in Chapter 2. These CO_2 anomalies (standardized) are shown in Figure 4.1 (middle) along with the standardized daily NAM index (solid red line). From this figure we can see some degree of agreement between the two time series, particularly during two strong high-index NAM events that occurred ~1989-1990, before the Pinatubo eruption in 1991. Following the eruption, the time series appear much less correlated up to 4 years later. There are also other periods in the time series where the time series lack agreement, suggesting that the NAM may play some role in the changes in CO_2 at BRW but is certainly not the only driving factor.

Figure 4.1 (bottom) illustrates the lag correlation (+/- 60 days) between the daily BRW CO_2 anomalies and the daily NAM index. Significant positive correlations occur for almost all lags, even the negative lags in which the CO_2 anomalies lead the NAM index. The highest positive correlations occur 7-10 days after a NAM event, suggesting that anomalously high CO_2 is found at BRW about a week after a high-index NAM event. This result generally agrees with the correlations between the monthly mean CO_2 concentrations and the NAM (Figure 3.4 (bottom)), as expected, but since the time scales are shorter we get a more accurate idea of the timing of the peak correlation. While it's feasible that biospheric or oceanic fluxes could vary on the order of a week (or even a

few days), it seems less likely that the NAM could drive surface climate changes that would then affect these fluxes within that time frame. Therefore, it is possible that, on short time scales, circulation changes induced by the NAM drive advection of CO_2-enriched air into BRW following a high-index NAM event (and vice versa for a low-index event). However, the fact that the correlations are significant at almost all lags suggests that the relationship between the daily BRW CO_2 and the NAM is likely dominated by timescales greater than ~60 days, which indicates that these results do not necessarily reflect only advection and fluxes may still play a role.

In order to look at the circulation patterns associated with high or low CO_2 days at BRW, we can look at the composite difference of the 500-hPa height field for days at BRW with greater than 1 standard deviation of CO_2 minus days at BRW with less than -1 standard deviation of CO_2, shown in Figure 4.2 (top). As a side note, we focus on the 500-hPa height field throughout this chapter, because the annular modes are present year-round in the troposphere. Using the sea level pressure field instead yields similar results. We also look at lag zero throughout this analysis because, as shown in Figure 4.1 (bottom), the correlations have nearly the same level of significance at both lag zero and at lag 7 days. The patterns in Figure 4.2 (top) suggest that for days with higher-than-normal CO_2 at BRW, the height field at 500-hPa is characterized by lower-than-normal heights over the polar cap and higher-than-normal heights at mid-latitudes. This same pattern can also be seen in the regression of the 500-hPa height field onto the standardized time series of the daily BRW CO_2 in Figure 4.2 (bottom left). The lower heights over the polar cap and the higher heights over mid-latitudes are all 95% significant (Figure 4.2, bottom right). This pattern compares reasonably well to the

regression of the 500-hPa heights onto the daily NAM index (Figure 4.3). The main difference is the stronger amplitudes over the Atlantic sector of the mid-latitudes in Figure 4.3. This difference is perhaps expected, however, because while the NAM is associated with hemispheric circulation changes, advective changes in CO_2 should primarily be associated with changes in circulation near Barrow.

These results suggest that high CO_2 days at BRW are associated with circulation patterns resembling the high-index NAM. Barrow is located on the gradient between the high and low heights (marked with a red 'x' in Figure 4.2 (top)), suggesting that high CO_2 occurs when the circumpolar flow is cyclonic. Since we are looking at the zero lag relationships, we hypothesize that this NAM-like pattern is indicative of advection of high CO_2 air into BRW, but it is difficult to interpret where this anomalously CO_2-enriched air would be coming from. While the circulation trajectory suggests that it may come from boreal Asia, understanding why air parcels anomalously high in CO_2 would be originating from there is beyond the scope of this thesis.

4.1.2 Further Analysis

Figure 4.4 shows the months (top) and years (bottom) of the days used in the composite analysis in Figure 4.2 (top), for days with greater than +1 standard deviation (left) and days with less than -1 standard deviation (right) of CO_2 at BRW. While high CO_2 days at BRW are dispersed relatively evenly over every calendar month (with a high peak in July), low CO_2 days are more biased towards fall and winter months. High CO_2 days also occur mostly during the period 1989-1992, while low CO_2 days occur mostly during the periods 1984-1987 and 1993-1998. Hence, our previous analysis is really only drawn from ~3 periods (note that significance levels calculated throughout this chapter

are based on N_{eff}, defined in Chapter 2). Evidently, these long periods of high or low CO_2 result from the inherent low-frequency variability in the CO_2 time series (these periods can also be seen in Figure 4.1 (middle), above and below the dashed 1 standard deviation lines). These time periods do not directly correspond to ENSO (although the 1993-1998 period of low CO_2 may result from the Pinatubo eruption) and thus they may be driven by the low-frequency variability in the NAM index itself.

In order to obtain samples from a larger portion of the record, we use a 5^{th}-degree polynomial fit to the daily CO_2 trend instead of the global mean linear trend, shown in Figure 4.5 (top left). Clearly, removal of this curvier fit will eliminate some of the low-frequency variability of the daily CO_2 time series. Performing the rest of the analysis in the same manner, we find the regression of the 500-hPa height field onto the newly-de-trended daily BRW CO_2 in Figure 4.5 (top right). The pattern is very similar to that found using the global linear trend removal (Figure 4.2, bottom left). Figure 4.5 (bottom left and right) reveals a similar dispersion of high and low CO_2 days across calendar months as in the linear trend case (Figure 4.4, top), but with slightly better sampling across years. In conclusion, the fairly small differences in the results suggest that for the NH daily CO_2, the results are robust to the method of trend removal. We will show in the following section that this is not the case in the SH.

Because the strongest NAM events generally occur in the NH winter, and because the location of the CMDL stations may influence how changes in air circulation or local fluxes impact the CO_2 measured at that station, the final step in this analysis is to look for seasonality or location effects on the results. Because the method of trend removal did not affect the results, we remove the global mean linear trend from the daily CO_2 for the

remainder of this section. Figure 4.6 (top) shows the regression of the JFM 500-hPa height field onto the standardized JFM daily CO_2 at BRW. This pattern has stronger amplitude and is more zonally symmetric than the pattern based on year-round heights and CO_2 (Figure 4.2, bottom left); in other words, it is slightly more NAM-like. The progression through the rest of the seasons (AMJ, JAS, OND) corresponds to a weakening of the amplitude and a distortion of the symmetrical pattern in the height field. This result suggests that the circulation of the NAM is most strongly associated with instantaneous CO_2 changes at BRW in the NH winter months.

Figure 4.6 (bottom) shows the regression of the 500-hPa height field onto the standardized daily CO_2 at Cold Bay, Alaska (CBA, marked with a red 'x' on the figure). This pattern is considerably less NAM-like than the corresponding pattern at BRW, and also is slightly shifted so that CBA is located at the gradient between high and low heights similar to the location of BRW in Figure 4.2 (top). Therefore, like at BRW, high CO_2 days at CBA are associated with westerly zonal flow at the 500-hPa level above CBA. Several other NH stations are also located at the gradient between high and low heights; in certain cases, this pattern exists although the overall pattern is not NAM-like. This result may indicate that the daily variations in CO_2 at these stations on short time scales is due to local changes in advection, and at BRW the changes in circulation happen to resemble the NAM.

4.2 Daily CO_2 concentrations and relationships to the SAM

4.2.1 Analysis using global mean linear trend

For the SH analysis, we focus on Palmer Station (PSA) rather than the longer record at the South Pole (SPO) because if atmospheric CO_2 in the SH is affected by

changes in air-sea flux or changes in advection driven by the SAM, then we are more likely to detect those local changes at Palmer Station (located on the Antarctic Peninsula) than at the South Pole.

Figure 4.7 (top) shows the time series of daily CO_2 at PSA and the global mean linear trend. There are some periods early in the record where data are missing. It is apparent that this SH station has substantially less seasonal variability in CO_2 than a NH station such as BRW (Figure 4.1, top). Removal of the global mean linear trend and the small seasonal cycle results in daily CO_2 anomalies, shown standardized (blue crosses) in Figure 4.7 (middle) along with the standardized SAM index (red line). The main feature in the anomaly time series is the decrease in CO_2 following the Pinatubo eruption. Due largely to this decrease, a relationship between the daily PSA CO_2 anomalies and the SAM index is not visually apparent.

Indeed, correlations between the daily CO_2 anomalies at PSA and the SAM index (Figure 4.7, bottom) show no significance at any lag. This result agrees with the lack of significant correlations between monthly mean CO_2 anomalies and the SAM discussed in Chapter 3. Other SH stations also lack significant correlations. Evidently, the SAM does not have a strong effect on local variations in CO_2 even on short timescales.

Repeating the analysis that we used for daily BRW CO_2, we composite the difference of 500-hPa heights for high CO_2 and low CO_2 days at PSA as shown in Figure 4.8 (top). Palmer Station is marked on this figure with a red 'x'. The resultant pattern is not symmetric about the pole and lacks resemblance to the pattern of the 500-hPa heights regressed onto the standardized daily SAM index (Figure 4.9). Similarly to the composite, the corresponding regression pattern and 95% significance contours for the

daily PSA CO_2 (Figure 4.8, bottom left and right) show higher-than-normal heights above Antarctica and lower-than-normal heights over the Pacific sector of the Southern Ocean, just off the coast of the Antarctic Peninsula where PSA is located. This means that PSA is located between the gradient of high and low heights (reminiscent of results in the NH) where winds flow poleward into the station. Therefore, even though the 500-hPa level circulation is *not* SAM-like for high or low CO_2 days at PSA, the circulation patterns that are present are suggestive of poleward advection into the station.

4.2.2 Analysis using 5th-degree polynomial fit removal

In Figure 4.7 (middle) we see that the daily PSA CO_2 anomalies are strongly influenced by the Pinatubo eruption. This fact is further illustrated in Figure 4.10, which shows the months (top) and years (bottom) of the days used in the composite analysis in Figure 4.8 (top), for days with greater than +1 standard deviation (left) and days with less than -1 standard deviation (right) of CO_2 at PSA. High and low CO_2 days at PSA are distributed relatively evenly across calendar months; however, most high CO_2 days only occur over the period 1989-1990 and most low CO_2 days only occur from 1994-1998. These periods are also evident in Figure 4.7 (middle), where the +/- 1 standard deviation line is marked with a dashed line. Evidently the composite analysis is based on samples drawn from only two periods, which does not provide a good sampling distribution.

It can be seen from Figure 4.7 (top) that the cause of this poor sampling may be due to our choice of linear trend removal. While using the global mean linear trend may be a decent approximation to the trend in fossil fuel emissions, removal of this linearity tends to emphasize low-frequency variability in the CO_2 concentrations such as the long-term effects of the Pinatubo eruption. In order to widen our sampling distribution, we

can use a 5th-degree polynomial fit to the CO_2 data instead of the global mean linear fit as a simple way to filter out low-frequencies.

The raw daily PSA CO_2 concentrations are plotted with the 5th-degree polynomial fit in Figure 4.11 (top left). Removal of this fit will eliminate some of the low-frequency variability associated with the Pinatubo eruption, retaining higher frequency variability that may be associated with more local effects such as changes in the circulation. After removing the 5th-degree fit, the analysis in section 4.2.1 is repeated. Figure 4.11 (top right) shows the lag correlations between the new daily PSA CO_2 anomalies and the daily SAM index. Significant positive correlations now occur for up to ~15 days after a SAM event, suggesting that a high-index SAM is associated with higher-than-normal CO_2 days at PSA up to 2 weeks later. This may be due to advection of CO_2-enriched air into the station and/or to the anomalous outgassing near the Antarctic coast associated with a high-index SAM, as hypothesized in *Lovenduski and Gruber* [2005].

Figure 4.11 (middle) illustrates the regression of the 500-hPa height field onto the new standardized daily PSA CO_2 anomalies. In comparison to the linear fit version in Figure 4.8 (bottom left), the pattern has a slightly stronger resemblance to the SAM, with weakly lower-than-normal heights above Antarctica and higher-than-normal heights at lower latitudes in most locations. In both figures, PSA is located between a very strong region of low heights and a fairly strong region of high heights, indicating poleward air flow into the station. If a composite is created from the new CO_2 anomalies for high and low CO_2 days at PSA, the distribution of extreme days over calendar month (Figure 4.11, bottom left) is very similar to the monthly distribution in the linear trend case. However, there is a better distribution of extreme days over years, as shown in Figure 4.11 (bottom

right). Instead of only one period each of high and low CO_2 days (as for the linear trend case), there are about 3 periods for both high and low CO_2 days. Although this distribution is an improvement, obviously we would gain more confidence in the regression pattern if we had more samples drawn from every year of the record.

In the case of the NH CO_2 anomalies, using a 5^{th}-degree fit rather than a linear fit did not significantly affect the results. Clearly, in the case of the SH, the result is much more "trend-dependent". This finding suggests that the relationship between the SH circulation pattern and CO_2 concentrations must be fairly weak because it varies based on the method of analysis. Nonetheless, using the 5^{th}-degree polynomial fit does broaden the sampling distribution, and we therefore continue to use this fit removal for the remainder of the SH analysis.

4.2.3 Further Analysis

Lastly, we examine the dependence of the results on seasonality and location. The seasonal influence on the results appears to be small. The regression pattern of the 500-hPa heights onto the daily PSA CO_2 anomalies (see Figure 4.11, top right) is weakest in the SH summer (JFM) but persists throughout the year (not shown). We also check to see how the pattern changes if we use different SH station CO_2 data. Figure 4.12 (top) shows the regression of the 500-hPa height field onto daily CO_2 anomalies at Halley Bay, Antarctica, while Figure 4.12 (bottom) shows the same regression onto daily CO_2 anomalies at Cape Grim, Australia. The patterns, while not as SAM-like as the regression at Palmer Station, are otherwise very similar to the pattern at PSA, with a "wave train" pattern of anomalously high and low heights across the South Pacific Ocean and the Antarctic Peninsula. Regression patterns at other stations, such as the South Pole

and Syowa Station, do not look similar; however, Syowa has a much shorter record while the South Pole CO_2 may not be influenced by the circulation changes in the same manner as stations at lower latitudes.

In the NH analysis the circulation pattern tended to move around depending on the location, so that the station was located between the gradient of high and low heights. This result suggested a linkage between the daily changes in CO_2 and the changes in local advection. In the SH, however, the pattern appears to remain stationary no matter where the changes in CO_2 are occurring, which implies that the variability may be originating from a pattern of variability that affects each location equally. From Figure 4.13, which shows the regression of the monthly mean 500-hPa heights onto the monthly ENSO index (inverted), we see that the pattern of heights associated with daily CO_2 at PSA, HBA, and CGO has a resemblance to the pattern of heights associated with ENSO. The sign of the regressions suggests that high CO_2 days at these stations are associated with concurrent La Niña events. Although removal of the 5^{th}-degree polynomial fit should have filtered out a substantial portion of the low-frequency contribution from ENSO, it evidently did not remove it completely.

4.3 Conclusions

In this chapter, we have analyzed how circulation patterns may be associated with changes in daily CO_2 anomalies. In particular, composite and regression patterns of the 500-hPa height field onto the NH daily CO_2 anomalies suggest that local changes in advection are likely driving changes in surface CO_2 anomalies on short time scales. However, the significance of the correlations between the NAM and daily BRW CO_2 for all lags (-40 days to +40 days) implies a dominance of variability by monthly timescales,

so that the results do not rule out the influence of the NAM on CO_2 flux from the ocean or biosphere. At BRW, the associated height field for high CO_2 days resembles the NAM, but this is not the case for all NH stations.

In the SH, the composite and regression patterns were dependent on the method of trend removal, suggesting that the relationship between the SH circulation and changes in daily SH CO_2 is weak. Using a 5^{th}-degree polynomial fit removal to broaden the sampling distribution of high and low CO_2 events, we found a high-index SAM-like pattern for high CO_2 days at PSA. Lag correlations verified a significant relationship of daily PSA CO_2 to the SAM up to 2 weeks after a SAM event. More apparent, however, was the wave-like pattern of anomalously high and low heights across the South Pacific Ocean and Antarctic Peninsula that occurred for regressions at CGO, HBA, and PSA. This pattern shared a likeness to the regression pattern of 500-hPa heights onto the ENSO index, suggesting that ENSO may still be dominating the CO_2 signal at SH stations despite the use of the 5^{th}-degree fit to filter out lower frequency signals like ENSO.

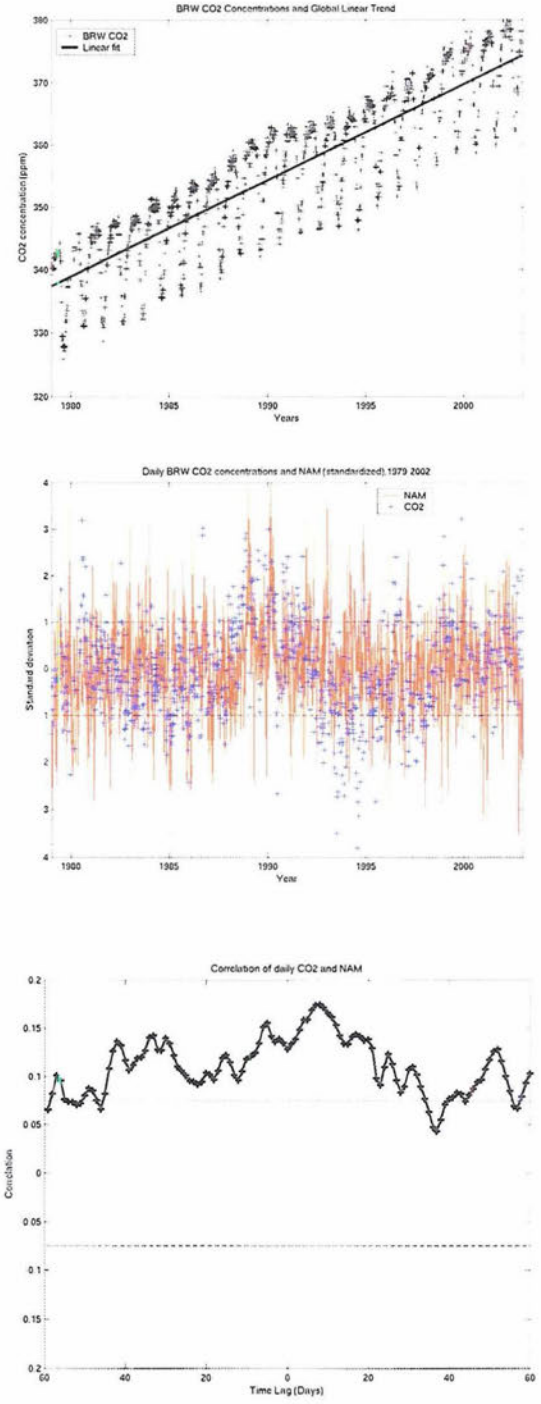

Figure 4.1 (top) Daily BRW CO_2 concentrations (crosses) and global linear trend (solid). (middle) Standardized daily BRW CO_2 concentration anomalies (blue crosses; de-trended, seasonal cycle removed) and standardized daily NAM index (red). (bottom) Lag correlation of daily CO_2 at BRW and the daily NAM index. Negative lags imply CO_2 leading the NAM. 95% significant lines are marked (dashed).

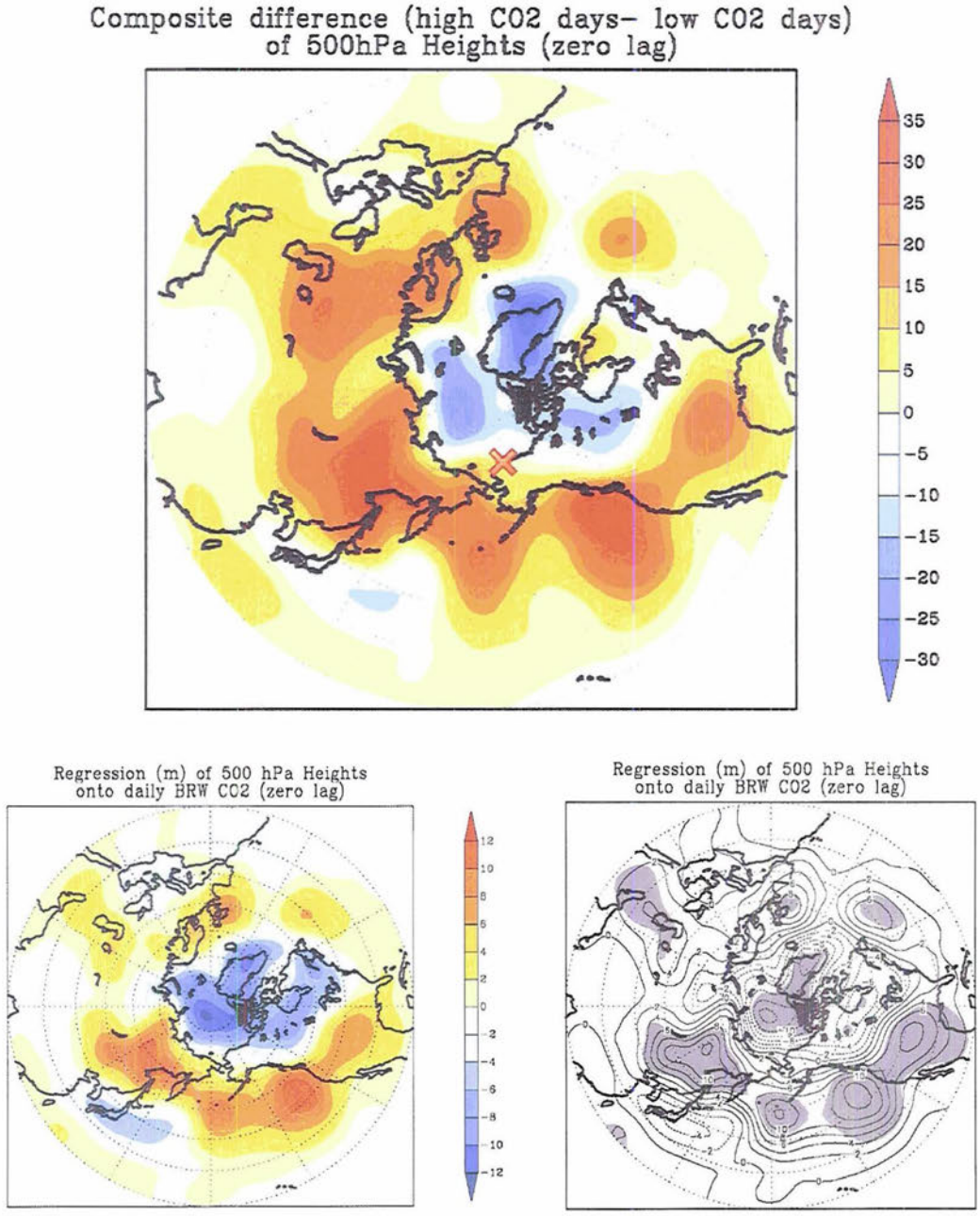

Figure 4.2 (top) Composite difference of 500-hPa height field for high CO_2 days and low CO_2 days at BRW at zero lag. Units are in meters. BRW is marked with a red 'x'. (bottom left) Regression of 500-hPa height field onto standardized daily BRW CO_2 concentration anomalies at zero lag. Units are in m/std CO_2. (bottom right) Same as in (bottom left), but with contours showing regression and shading showing regions that are 95% significant.

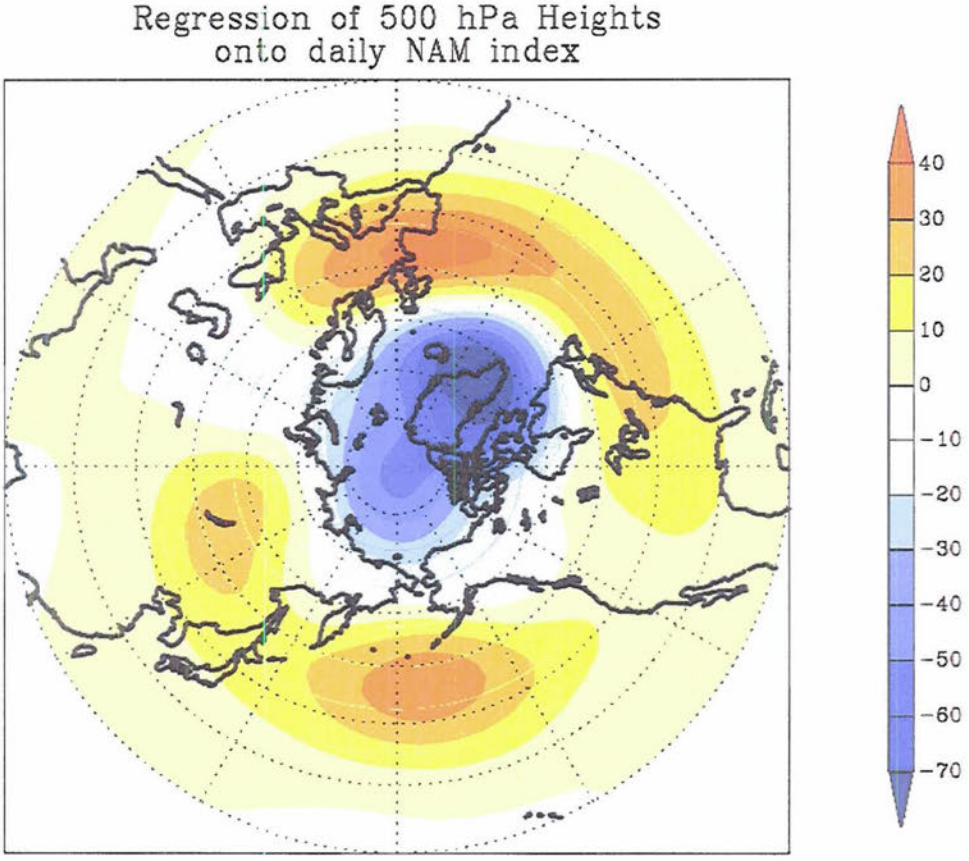

Figure 4.3 Regression of the 500-hPa height field onto the standardized daily NAM index. Units are meters/standard deviation of the NAM.

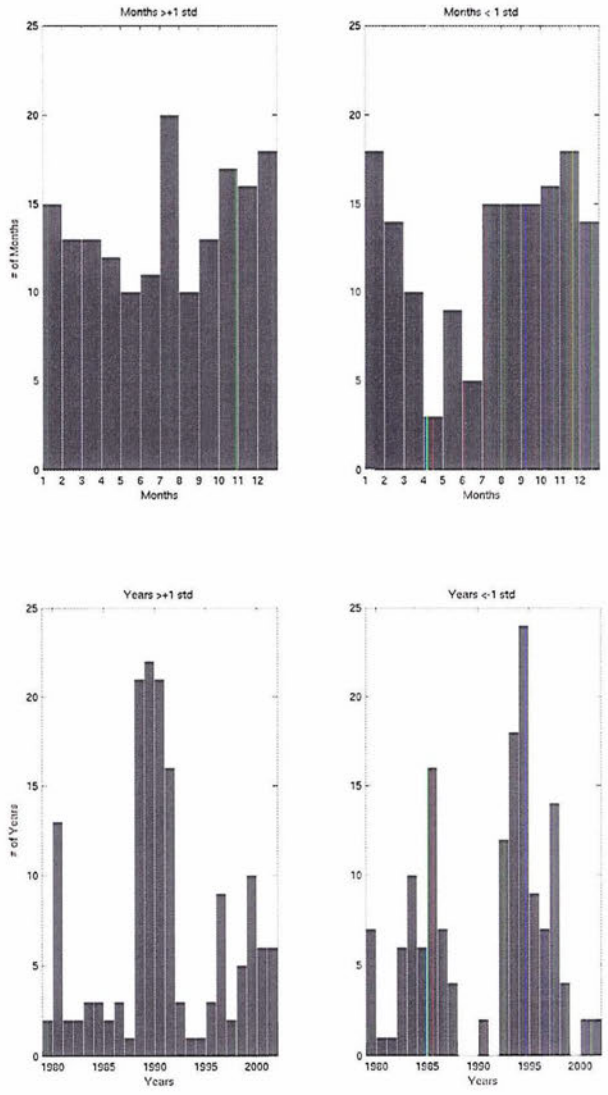

Figure 4.4 Histograms of (top) months used in composite analysis and (bottom) years used in composite analysis, for BRW CO_2 days >+1std (left) and <-1std (right).

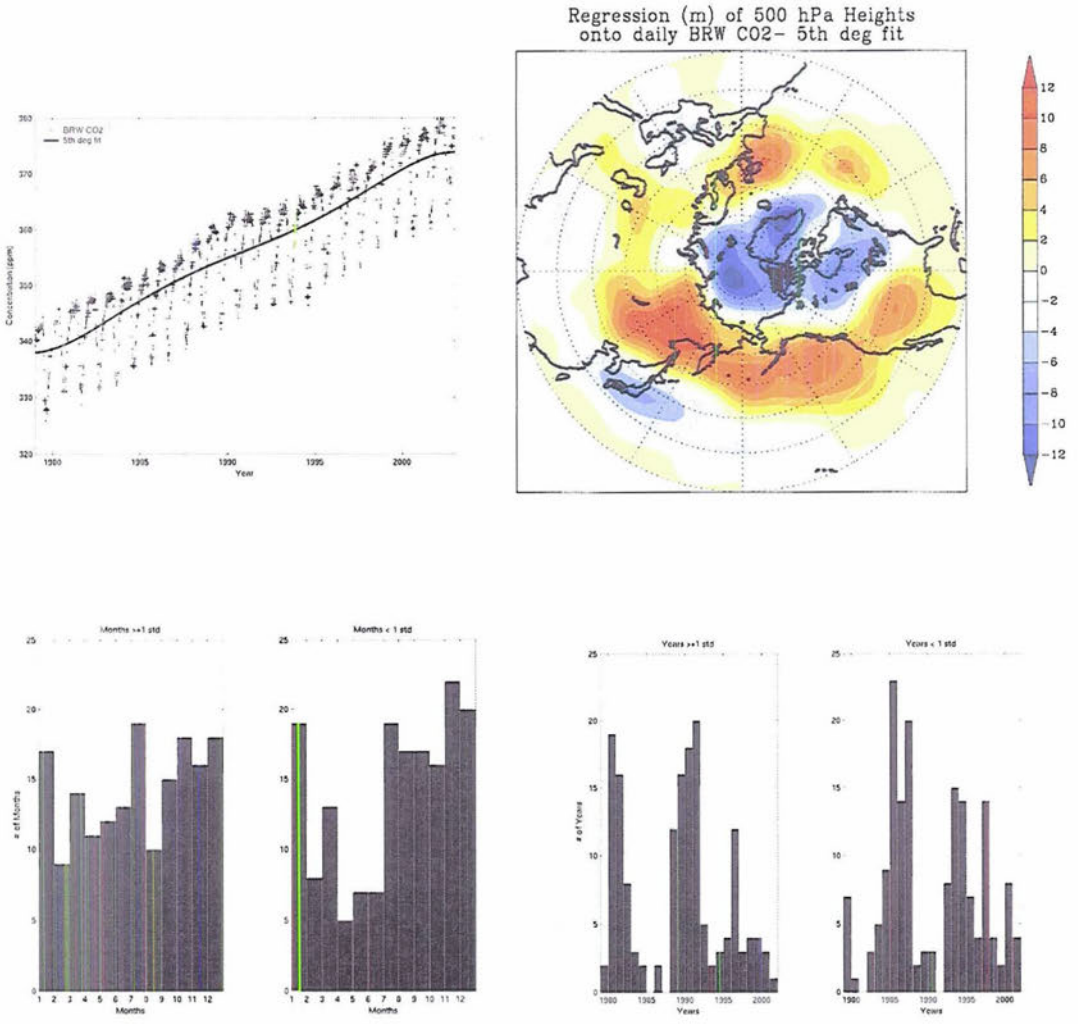

Figure 4.5 (top left) Same as in Figure 4.1 (top), but using a 5th-degree polynomial fit for the trend instead of the global linear trend. (top right) Regression (m/std) of 500-hPa height field onto daily BRW CO_2 anomalies that were de-trended using 5th-degree polynomial fit. (bottom left & right) Same as in Figure 4.4, but composite using 5th-degree polynomial fit removal.

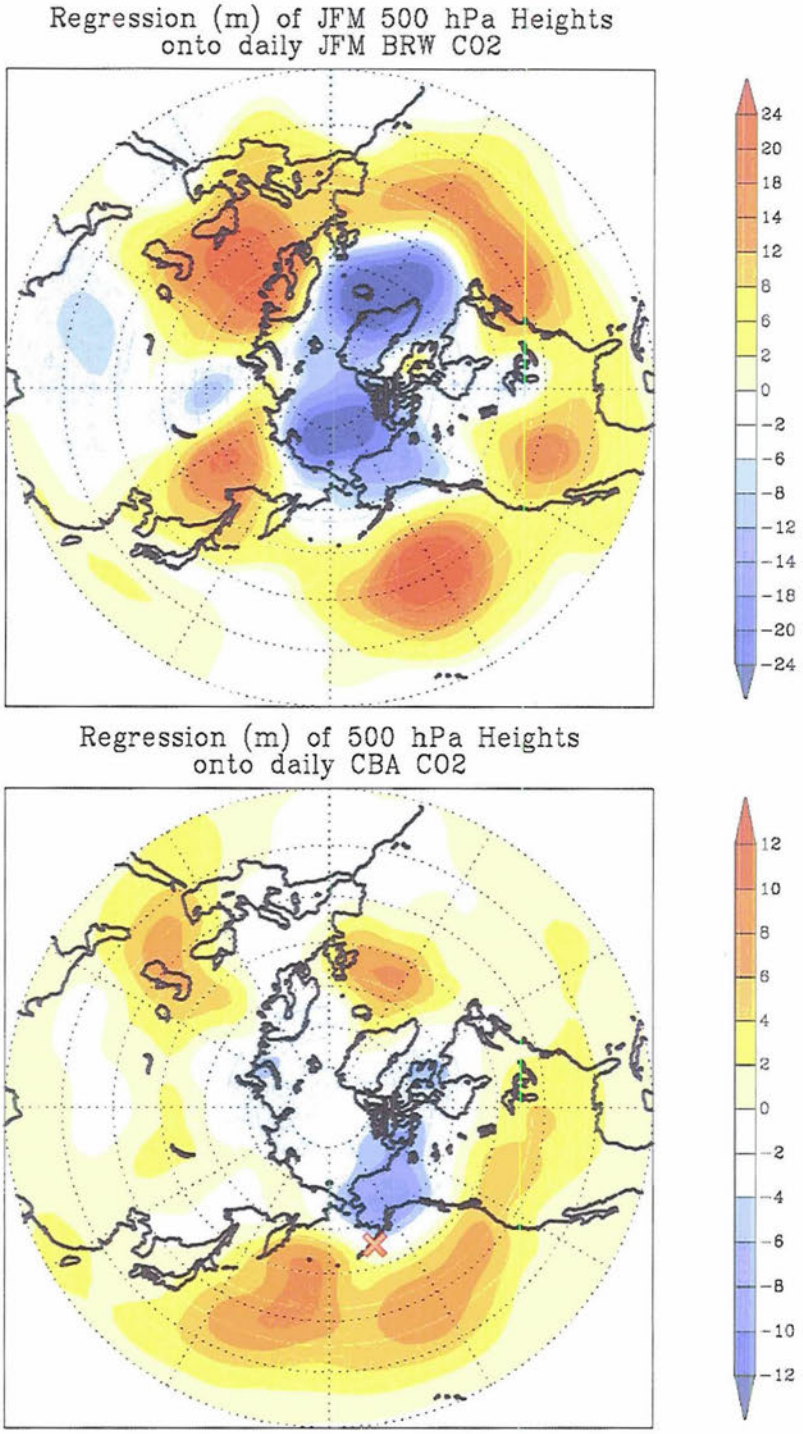

Figure 4.6 (top) Regression of the JFM 500-hPa height field onto the standardized JFM daily CO_2 at BRW (de-trended with global linear fit). (bottom) Regression of 500-hPa heights onto standardized daily CO_2 at Cold Bay, Alaska (CBA, marked with red 'x'). Units are in meters/ standard deviation of CO_2.

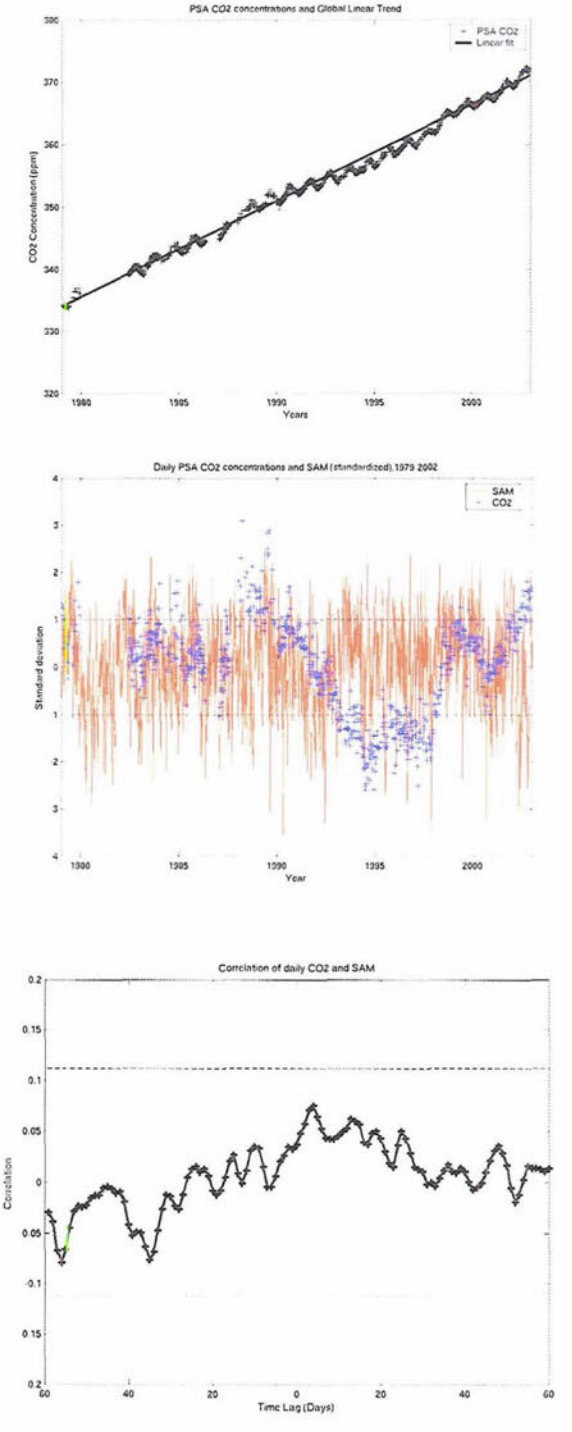

Figure 4.7 (top) Daily PSA CO_2 concentrations (crosses) and global linear trend (solid). (middle) Standardized daily PSA CO_2 concentration anomalies (blue crosses; de-trended, seasonal cycle removed) and standardized daily SAM index (red). (bottom) Lag correlation of daily CO_2 at PSA and the daily SAM index. Negative lags imply CO_2 leading the SAM. 95% significance levels are marked (dashed lines).

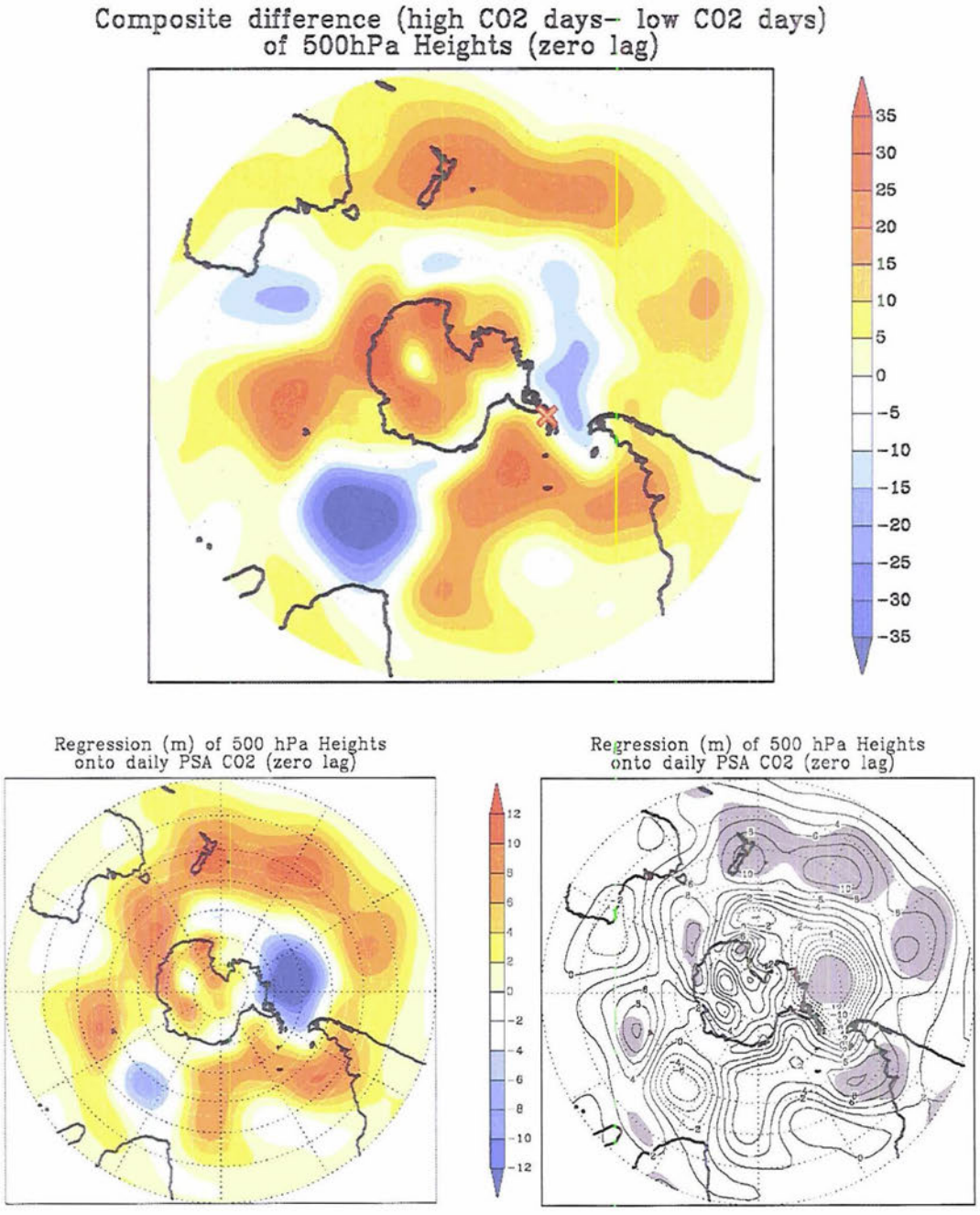

Figure 4.8 (top) Composite difference of 500-hPa height field for high CO_2 days and low CO_2 days at PSA at zero lag. Units are in meters. PSA is marked with a red 'x'. (bottom left) Regression of 500-hPa height field onto standardized daily PSA CO_2 concentration anomalies at zero lag. Units are in m/std CO_2. (bottom right) Same as in (bottom left), but with contours showing regression and shading showing regions that are 95% significant.

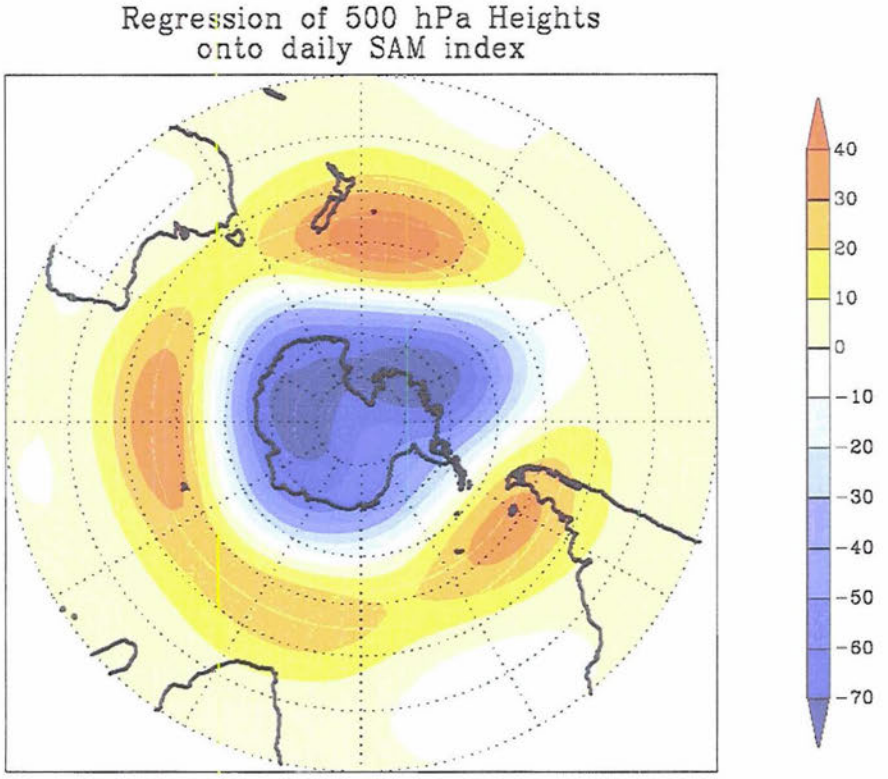

Figure 4.9 Regression of the 500-hPa height field onto the standardized daily SAM index. Units are meters/standard deviation of the SAM.

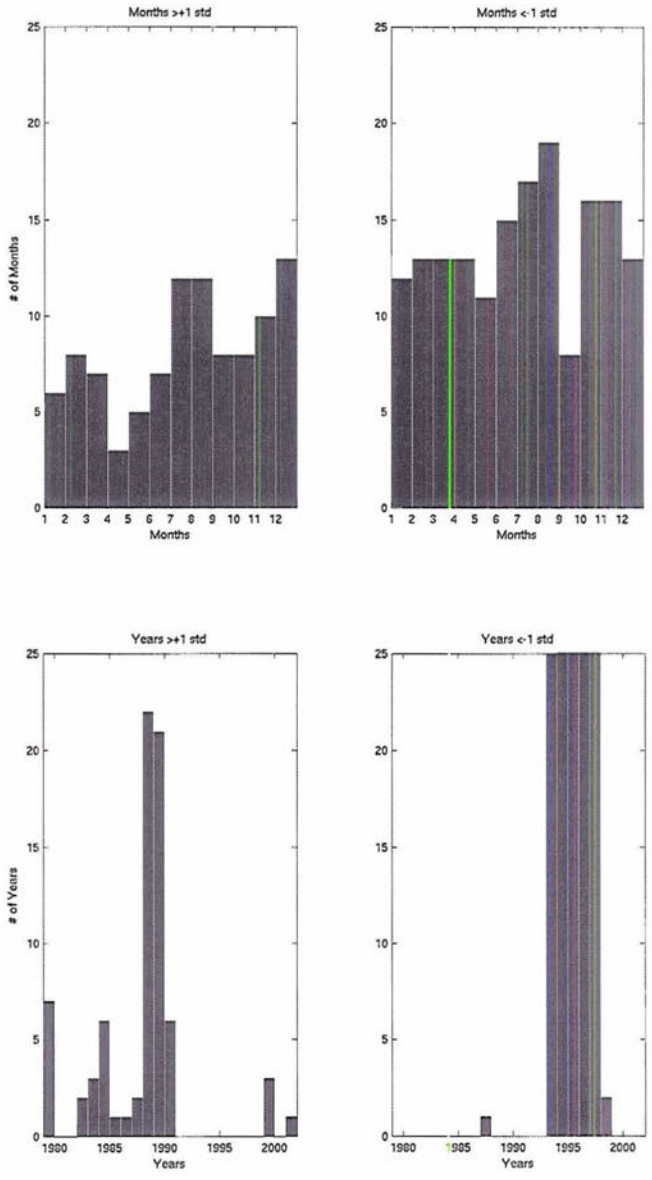

Figure 4.10 Histograms of (top) months used in composite analysis and (bottom) years used in composite analysis, for PSA CO_2 days >+1std (left) and <-1std (right).

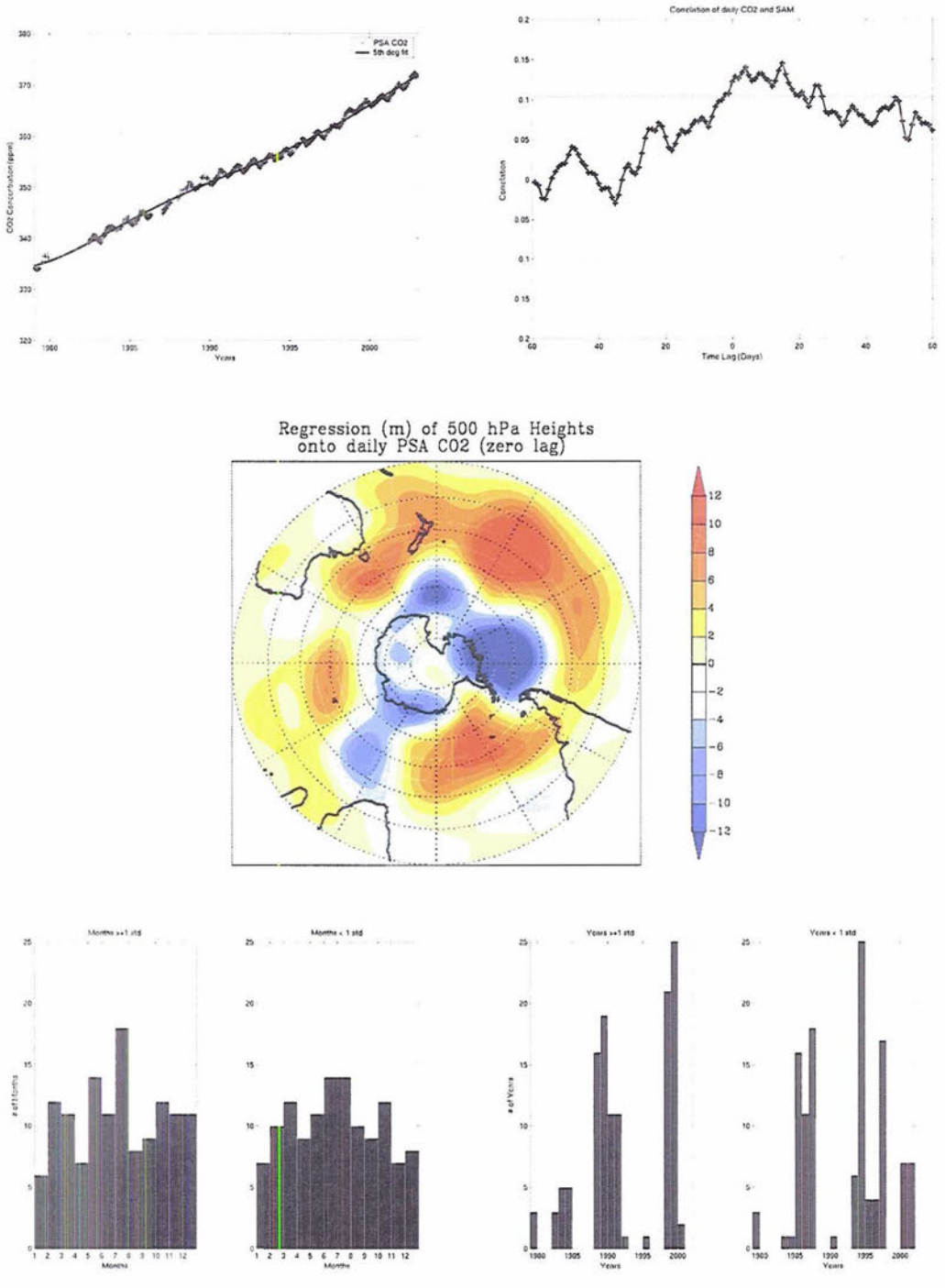

Figure 4.11 (top left) Same as in Figure 4.7 (top), but using a 5th-degree polynomial fit for the trend instead of the global linear trend. (top right) Lag correlation of daily CO_2 anomalies (5th-degree fit removal) at PSA and the daily SAM index. Negative lags imply CO_2 leading the SAM. (middle) Regression (m/std) of 500-hPa height field onto daily PSA CO_2 anomalies that were de-trended using 5th-degree polynomial fit. (bottom left & right) Same as in Figure 4.10, but from composite using 5th-degree polynomial fit removal.

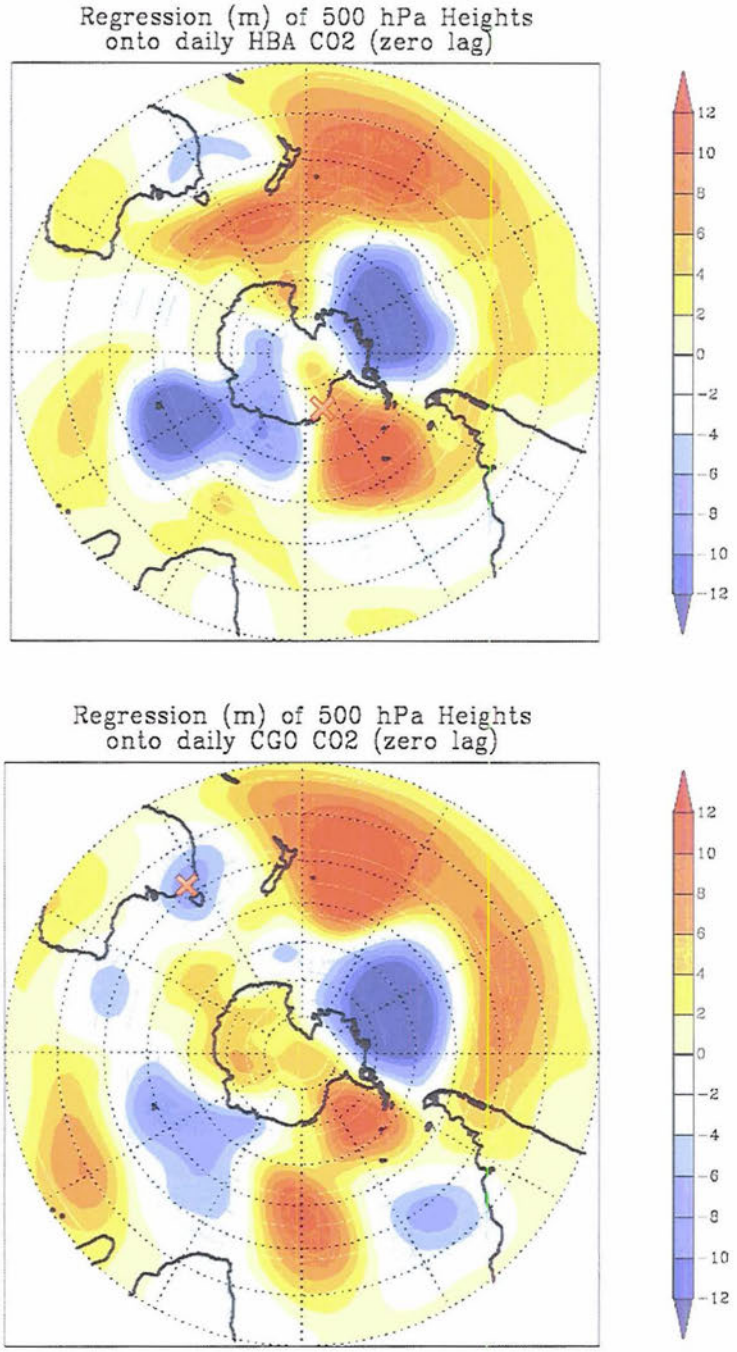

Figure 4.12 (top) Regression of 500-hPa height field onto the standardized daily Halley Bay (HBA) CO_2 anomalies (de-trended with 5th-degree polynomial fit) at zero lag. HBA is marked with a red 'x'. (bottom) Regression of 500-hPa height field onto the standardized daily Cape Grim (CGO) CO_2 anomalies (de-trended with 5th-degree polynomial fit) at zero lag. Units are meters/standard deviation of CO_2. CGO is marked with a red 'x'.

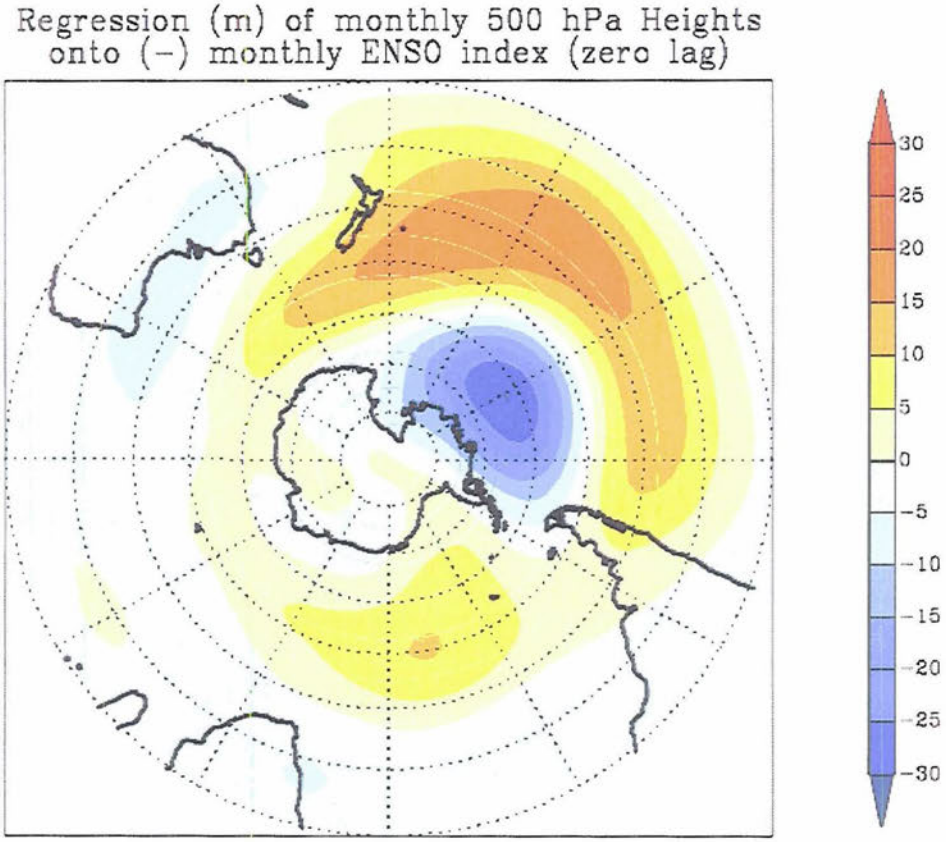

Figure 4.13 Regression of monthly 500-hPa height field onto the standardized monthly ENSO index (inverted) at zero lag. Units are meters/standard deviation of ENSO.

CHAPTER 5: TRANSCOM MONTHLY MEAN CO_2 FLUX ESTIMATES

The relationship between the TransCom monthly mean interannual CO_2 flux estimates and large-scale climate patterns has yet to be studied in depth. In this chapter, we first provide some background analysis on the flux estimates themselves and then compare our results with previous studies. However, our main focus in this chapter is the analysis of the relationships between TransCom flux estimates and the ENSO, NAM, and SAM indices. The TransCom estimates allow us to examine how CO_2 fluxes over large regions may be influenced by climate, which is useful considering the sparse spatial sampling of observational CO_2 stations.

5.1 Background Analysis of TransCom Monthly Mean CO_2 flux

In this section, we examine the long-term mean of the total fluxes as well as the variance and trends of the flux anomalies in order to better understand the properties of the flux estimates from each TransCom region. This analysis will provide background information that may be useful when considering the relationships between the flux estimates and large-scale climate patterns later in this chapter.

5.1.1 The Long-term Mean of Total Fluxes

As a reminder of the names and locations of the 22 different TransCom regions, we suggest the reader refer to Figure 2.2. In order to get a sense of what regions are CO_2 sources or sinks over a long time period, we calculate the long-term mean of the total

fluxes (seasonal cycle is NOT removed, but fossil fuel emissions ARE removed) from 1980-2002, shown in Figure 5.1 in Gt C yr^{-1}. In general, NH land regions (temperate North America, boreal Asia, and Europe) tend to be a sink of CO_2, while the tropics (East Pacific, tropical Asia, tropical Atlantic, tropical Indian, and South Africa) tend to be a source of CO_2. The tropical oceans are expected to be a source of CO_2 due to the upwelling of nutrient-rich waters in those regions [*Feely et al.*, 1999]. Tropical land regions may be a source of CO_2 due to deforestation or forest fires [*Houghton*, 2003; *Rodenbeck et al.*, 2003]. However, increased photosynthesis from CO_2 fertilization as well as re-growth of previously deforested areas in tropical land regions may act to cancel out the source [*DeFries et al.*, 2002; *Rodenbeck et al.*, 2003], which may explain why the long-term mean of the tropical America region is approximately zero. Both the SH and NH mid- to high-latitude oceans are also generally sinks of CO_2, which is also expected due to the subduction of colder water (which is more soluble to CO_2) in the subtropics.

The numeric values corresponding to Figure 5.1 as well as recently published values from *Baker et al.* [2005] are given in Table 5.1. Note that the values from *Baker et al.* correspond to averages across 1991-2000, so in the table we include '91-'00 averages as well as the '80-'02 averages. Differences between our results and *Baker et al.* most likely arise from the difference in the number of stations used in the inversion model runs. Because the network of stations used in the inversion must stay continuous over time in order to not induce spurious jumps in the results, we are only using 23 stations for the period of 1980-2002, while *Baker et al.* is able to use 78 stations from 1991-2000. The 23 stations used in our inversion model and their locations are given in Table 5.2. In particular, we are lacking stations over most tropical land regions and many

ocean regions. Clearly, we may be at a disadvantage by using fewer stations; however, it is important in our analysis of relationships to large-scale climate patterns to use the longest record possible. Thus, we are sacrificing spatial coverage for temporal coverage.

The regions that have the largest differences with *Baker et al.*'s results (shown in bold in the table) for the '91-'00 time period are temperate North America, tropical America, temperate South America, and Northern Africa. We also have oppositely signed flux estimates in the South Pacific region. The large differences in amplitude and sign between our results may be due to these regions being poorly constrained. The *Baker et al.* results are most likely better constrained in these regions since they have more station data available to them. While our total global CO_2 flux estimates (land + ocean) are similar (~3.1 Gt C yr^{-1} uptake), the partitioning between land and ocean uptake is very different. We find an almost equal terrestrial and oceanic sink, while *Baker et al.* find a terrestrial sink that is almost double the oceanic sink. This discrepancy may be due to fewer stations over NH extra-tropical continents (where a major land sink is hypothesized to exist [*Tans et al.*, 1990]) during our 1980-2002 inversion time frame than during the 1991-2000 time frame, which may cause the underestimation of the terrestrial land sink; or equally possible, our lack of stations over oceanic regions may result in an overestimation of the oceanic sink (no shipboard measurements are included in our inversion).

Although our results do not agree exactly with *Baker et al.* [2005], examining the long-term means of the total fluxes and comparing them with a more highly-constrained result gives a sense of the reliability of the fluxes in different regions. The reliability of

the different regions will be important when we study relationships between the flux estimates and large-scale climate patterns later in this chapter.

The seasonality of the long-term mean CO_2 flux is explored in Figure 5.2, which shows the April through September long-term mean (top) and the October through March long-term mean (bottom). During the April to September season (NH summer), all NH land regions are a CO_2 sink due to photosynthesis exceeding respiration during those months. South Africa and Temperate South America are CO_2 sources because in the SH winter, respiration exceeds photosynthesis (the flux from Australia behaves differently, suggesting that photosynthesis is not the dominant control on the seasonality of the flux in that region). The October to March season (NH winter) corresponds with a change in sign for all land fluxes (except for Tropical Asia, where the length of the day stays relatively constant throughout the year). Oceanic fluxes do not exert as much seasonality as land fluxes, although the South Pacific is only a significant sink from April to September and the Southern Ocean from October to March.

5.1.2 Variance of Flux Anomalies

Figure 5.3 illustrates the variance of the flux anomalies (the seasonal cycle has been removed). The highest variances occur over land regions, which agrees with previous research that finds the variability of land fluxes to be much greater than that of ocean fluxes [*Bousquet et al.*, 2000; *Le Quere et al.*, 2003]. In our analysis, the largest variances occur in the regions of boreal and temperate Asia, South America, temperate North America, tropical America, and South Africa. The large variability in tropical and South America and Africa is thought to be associated with the ENSO cycle [*Rodenbeck et al.*, 2003].

The oceanic regions have the lowest variances. Of the ocean regions, the variance is largest in the tropical Indian and South Pacific Ocean regions. Surprisingly, the equatorial Pacific has a very low variance, which disagrees with previous findings from both observations and ocean and atmosphere models which find that this region has the most variability of the ocean regions [*Feely et al.*, 1999; *Le Quere et al.*, 2000; *Rodenbeck et al.*, 2003]. Most likely, the variance of the equatorial Pacific in our results is underestimated due to the complete lack of stations in our data set located in that region (refer to Table 5.2).

5.1.3 Trends in Flux Anomalies

The trends in the flux anomalies are shown in Figure 5.4. There are positive trends for the temperate North America, tropical America, and South Pacific regions (as well as a slightly positive trend in the East Pacific Ocean). Stronger negative trends occur in the regions of boreal Asia and South Africa, while slightly negative trends occur in the regions of boreal North America, North Africa, temperate South America and Asia, West Pacific, tropical and South Atlantic, and the Northern ocean.

Several authors have noted a small trend towards greater oceanic uptake of CO_2 over time, as seen here for almost every ocean region except the South and East Pacific. The explanation for this trend is that due to increased atmospheric CO_2 concentrations, the ocean continues to take up CO_2 emitted in past decades because the oceanic CO_2 is not in equilibrium with the atmosphere [*Le Quere et al.*, 2003]. *Le Quere et al.* [2003] compared atmospheric inversions and ocean models and found in common a larger oceanic sink in the 1990s than in the 1980s, yielding a global oceanic trend between 0.1 to 0.6 Gt C yr^{-1} per decade. Our results indicate trends closer to 0.1 Gt C yr^{-1} per decade

for specific ocean regions. The strong positive trend over the South Pacific seems out of place, but this region is poorly constrained (there are no observational stations in this region).

5.2 Relationships between TransCom CO_2 flux estimates and the ENSO index

Since the response of CO_2 in various regions of the world to the ENSO cycle has been more researched (using observations and models) than the response to the NAM or the SAM, we will begin with this relationship so that we can compare our results to previous findings. Hopefully, this analysis will serve as a means of judging how reliable these flux estimates are when using them to look for relationships with large-scale patterns of variability.

Figure 5.5 illustrates the lag correlations between the 22 TransCom regions and the ENSO index for the period 1980-2002. We note that these correlations and significance levels do not take into account any uncertainties in the flux estimates. Lag zero represents the start of an ENSO event so that negative lags imply that the CO_2 flux is leading ENSO. From this figure we can see that the regions of North Africa (3 months), temperate Asia (4 months), tropical America (-9 months), East Pacific Ocean (1 month), temperate South America (2 months), South Indian Ocean (3 months), and South Atlantic Ocean (4 months) have significant correlations at the given lags with the ENSO index. The best correlation at lag -9 months for tropical America may be an artifact of the periodic nature of the ENSO cycle. At the lag of the best correlation for these regions, only tropical America and the East Pacific Ocean have negative correlations with ENSO, implying CO_2 uptake associated with a warm ENSO event. Figure 5.5 generally agrees with previous research on this subject [*Keeling et al.*, 1989; *Feely et al.*, 1999] that

suggests that the initial response after a warm ENSO event is the reduction of upwelling in the eastern Pacific Ocean (leading to anomalous CO_2 uptake there) followed by higher temperatures and decreased precipitation over land (leading to an anomalous terrestrial source of CO_2). It is not entirely clear why the South Indian or South Atlantic Ocean regions should have significant positive correlations with ENSO, although warmer temperatures associated with a warm ENSO event in these regions could lead to warmer SSTs and decreased solubility of CO_2.

Figure 5.6 shows the composite of CO_2 flux estimates 3 months after (top) months when ENSO exceeds 1 standard deviation and (bottom) months when ENSO exceeds -1 standard deviation. A lag of 3 months is chosen because of the high number of significant correlations at that time lag, as discussed above. In the case of warm ENSO events (top), there are large sources of CO_2 from all tropical land regions, such as tropical America, tropical Asia, North Africa, South Africa, and Australia, as well as from temperate Asia and temperate South America. The North Pacific, South Indian, and Southern Ocean are also sources of CO_2 to the atmosphere. The East Pacific and South Pacific, as well as boreal Asia and temperate North America, are sinks of CO_2. Note that the only regions that have mean flux estimates that are significantly different from the mean flux from non-El Niño months are temperate Asia, South Africa, and South America (marked with a red 'x'). This result generally agrees with Figure 5.5 at a 3 month lag; however, it is surprising that the South Indian or South Atlantic Oceans do not show up as significant in this composite. This suggests that these regions have significant correlations with ENSO at 3 months but are not significantly different from the non-El Niño mean flux in that region for that lag.

For cold ENSO events (bottom), the mean CO_2 flux for almost every region changes sign from the warm ENSO composite, except for the Southern Ocean and boreal North America (a few regions don't change sign but change to essentially zero, such as tropical America). This result is encouraging because the composites are based on two different sample sets but yield nearly the same information. In this composite, only temperate Asia has a mean CO_2 flux following a cold ENSO event that is significantly different from non-La Niña months. Fewer regions may be significant in the cold ENSO event composite because these events are typically weaker than warm ENSO events.

We compare our results with previous findings shown in Figure 5.7. *Jones et al.* (2001) used a coupled climate-carbon cycle model to find the distribution of anomalous CO_2 fluxes (gC m^{-2} yr^{-1}) for mean El Niño conditions and mean La Niña conditions, shown in Figure 5.7 (top). Most of our results compare reasonably well to theirs. For warm ENSO events, we both find anomalous uptake over the East Pacific Ocean, boreal Asia, and temperate North America, and we both find anomalous sources over tropical America, South Africa, and tropical Asia. Their fluxes also switch sign almost everywhere for cold ENSO events. However, we differ over some of the ocean regions; where they find uptake from the North Pacific and tropical Indian Oceans during El Niño, we find a source of CO_2 from these regions. They also observe the highest amplitude response from tropical America and South America, whereas we see the largest response from temperate South America, temperate Asia, and South Africa. These differences in amplitude may be a result of the fact that they are using area-weighted units (gC m^{-2} yr^{-1}) whereas we are not (Gt C yr^{-1}). Overall, though, it is encouraging that the flux results

from a process-based model agree so well with inversion estimates that are based on observed CO_2 measurements.

In order to compare our results to another atmospheric inversion, we examine the findings from *Rodenbeck et al.* (2003), shown in Figure 5.7 (bottom). They averaged the inversion flux anomaly estimates for an El Niño event from June 1997 to May 1998 and a La Niña event from October 1998 to September 1999. During the El Niño event, they also see the largest amplitude response, also using area-weighted units, in the form of an anomalous source from the tropical and South America regions. Other sources occur in the tropical Asia, Australia, and tropical and South Indian Ocean regions, in agreement with our results. Also in agreement are the anomalous sinks of CO_2 in boreal Asia and most of temperate North America. However, they find CO_2 uptake in South Africa and all of the Atlantic Ocean regions, whereas we see sources in these regions. They also find almost no flux from the East Pacific region, whereas both our results and *Jones et al.* (2001) show uptake in this region (in agreement with observations). During the La Niña event, almost all their fluxes change sign except for South Africa, temperate North America, and the tropical Indian Ocean (we see a sign change for all these regions).

We would like to note that TransCom estimates are based on the average of 13 inversion model results while these two studies are based on individual models, lending robustness to the TransCom results shown in Figure 5.6 that the other studies lack. Nonetheless, one thing this comparison makes clear is that for many regions around the globe the CO_2 flux following an ENSO event remains uncertain. The only regional CO_2 flux anomalies that all three analyses agree on is the large source from the tropical Asia and tropical America region after an El Niño event, most likely due to higher

temperatures leading to increased plant respiration there. We also all find varying degrees of uptake from temperate North America and boreal Asia. Therefore, we conclude that while using the TransCom inversion flux estimates for this type of analysis can be beneficial and produce realistic results, we must remain aware that not all results are trustworthy.

5.3 Relationships between TransCom CO_2 flux estimates and the NAM index

In this section we investigate the sinks and sources of the TransCom flux estimates that are associated with the NAM. The 12-month lag correlations between the TransCom CO_2 flux estimates and the NAM index are shown in Figure 5.8. In the NH (top), where we expect the influence of the NAM on the carbon flux to be greatest, temperate North America, boreal North America, boreal Asia, and the North Atlantic Ocean are significantly correlated to the NAM 5 months after a NAM event. For a high-index NAM event, temperate North America is a source of CO_2 while boreal North America, boreal Asia, and the North Atlantic are sinks. Temperate Asia is also a significant sink of CO_2 1 month after a high-index NAM event. These results generally agree with the theory that a high-index NAM event has a stronger than normal polar vortex, leading to fewer cold outbreaks and warmer temperatures over high-latitude Northern Hemisphere land regions that results in an advance of spring budburst, a longer growing season, and thus higher annual CO_2 drawdown by the terrestrial biosphere [*Russell and Wallace*, 2004]. The source from temperate North America may be a result of the warmer temperatures and decreased precipitation in that region associated with a high-index NAM [*Hurrell*, 1995; *Thompson et al.*, 2000], leading to higher plant respiration.

Patra et al. [2005] recently examined the correlations between inversion flux estimates and the NAM from 1994-2001. The authors found a significant positive correlation between the boreal North American flux anomalies and the NAM, and a significant negative correlation between the boreal Asia flux anomalies and the NAM, at a lag of 5 months for each correlation. Our lag of best correlation agrees well with their results, but we find a sink in boreal North America where they see a source. This disagreement may reflect the differences in available station data; *Patra et al.* [2005] used 87 stations whereas we use only 23 stations.

Somewhat more inexplicable in our results are the significant correlations of North Africa, tropical America, tropical Asia, South America, and the Southern Ocean up to a year before a NAM event. Tropical Asia, tropical America, South America, Australia, the West Pacific Ocean, and the Southern Ocean are also significantly correlated with the NAM 5-8 months after a NAM event, even though we would expect these regions to be too far away from NAM's center of action to be affected very much. It is possible that since the NAM isn't entirely independent of the ENSO or SAM that these high correlations simply reflect the impact of another pattern of variability on the southern regional fluxes concurrent with a high-index NAM event, or that these high correlations happened by chance.

Because the strongest NAM events generally occur in the Northern Hemisphere winter, we will now focus on the impacts of the mean January-February-March (JFM) NAM on seasonal flux anomalies. We only look at the JFM and AMJ flux anomalies in this thesis, as they seem to offer the most physical results. Figure 5.9 (top) shows the correlations between the mean JFM flux anomalies and the mean JFM NAM for each

region. For a high-index NAM event, we find a significant source of CO_2 in the boreal Asia and boreal North America regions, and significant sinks in Europe, North Africa, and the North Atlantic Ocean. Temperate Asia and North America act as smaller, less significant sinks. These results agree with the Chapter 4 finding that high CO_2 days at Barrow (located in the boreal North America region) are associated at lag zero with a pattern similar to the high-index NAM. The fairly large correlations in the South Pacific and Australia regions are unexpected.

Figure 5.9 (bottom) shows the correlations between the mean April-May-June (AMJ) flux anomalies and the mean JFM NAM. We find CO_2 sinks over most of the NH high-latitude land regions and a source from temperate North America following a wintertime high-index NAM event. This finding agrees well with *Russell and Wallace* [2004] in the sense that the late spring/early summer CO_2 fluxes are affected by the wintertime NAM, and that CO_2 uptake is enhanced over the NH high-latitudes following a high-index NAM event. As noted above, the source from temperate North America may be a result of the decreased precipitation and higher temperatures there. However, significant correlations occur only for Europe in the NH, and also for Australia and tropical America, regions that are far from the centers of action of the NAM. Moreover, regions that we would expect to be significant such as boreal Asia or North America are not significant. It's possible that the strong signal in these regions at a lag of 5 months (shown in Figure 5.8) is simply being averaged out in the three-month mean.

We try to elucidate the terrestrial flux results by comparing them in Figure 5.10 to the correlations of the mean JFM NAM and (a) the mean JFM and (b) mean AMJ Normalized Difference Vegetation Index (NDVI). The NDVI is an index that quantifies

the concentration of green leaf vegetation around the globe [*Tucker*, 1980; *Tucker et al.*, 2005]. Note that the color bar in Figure 5.10 has been reversed so that increased plant growth corresponds to the increased CO_2 uptake in Figure 5.9. In Figure 5.10 (a), we find that the JFM NDVI is very positively correlated the JFM NAM in Europe (in particular, the 95% significance plot shows the greatest spatial coverage over Europe). This implies that the increased concentration of plants in Europe associated with a high-index NAM event may be responsible for the significant uptake that we see in that region in Figure 5.9 (a). Why a high-index NAM event corresponds with higher than normal plant concentration in the NH winter most likely has to do with the milder winters in Europe also associated with this polarity of the NAM. Decreased snow cover may also play a role. A similar agreement between the vegetation and the flux anomalies occurs in North/Central Africa. Disagreements occur in boreal and temperate North America, and may suggest that the concentration of plant life associated with the JFM NAM is *not* responsible for the associated JFM flux anomaly. For boreal, temperate, and tropical Asia, it is difficult to tell whether the NDVI correlations Figure 5.10 (a) agree with the flux anomaly correlations due to the mottled appearance of the NDVI correlations.

In Figure 5.10 (b), we see that a high-index JFM NAM event is generally associated in the following spring (AMJ) with higher than normal concentrations of green leaf vegetation over the boreal NH land regions, particularly boreal Asia and Europe, and lower concentrations over temperate North America. Therefore, at least for the NH land regions, the mean AMJ CO_2 sources and sinks shown in Figure 5.9 (b) correspond with regions of increased or decreased plant concentrations, in agreement with the theory from

Russell and Wallace [2004]. The correspondence between these two data sets adds credence to the relationship between the TransCom flux estimates and the NAM.

Most of the above findings are reasonable, but unfortunately there are several problematic results as well. These flux anomaly correlations in Figure 5.9 do not always agree with the correlations to the NDVI in Figure 5.10, so for these regions it is unlikely that they can be explained by changes in vegetation associated with the NAM. It is difficult to know what other factors may be responsible for the terrestrial fluxes if not the plant cover (variations in soil respiration is one potential factor). Also, the fact that the flux estimates from certain regions far from the center of action of the NAM have significant correlations while regions closer to the NAM do not serve as a reminder that these results are suggestive at best.

5.4 Relationships between TransCom CO_2 flux estimates and the SAM index

Now that we have illustrated the strengths and weaknesses of using the TransCom flux estimates to look for relationships of CO_2 flux to the ENSO and the NAM, we complete this chapter by exploring the less-researched relationship between CO_2 flux and the SAM. Figure 5.11 shows the 12-month lag correlations between the SAM and the CO_2 flux estimates for every region. We are particularly interested in the SH regions (bottom plot) because they are nearest to the strongest amplitudes of the SAM signal. South America, South Africa, South Indian Ocean, and South Atlantic Ocean are all significant anomalous sinks of CO_2 ~3-5 months after a high-index SAM event. Moreover, they all have similar lag correlation curves, although it's possible that this similarity could be due to the fact that several of these regions are not independent of each other (namely South America, South Africa, and the South Atlantic Ocean). An

encouraging result is the similar but opposite-in-sign lag correlation of the Southern Ocean.

Recall that a high-index SAM event is hypothesized to influence air-sea flux via the associated increase in westerly winds south of 50°S, leading to anomalous equatorward Ekman drift and increased upwelling along the Antarctic coast, thereby increasing the CO_2 outgassing and resulting in a source of atmospheric CO_2 by the ocean south of 50°S. Above 50°S, anomalous easterly winds drive poleward Ekman drift, increasing the convergence and downwelling of surface water near 50°S and reducing upwelling, leading to an anomalous CO_2 sink [*Hall and Visbeck*, 2002; *Lovenduski and Gruber*, 2005]. Our results generally agree with this hypothesis, showing a CO_2 sink for the majority of the regions north of 50°S and a CO_2 source for the Southern Ocean. Only the South Pacific Ocean disrupts this pattern as a source north of 50°S, but we note from Figure 5.12 that the westerly wind anomalies over the Southern Ocean associated with the SAM extend into the South Pacific region and that the anomalous easterlies in the South Pacific are very weak compared to easterlies in the other regions north of 50°S. This wind difference may explain the source of CO_2 for this region.

We now compare these findings with the results from Chapter 3 (Figure 3.9) that show a significant uptake of CO_2 compared to the global mean (the "departure CO_2") 3-7 months after a high-index SAM event for stations south of 30°S. It is encouraging that the shape of the lag correlations for the South America, South Africa, South Indian Ocean, and South Atlantic Ocean regions look very similar to the shape of the lag correlation for the departure CO_2. Nevertheless, we see an anomalous source from the Southern Ocean and the South Pacific in this analysis but anomalous uptake at every

station south of 30°S in the departure CO_2 analysis. Perhaps these regions really are an anomalous source of CO_2 following a high-index SAM event but a sink relative to the global mean.

Referring back to Figure 5.11, we note once again the strong correlations in tropical regions (East Pacific Ocean, tropical Asia and America) and NH regions (Europe, temperate North America, boreal North America and Asia, and even the Northern Ocean!) where we wouldn't expect the amplitude of the flux response to a SH phenomena to be so strong. As suggested before, these high correlations may be due to chance or to the slight dependence of the SAM on other large-scale patterns of variability.

Figure 5.13 illustrates the correlation between the SAM index and the regional flux anomalies 5 months later. We choose to examine the 5 month lag because the correlations in the SH regions are greatest around this lag. As we noted in Figure 5.11 (bottom), the South Pacific and Southern Oceans are significant anomalous sources of CO_2 at this lag while South America, South Indian Ocean, and South Atlantic Ocean are significant anomalous sinks. Inexplicably, tropical Asia and Europe also have significant correlations at this lag.

5.5 Conclusion

It is difficult to assess why we occasionally find surprisingly significant correlations far from the sources of the change in atmospheric circulation throughout this analysis, or at lags prior to the circulation event. Nonetheless, many of this chapter's results seem reasonable and agree with previous findings or theories. For example, the locations of the sources and sinks following an ENSO event seem reasonable and agree in

most respects with previous model results and observations. We also see NH spring flux anomalies following the wintertime NAM that agree with the hypothesis in *Russell and Wallace* [2004]. In the SH, the SH flux anomalies following a SAM event also agree with a previous hypothesis described in *Lovenduski and Gruber* [2005]. Certainly these results suggest that using the TransCom flux estimates can be useful for studying the interannual variability of the carbon cycle on a global scale, particularly if we have an *a priori* hypothesis with which to test the physicality of the results.

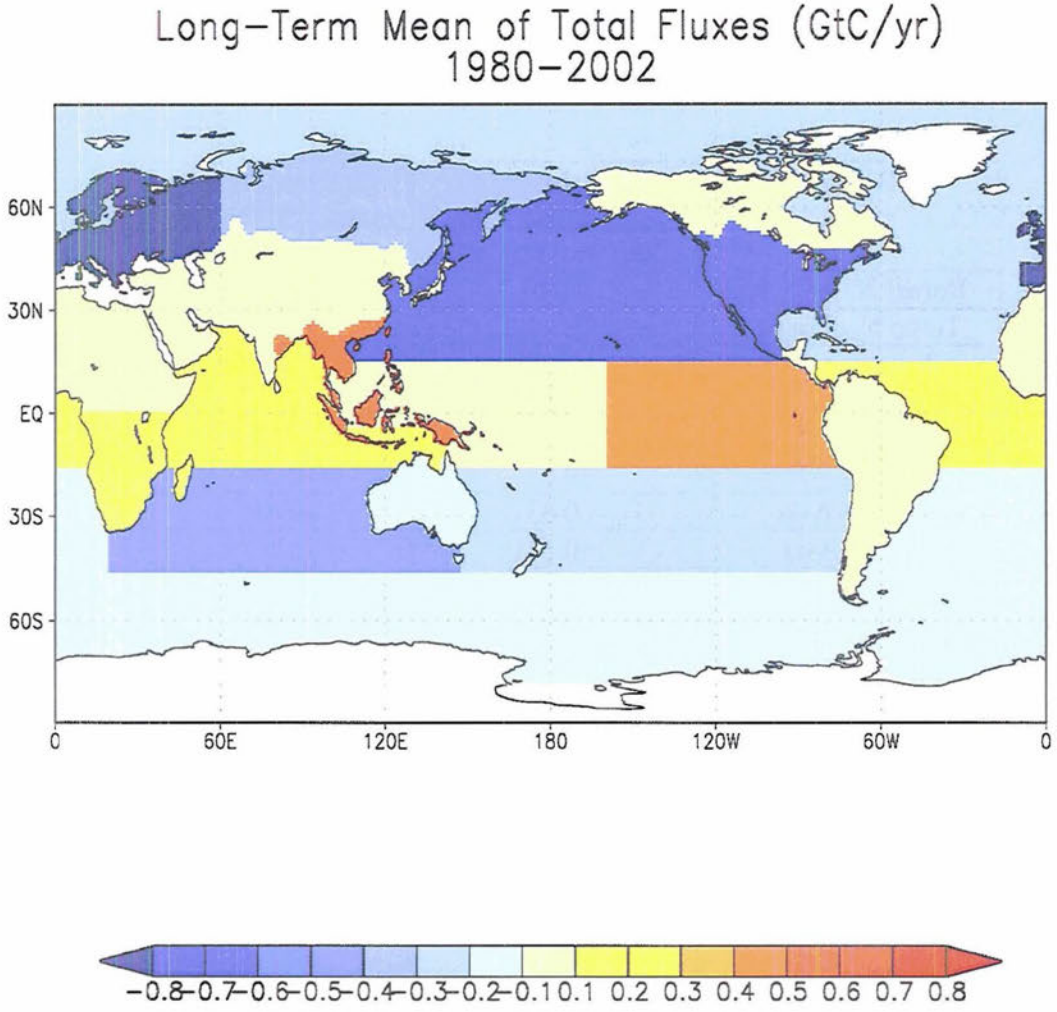

Figure 5.1 Long-term mean of total fluxes (fossil fuels have been removed, but NOT the seasonal cycle). Units are Gt C yr^{-1}.

Table 5.1 Long-term mean of total fluxes (seasonal cycle included) for the 22 TransCom regions (Gt C yr^{-1}), as well as the global totals. Second column from *Baker et al.* [2005]. Regions with the largest difference (≥0.5 Gt C yr^{-1}) between Baker et al. and our results are in bold.

Region	Baker '05 long-term mean ('91-'00) in Gt C yr^{-1}	Our long-term mean ('91-'00) in Gt C yr^{-1}	Our long-term mean ('80-'02) in Gt C yr^{-1}
Boreal N. America	0.14	0.01	0.06
Temp N. America	-1.11	**-0.51**	-0.71
Trop America	1.07	**0.04**	**-0.05**
Temp S. America	-0.64	**0.06**	**0.10**
Northern Africa	0.50	**-0.03**	0.06
Southern Africa	-0.62	-0.20	**0.20**
Boreal Asia	-0.33	-0.46	-0.34
Temp Asia	-0.31	-0.02	-0.04
Trop Asia	0.29	0.47	0.53
Australia	-0.11	-0.09	-0.15
Europe	-0.97	-0.85	-0.89
N. Pacific	-0.56	-0.68	-0.70
W. Pacific	-0.11	-0.03	0.03
E. Pacific	0.57	0.45	0.42
S. Pacific	0.09	-0.18	-0.28
Northern Ocean	-0.22	-0.29	-0.27
N. Atlantic	-0.29	-0.27	-0.24
Trop Atlantic	0.09	0.09	0.13
S. Atlantic	-0.21	-0.12	-0.10
Southern Ocean	-0.25	-0.21	-0.15
Trop Indian	0.24	0.08	0.17
S. Indian	-0.41	-0.39	-0.42
Global land	-2.09	-1.58	-1.23
Global Ocean	-1.06	-1.55	-1.41
Global Total	-3.15	-3.13	-2.64

Table 5.2 The 23 stations, and their respective TransCom regions, used for the inversion model run in our analysis. Stations with "x2" have both discrete and continuous measurements from that station (which brings the total to 23).

Station	Location	Latitude	Longitude
Alert (ALT)	Canada	82.45° N	62.52° W
Amsterdam Island (AMS)	South Indian Ocean	37.95° S	77.53° E
Ascension Island (ASC)	Tropical Atlantic Ocean	7.92° S	14.42° W
Azores (AZR)	North Atlantic Ocean	38.77° N	27.38° W
Baring Head (BHD)	New Zealand		
Barrow (BRW) x2	Alaska	71.32° N	156.60° W
Mt. Cimone (CMN)	Italy	44.18° N	10.70° E
Guam, Mariana Islands (GMI)	West Pacific Ocean	13.43° N	144.78° E
Key Biscayne (KEY)	Florida	25.67° N	80.20° W
Cape Kumukahi (KUM)	North Pacific Ocean	19.52° N	154.82° W
Mauna Loa (MLO) x2	North Pacific Ocean	19.53° N	155.58° W
Niwot Ridge (NWR)	Colorado	40.05° N	105.58° W
Palmer Station (PSA)	Antarctica	64.92° S	64.00° W
Schauinsland (SCH)	Germany	47.92° N	7.90° E
Seychelles (SEY)	Tropical Indian Ocean	4.67° S	55.17° E
Matatula Point, Samoa (SMO) x2	West Pacific Ocean	14.24° S	170.57° W
South Pole (SPO) x2	Antarctica	89.98° S	24.80° W
Station "M" (STM)	Northern Ocean	66.00° N	2.00° E
Station "M" extended baseline condition (STMEBC)	Northern Ocean	66.00° N	2.00° E

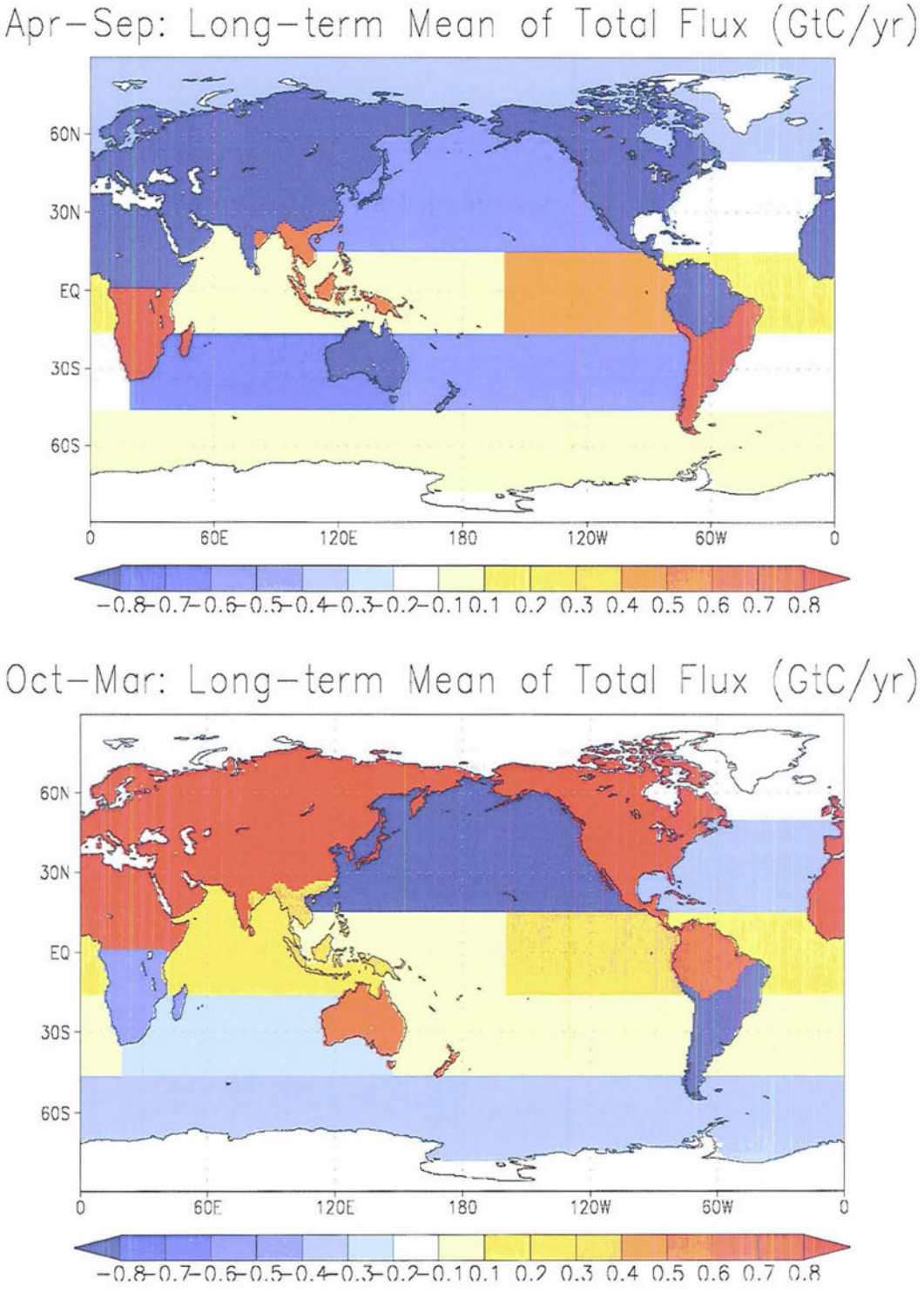

Figure 5.2 (top) April-October long-term mean of the total flux (Gt C yr^{-1}) and (bottom) October- March long-term mean of the total flux (Gt C yr^{-1}).

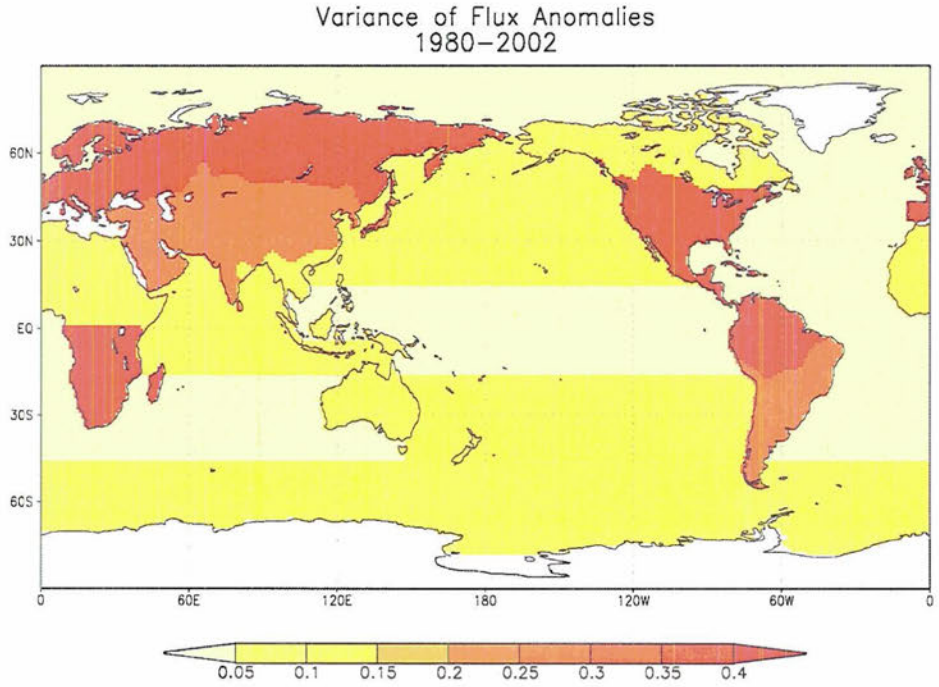

Figure 5.3 The variance of the flux anomalies (seasonal cycle removed) from 1980-2002. Units are in $(\text{Gt C yr}^{-1})^2$.

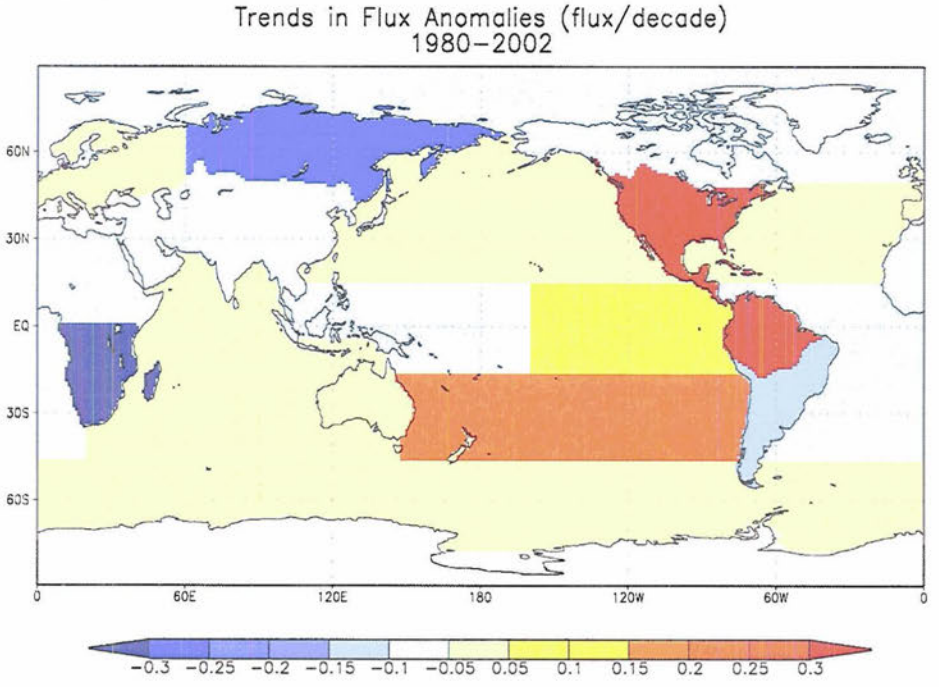

Figure 5.4 Trends in flux anomalies (seasonal cycle removed) from 1980-2002. Units are in flux (Gt C yr^{-1}) per decade.

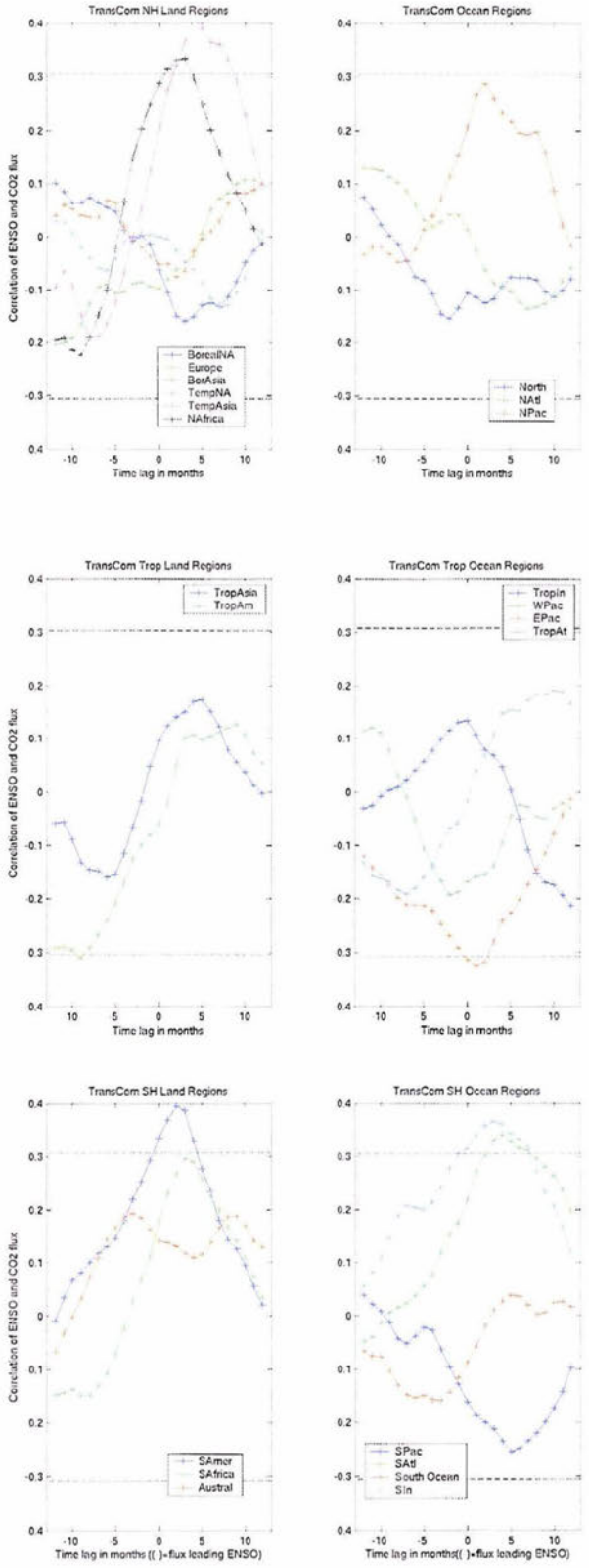

Figure 5.5 Lag correlations between the ENSO index and CO_2 flux estimates for all 22 TransCom regions, 1980-2002. Negative lags imply CO_2 flux leading ENSO. (top) NH regions (middle) Tropical regions, (bottom) SH regions. Land regions are on the left and ocean regions are on the right. 95% confidence intervals are marked according to the *t*-statistic (dashed lines).

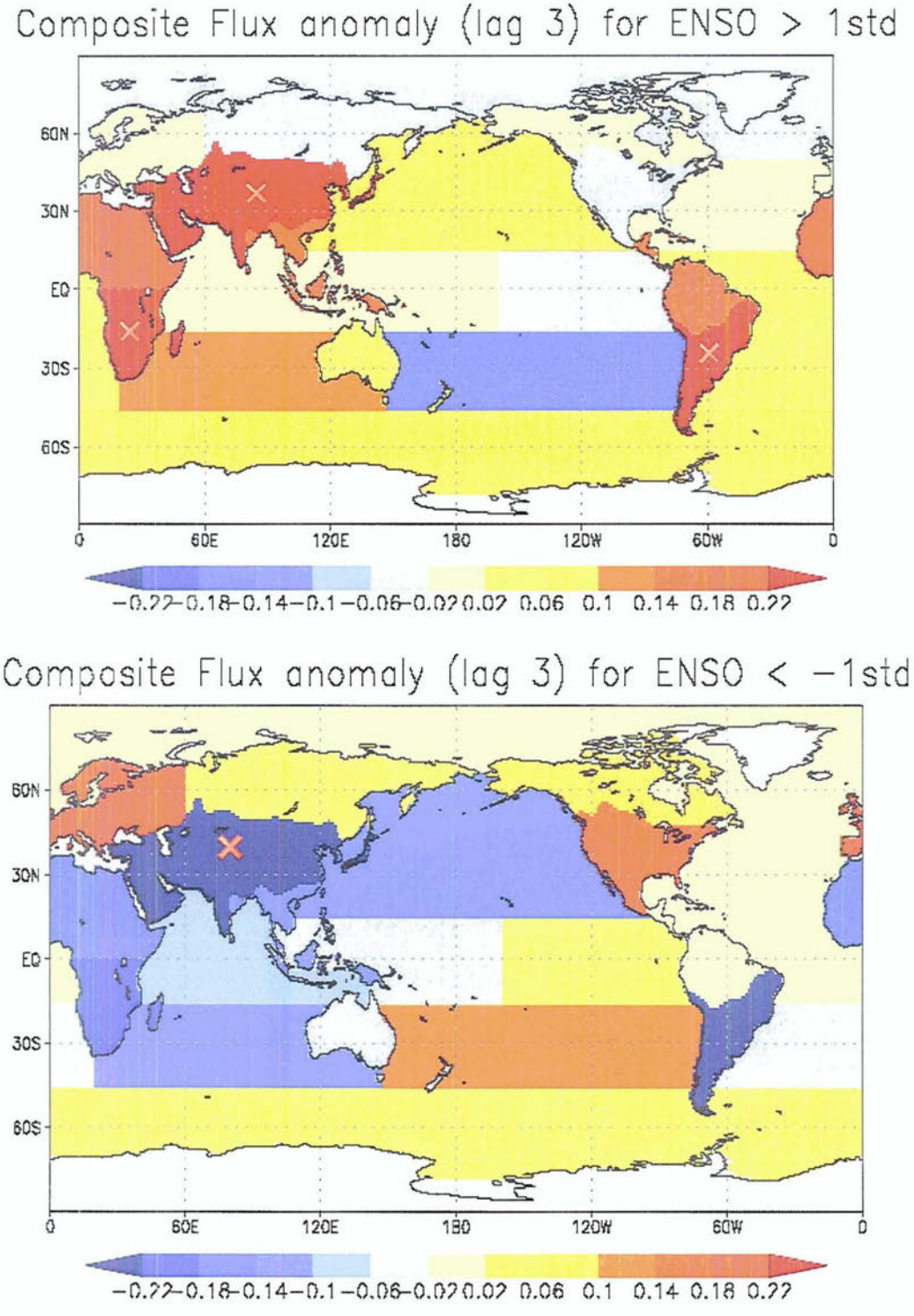

Figure 5.6 Composite of the TransCom flux anomaly estimates (1980-2002) 3 months following (top) ENSO exceeding 1 standard deviation and (bottom) ENSO exceeding -1 standard deviation. Units are in Gt C yr^{-1}. Mean flux values that are significantly different from non-El Niño or non-La Niña time periods are marked with a red 'x'.

(top)

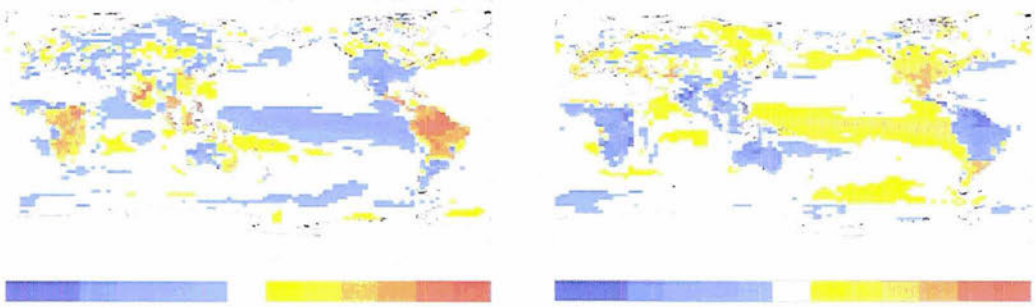

(bottom)

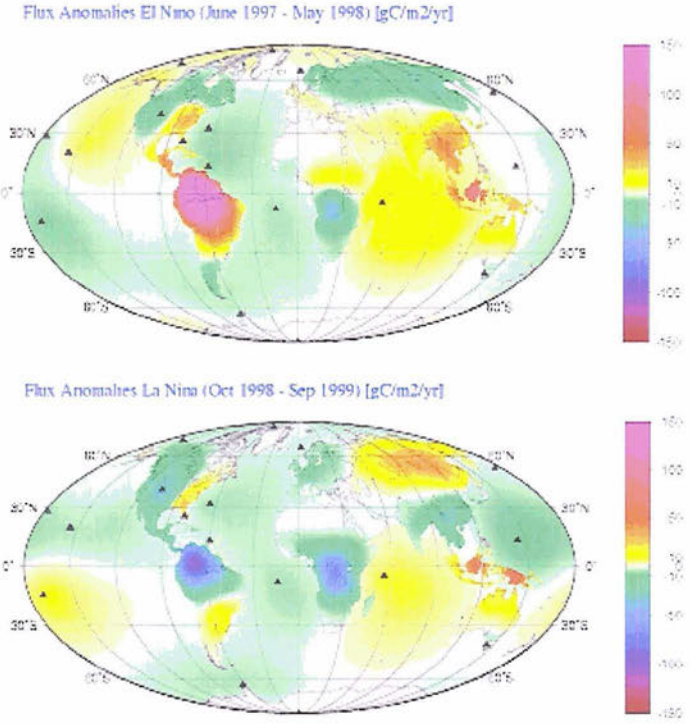

Figure 5.7 Flux anomaly estimates during ENSO events from 2 previous studies. (top) from *Jones et al.* (2001), coupled climate-carbon cycle model results, in units of gC m^{-2} yr^{-1}, for mean El Niño conditions and mean La Niña conditions. (bottom) from *Rodenbeck et al.* (2003), atmospheric inversion results, in units of gC m^{-2} yr^{-1}, averaged over the 1997/1998 El Niño and the 1998/1999 La Niña.

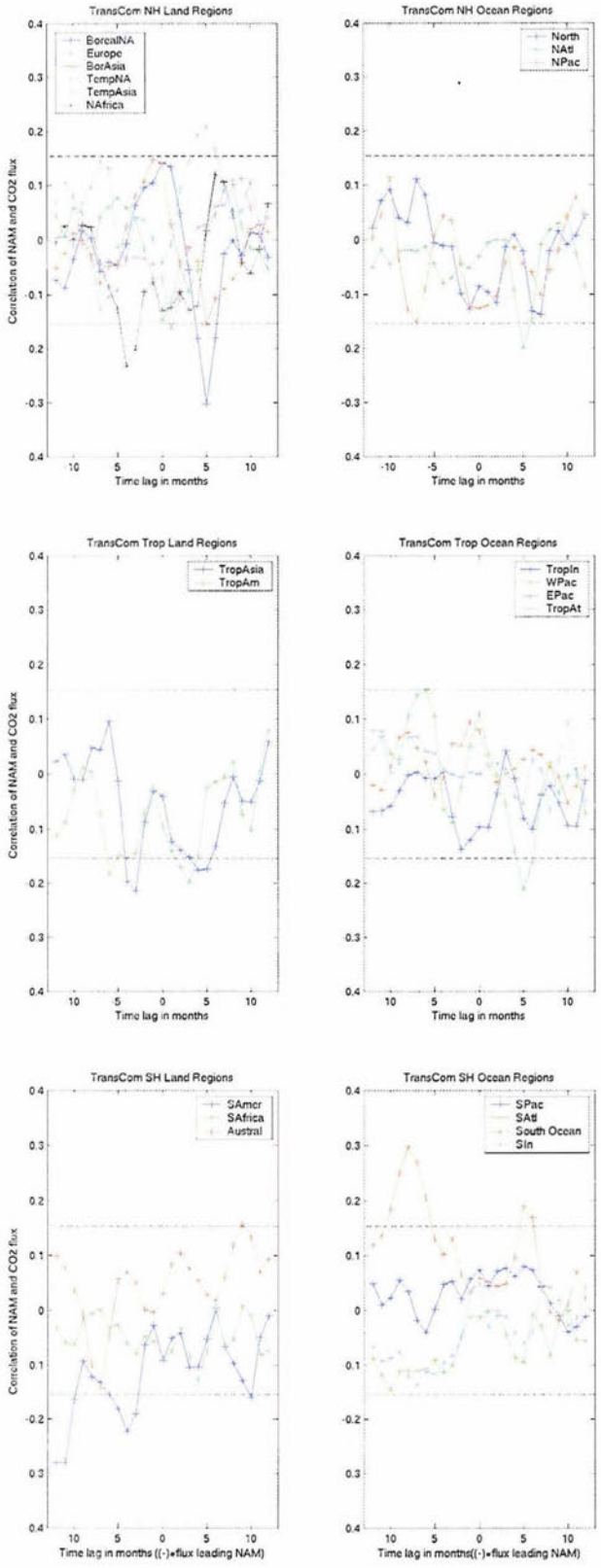

Figure 5.8 Lag correlations between the NAM index and CO_2 flux estimates for all 22 TransCom regions, 1980-2002. Negative lags imply CO_2 flux leading NAM. (top) NH regions (middle) Tropical regions, (bottom) SH regions. Land regions are on the left and ocean regions are on the right. 95% confidence intervals are marked according to the *t*-statistic (dashed lines).

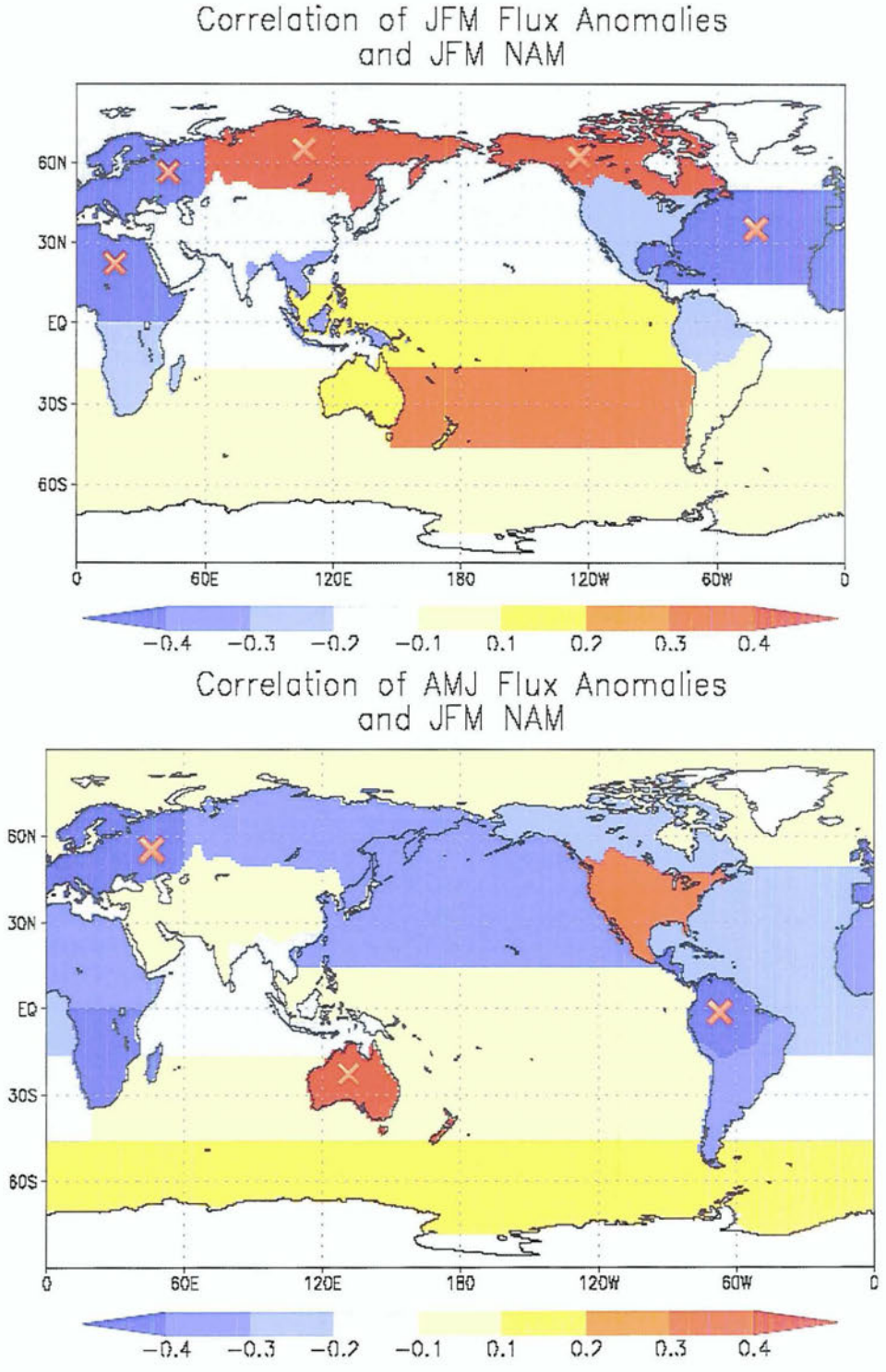

Figure 5.9 Correlations between the mean-JFM NAM (1980-2002) and (top) mean-JFM flux anomalies and (bottom) mean-AMJ flux anomalies. Correlations that exceed the 95% significant level according to the *t*-statistic are marked with a red 'x'.

(a)

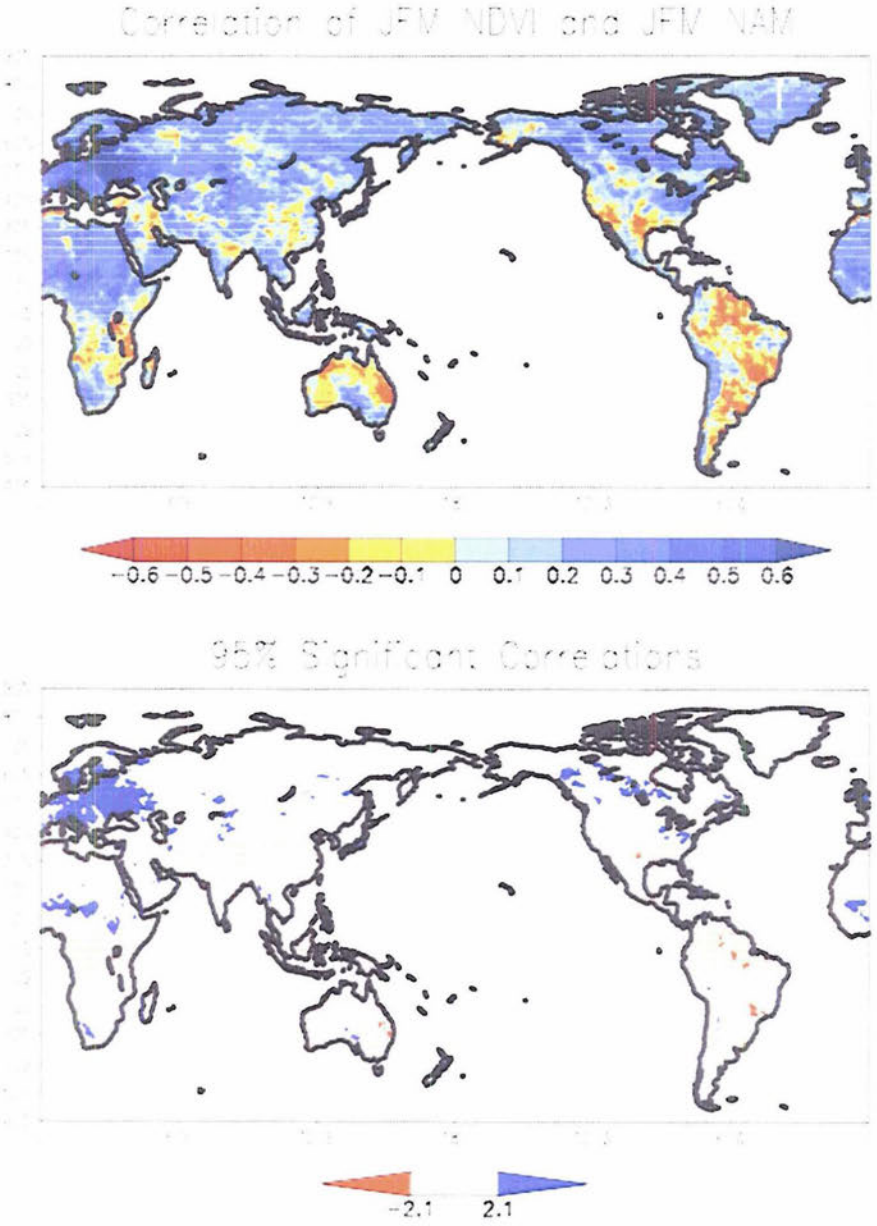
Correlation of JFM NDVI and JFM NAM
-0.6 -0.5 -0.4 -0.3 -0.2 -0.1 0 0.1 0.2 0.3 0.4 0.5 0.6
95% Significant Correlations
-2.1
2.1

(b)

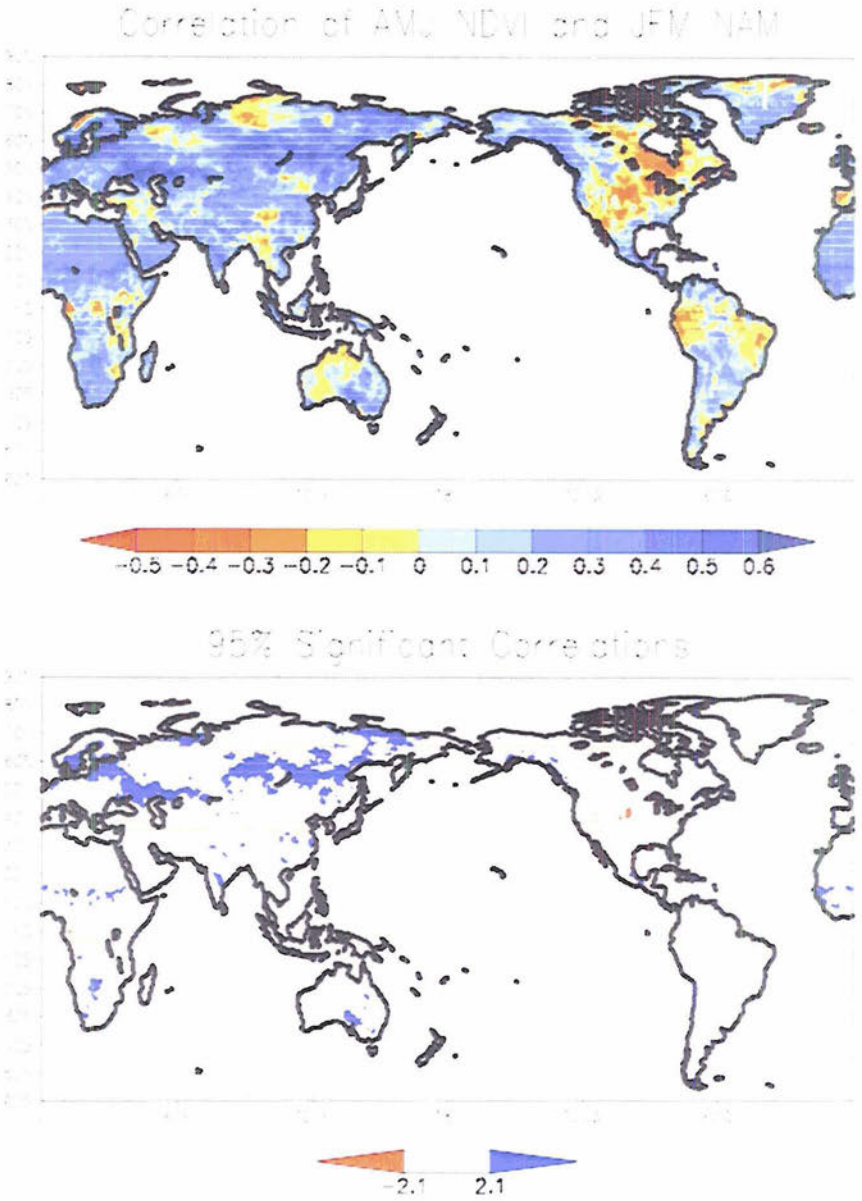

Figure 5.10 (a) The correlation of the mean JFM NAM and (top) the mean JFM NDVI (bottom) and the 95% significantly correlated regions (1981-2001). Note that the color bar has been reversed to match Figure 5.9: more plants (dark blue) means more uptake (blue in Figure 5.9). (b) The correlation of the mean JFM NAM and (top) the mean AMJ NDVI (bottom) and the 95% significantly correlated regions (1981-2001). Values on significance color bar denote t-statistic value for the 95% level. (Note: horizontal red lines are caused by conversion to PDF and are not representative of data).

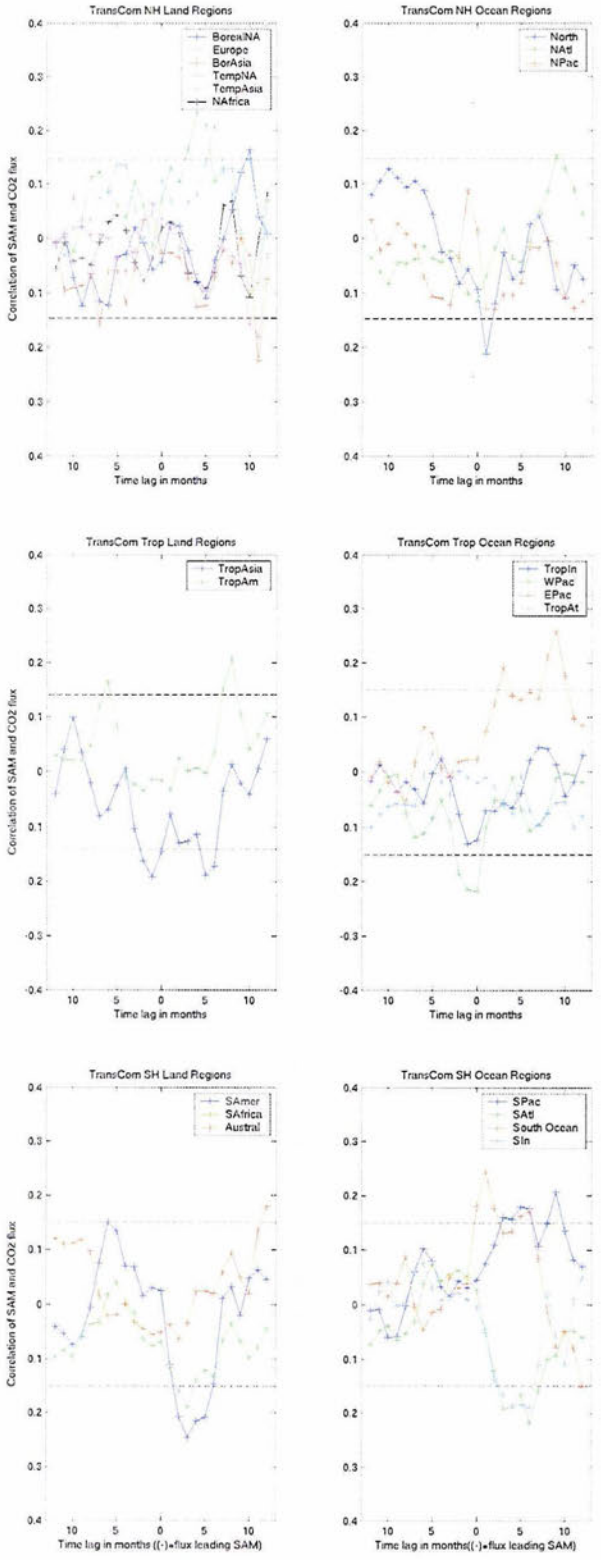

Figure 5.11 Lag correlations between the SAM index and CO_2 flux estimates for all 22 TransCom regions, 1980-2002. Negative lags imply CO_2 flux leading the SAM. (top) NH regions (middle) Tropical regions, (bottom) SH regions. Land regions are on the left and ocean regions are on the right. 95% confidence intervals are marked according to the *t*-statistic (dashed lines).

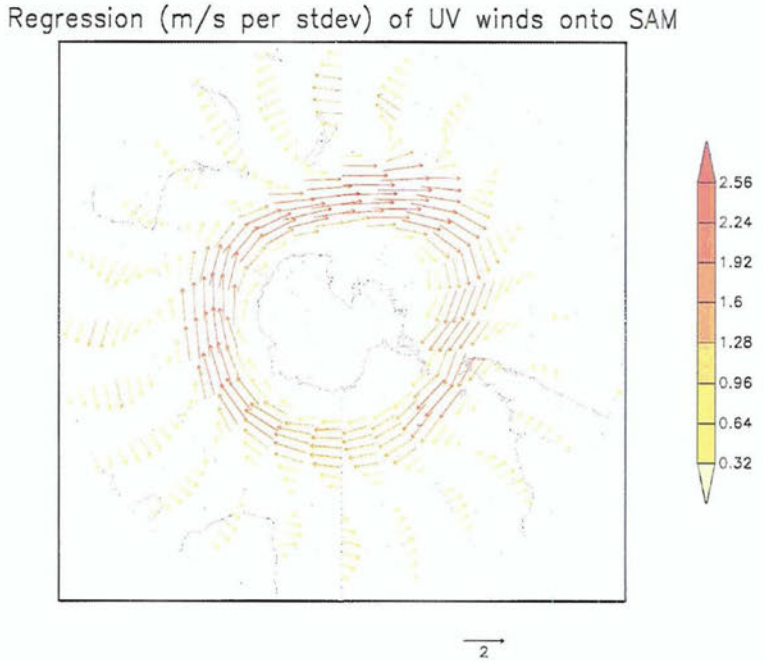

Figure 5.12 The regression of the zonal and meridional winds at 925 mb onto the SAM index, 1980-2002. Units are m/s per standard deviation of the SAM. The colors indicate magnitude, not direction, of the wind vectors.

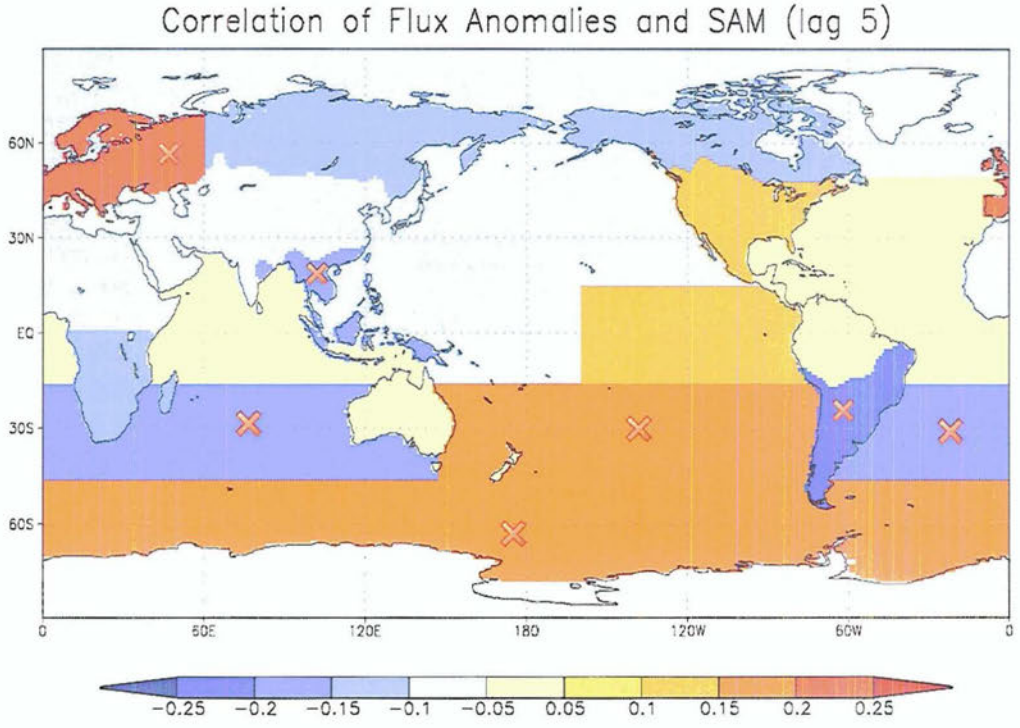

Figure 5.13 Correlations between the CO_2 flux anomalies and the SAM index at lag 5 months (SAM leading the flux). Correlations that exceed the 95% significant level according to the *t*-statistic are marked with a red 'x'.

CHAPTER 6: CONCLUSIONS

We conclude this thesis with a summary of our key findings and a discussion about potential future work.

Most previous studies focusing on the relationship of the carbon cycle to large-scale climate patterns have examined the potential link between the El Niño Southern Oscillation and the global carbon cycle. ENSO is thought to significantly impact both oceanic [*Feely et al.*, 1999] and terrestrial CO_2 fluxes [*Keeling and Revelle*, 1985]. Far fewer studies have been published concerning relationships between the Northern and Southern Annular Modes and atmospheric CO_2. Because these patterns account for a substantial percentage of the variance in surface conditions, such as temperature, precipitation, and wind, they may have significant influence on carbon fluxes over both the land and the oceans. The intent of this thesis was to examine how changes in atmospheric CO_2 may be related to all three patterns of large-scale variability, with an emphasis on the annular modes. In the next three sections, we briefly review the findings for each relationship.

6.1 Relationship between ENSO and atmospheric CO_2

Previous findings suggest that an initial decrease in atmospheric CO_2 tendency anomalies occurs near the beginning of a warm ENSO event followed by a large increase in CO_2 tendency anomalies several months later [*Keeling et al.*, 1989; *Elliot et al.*, 1991; *Conway et al.*, 1994; *Rayner et al.*, 1999]. The initial decrease is thought to be due to the

reduction in oceanic upwelling during a warm ENSO event, causing a decrease in outgassing of CO_2 to the atmosphere [*Feely et al.*, 1999]. The subsequent increase in the CO_2 tendency following a warm ENSO event is thought to be a result of warmer temperatures and decreased precipitation, resulting in higher soil and plant respiration and an increase in forest fires, and thus a terrestrial biosphere source of CO_2 [*Keeling and Revelle*, 1985]. The biospheric effect is thought to be greater than the oceanic effect, so that the net result of a warm ENSO event is an anomalous increase of CO_2 to the atmosphere.

We examined this relationship using observed monthly mean CO_2 data from MLO. In agreement with theory, we found that a 95% significantly positive correlation occurs with ENSO leading the CO_2 tendency by 3-7 months (Figure 3.5), implying an increase of atmospheric CO_2 following a warm ENSO event. The time lag is partially due to the time of transport from the tropical land and ocean regions (where the effect of ENSO is strongest) to MLO. We also looked at the relationship between ENSO and TransCom regional CO_2 flux estimates using correlation and composite analysis in Figures 5.5 and 5.6. We found that 3 months after a warm ENSO event, there are large sources of CO_2 from all tropical land regions, while the East Pacific and South Pacific are sinks of CO_2. These results compared reasonably well to previous findings, suggesting that using the TransCom inversion flux estimates for this type of analysis can be beneficial and produce realistic results.

6.2 Relationship between the NAM and atmospheric CO_2

In theory, a high index NAM would imply a stronger polar vortex, leading to fewer cold outbreaks over high-latitude Northern Hemisphere land regions and warmer

temperatures over much of Siberia, northern Europe, and parts of Canada, allowing an advance of spring budburst and a longer growing season and thus higher annual CO_2 drawdown by the terrestrial biosphere [*Russell and Wallace*, 2004]. We looked for this relationship of the wintertime NAM to the spring CO_2 flux in several different analyses.

Using monthly mean CO_2 tendency anomalies at BRW, we found a significant negative correlation for the NAM leading the CO_2 tendency by 4-7 months (Figure 3.7), which agrees remarkably well with the theory that the NAM's influence on northern boreal climate will take several months to drive anomalous atmospheric CO_2 uptake through changes in the terrestrial biosphere. By breaking up the data into seasonal averages, we found that this relationship is strongest between the JFM NAM and spring and summer CO_2 tendency anomalies.

We then used daily CO_2 concentration data at BRW to obtain a greater sample size than we had in the monthly record. Lag correlations between the daily BRW CO_2 and the NAM show the largest significant positive correlations 7-10 days after a NAM event (Figure 4.1), suggesting that a high-index NAM may be associated with advection of CO_2-enriched air into BRW on short time scales. However, the fact that the correlations are significant at almost all lags suggests that the relationship between the daily BRW CO_2 and the NAM is likely dominated by timescales greater than ~60 days, which indicates that these results do not necessarily reflect only advection. Note that the daily CO_2 *concentration* anomaly results cannot be directly compared to the monthly mean CO_2 *tendency* anomaly results discussed above. We also regressed the 500-hPa height field onto the daily BRW CO_2 concentration anomalies (lag zero) in order to look for robust patterns in the circulation that occur for high or low CO_2 days (Figure 4.2).

The regression pattern suggests that high CO_2 days at BRW are associated with upper level circulation patterns that resemble the high-index NAM. However, at other stations in the NH, regression patterns are not NAM-like but indicate local advection may be the major driver of changes in CO_2 concentrations on short time scales.

Finally, in Figure 5.8 we investigated the sinks and sources of the TransCom flux estimates that are associated with the NAM. We found that 5 months after a high-index NAM event, boreal North America and boreal Asia are anomalous sinks of CO_2. This finding agrees with the relationship between the NAM and the monthly mean BRW CO_2 tendency anomalies discussed above, as well as with theory. Therefore, most of our results suggest that the wintertime high-index NAM is associated with anomalous CO_2 uptake in the NH boreal regions during the following spring, while on shorter time scales, local changes in advection may be the likely cause of changes in CO_2 concentrations at NH stations. At BRW, the changes in advection may be directly associated with the circulation of the NAM.

6.3 Relationship between the SAM and atmospheric CO_2

The SAM is thought to impact atmospheric CO_2 via air-sea flux exchange due to lack of nearby land regions with significant vegetation in the Southern Hemisphere. The major hypothesis described in this thesis is that a high-index SAM event leads to increased westerly winds south of 50°S, driving anomalous equatorward Ekman drift and increased upwelling along the Antarctic coast, thereby increasing the CO_2 outgassing and resulting in an anomalous source of atmospheric CO_2 by the ocean south of 50°S [*Lovenduski and Gruber*, 2005]. However, this source may be diminished due to the anomalously cold and iron-rich water being drawn up to the surface, which increases CO_2

solubility as well as phytoplankton productivity. The cancellation between mechanisms implies that changes in the CO_2 flux driven by the SAM may be hard to observe [*Lovenduski and Gruber*, 2005]. North of 50°S, anomalous easterly winds drive fluxes in the opposite sense.

The lag correlation between the monthly mean CO_2 tendency anomalies at PSA and the SAM showed no significant relationship at any lag (Figure 3.6), but once the ENSO signal was removed via linear fitting, a significant positive correlation occurred at lag zero (Figure 3.8). It is difficult to say whether this positive correlation is due to either changes in advection that might bring CO_2-enriched air into PSA or the anomalous outgassing along the Antarctic coast associated with a high-index SAM, described in the theory above, or both.

Because removing the ENSO signal produced useful results in the SH but did not remove other global signals like volcanic eruptions, we developed the concept of the "departure CO_2" time series, which is the CO_2 tendency minus the global mean tendency. We found that the best correlation for the SH stations south of 30°S occurs with a high-index SAM event leading anomalous uptake of the departure CO_2 tendency by 3 months (Figure 3.9). While this result is not consistent with theory or with Figure 3.8, we lack understanding of what the departure CO_2 physically represents. Perhaps, as hypothesized, there is outgassing of CO_2 south of 50°S following a positive SAM event, but uptake of CO_2 relative to the global mean. Therefore, we are cautious about these findings.

Similar to the monthly mean tendency analysis, correlations between the SAM and the daily CO_2 concentration anomalies at PSA did not show any significant

relationship when the CO_2 concentrations were de-trended using the global mean linear trend (Figure 4.7). We tried removing the 5th-degree polynomial fit instead to broaden the sampling distribution and to filter out lower-frequency influences like ENSO and Pinatubo. Significant positive correlations then occur for up to ~15 days after a SAM event, suggesting that a high-index SAM is associated with higher-than-normal CO_2 days at PSA up to 2 weeks later (Figure 4.11). The regression of the 500-hPa height field onto the daily PSA CO_2 anomalies (5th-degree fit removed) at zero lag has a slight resemblance to the SAM, and the location of PSA at the gradient between high and low heights implies advection into the station. However, at other SH stations, the regression patterns only share a "wave train" pattern of anomalously high and low heights across the South Pacific Ocean and the Antarctic Peninsula, comparable to the regression of 500-hPa heights onto the ENSO index (Figure 4.12). This suggests that ENSO may still be dominating the CO_2 signal at SH stations despite the use of the 5th-degree fit. The dependence of the results on the method of trend removal and the weakness of the patterns even after some manipulation further substantiate our belief that the relationship of the SAM to atmospheric CO_2 is either small or difficult to observe in the observations due to mitigating effects of local CO_2 flux.

Lastly, we looked at the lag correlations between the TransCom flux estimates and the SAM in Figure 5.11. This figure shows that South America, South Africa, South Indian Ocean, and South Atlantic Ocean are all significant anomalous sinks of CO_2 ~3-5 months after a high-index SAM event, while the Southern and South Pacific Oceans are anomalous sources. These results generally agree with the stated hypothesis, showing an

anomalous CO_2 sink for the majority of the regions north of 50°S and an anomalous CO_2 source for the Southern Ocean.

Hence, we can conclude that in most of our analyses, a relationship between the SAM and atmospheric CO_2 is difficult to detect. However, if we remove ENSO or low-frequency variability, we generally find that a high-index SAM is associated with anomalously high CO_2 concentrations near the Antarctic coast, with TransCom estimates indicating anomalously low CO_2 concentrations north of 50°S. These results agree with the stated theory. Nonetheless, it is difficult to deduce whether this relationship results from local changes in flux or from local changes in advection.

6.4 Future Work

While this thesis provides an initial step towards understanding the relationships between large-scale patterns of variability and the global carbon cycle, much work remains to be done. Our findings suggest that while there is a clear relationship between the wintertime NAM and the springtime CO_2 flux, the relationship between the SAM and CO_2 is much weaker. Future work may involve investigating why this relationship is so weak.

Because CO_2 fluxes due to dynamic, thermal, and biological processes in the Southern Ocean may cancel each other out [*Lovenduski and Gruber*, 2005], it may be useful to look at atmospheric oxygen in the form of the O_2/N_2 ratio (measuring O_2 variations alone is difficult due to the high O_2 content of air). Thermal and biological effects on O_2 in the ocean tend to reinforce rather than oppose each other [*Keeling and Shertz*, 1992], so variations of air-sea flux due to the SAM may be easier to detect using this data.

In this thesis we have only examined surface CO_2 concentrations. Future research may include examining vertical variations of CO_2 driven by the NAM and the SAM. While CO_2 is well-mixed up to ~100 kilometers [*Hartmann*, 1994], variations about the mean mixing ratio value could potentially be caused by changes in the zonal mean winds, associated with the annular modes, that may be advecting more or less CO_2-enriched air into the column. Several stations in the CMDL network have vertical profiles of CO_2.

Because the annular modes vary on relatively short time scales (e-folding timescales ~10 days [*Feldstein*, 2000]), more thorough studies could be done on the relationships of CO_2 to the NAM and SAM using more recent CMDL stations with shorter data records. For stations with daily records, even 5 years of data may be enough to examine relationships to these climate patterns. There are also a few stations with continuous data records, which would significantly boost the sample size.

Additionally, future work could further explore the usefulness of the TransCom CO_2 flux estimates for finding global relationships to large-scale patterns of variability. This may entail using sensitivity studies to understand which fraction of the observed CO_2 concentrations are caused by fluxes out of each of the 22 TransCom regions. This analysis would help us to understand, for example, whether the observed concentrations at PSA are caused more by oceanic or terrestrial fluxes. More work also remains to be done on how the uncertainty in the flux estimates affects the significance of the relationships in each region.

6.5 Final Thoughts

As found by *Cai et al.* [2003] and others, models show that under increasing CO_2 concentrations, the SAM displays an upward trend. The NAM may also exhibit an

increasing trend under such conditions but the response is more variable from one climate model to another. Therefore, information regarding the impact of the annular modes on CO_2 is necessary to close the feedback loop. For example, if the NAM is tending toward its high-index phase due to increasing CO_2 concentrations, then the increase in CO_2 may be slightly mitigated by the association of the high-index NAM with enhanced carbon uptake in the boreal NH spring (if we oversimplify and assume that this is the net effect over the course of the year), causing a negative feedback effect.

Human beings can affect their environment in many ways, but the rapid increase of CO_2 due to fossil fuel burning and land-use change will undoubtedly affect the future world in which we live. In particular, the 1.5°-4.5°C surface temperature increase for a doubling of CO_2 (including feedback effects) [*IPCC*, 2001] could have potentially devastating effects on the global environment. While the changes in CO_2 concentrations due to modulation by climate change is thought to be small compared to the overall increase from anthropogenic emissions, there is substantial uncertainty in projections of future CO_2 concentrations due to the uncertainty about the effects of climate change on processes determining land and ocean uptake of CO_2 [*IPCC*, 2001]. Therefore, our ability to accurately predict global temperature changes may be improved by understanding the feedbacks between the large-scale patterns of variability and atmospheric CO_2.

REFERENCES

Bacastow, R.B., 1976: Modulation of atmospheric carbon dioxide by the Southern Oscillation. *Nature*, **261**, 116-118.

Bacastow, R.B., J.A. Adams, C.D. Keeling, D.J. Moss, T.P. Whorf, and C.S. Wong, 1980: Response of atmospheric carbon dioxide to the weak 1975 El Niño. *Science*, **210**, 66-68.

Baker, D.F., R.M. Law, K.R. Gurney, P. Rayner, P. Peylin, A.S. Denning, P. Bousquet, L. Bruhwiler, Y.-H. Chen, P. Ciais, I.Y. Fung, M. Heimann, J. John, T. Maki, S. Maksyutov, K. Masarie, M. Prather, B. Pak, S. Taguchi, and Z. Zhu, 2005: TransCom 3 inversion intercomparison: Impact of transport model errors on the interannual variability of regional CO_2 fluxes, 1988-2003. Accepted to *Glob. Biogeochem. Cycles*, 2005.

Baldwin, M.P. and T.J. Dunkerton, 1999: Stratospheric harbingers of anomalous weather regimes. *Science*, **294**, 581-584.

Bergh, J., S. Linder, T. Lundmark, and B. Elfving, 1999: The effect of water and nutrient availability on the productivity of Norway spruce in northern and southern Sweden. *Forest Ecology and Management*, **119**, 51-62.

Bjerknes, J., 1969: Atmospheric teleconnections from the equatorial Pacific. *Monthly Weather Review*, **97**, 163-172.

Bousquet, P., P. Peylin, P. Ciais, C. Le Quere, P. Friedlingstein, and P.P. Tans, 2000: Regional changes in carbon dioxide fluxes of land and oceans since 1980. *Science*, **290**, 1342-1346.

Bretherton, C.S., M. Widmann, V.P. Dymnikov, J.M. Wallace, and I. Blade, 1999: The effective number of spatial degrees of freedom of a time-varying field. *J. Climate*, **12**, 1990-2009.

Buermann, W., B. Anderson, C.J. Tucker, R.E. Dickinson, W. Lucht, C.S. Potter, and R. B. Myneni, 2003: Interannual covariability in Northern Hemisphere air temperatures and greenness associated with El Niño-Southern Oscillation and the Arctic Oscillation. *J. Geophys. Res.*, **108**, doi:10.1029/2002JD002630.

Cai, W., P.H. Whetton, and D.J. Karoly, 2003: The response of the Antarctic Oscillation to increasing and stabilized atmospheric CO_2. *J. Climate*, **16**, 1525-1538.

Caspersen, J.P., S.W. Pacala, J.C. Jenkins, G.C. Hurtt, P.R. Moorcroft, and R.A. Birdsey, 2000: Contributions of land-use history to carbon accumulation in U.S. forests. *Science*, **290**, 1148-1151.

Cess, R.D., et al., 1993: Uncertainties in carbon dioxide radiative forcing in atmospheric general circulation models. *Science*, **262**, 1252-1255.

Chen, T.-C. and M.-C. Yen, 1997: Interdecadal variation of the Southern Hemisphere circulation. *J. Climate*, **10**, 805-812.

Conway, T.J., P.P. Tans, L.S. Waterman, and K.W. Thoning, 1994: Evidence for interannual variability of the carbon cycle from the National Oceanic and Atmospheric Administration/Climate Monitoring and Diagnostics Laboratory Global Air Sampling Network. *J. of Geophys. Res.*, **99**, 22831-22855.

DeFries, R.S., Houghton, R.A., Hansen, M.C., Field, C.B., Skole, D., and Townshend, J., 2002: Carbon emissions from tropical deforestation and regrowth based on satellite observations for the 1980s and 1990s. *Proc. Nat. Acad. Sc. USA*, **99**, 14256-14261.

Delmas, R.J., J.-M. Ascencio, and M. Legrand, 1980: Polar ice evidence that atmospheric CO_2 20,000 BP was 50% of present. *Nature*, **284**, 155-157.

Dettinger, M.D. and M. Ghil, 1998: Seasonal and interannual variations of atmospheric CO_2 and climate. *Tellus*, **50B**, 1-24.

Elliot, W.P., J.K. Angell, and K.W. Thoning, 1991: Relation of atmospheric CO_2 to tropical sea and air temperatures and precipitation. *Tellus*, **43B**, 144-155.

Enting, I., 2002: Inverse Problems in Atmospheric Constituent Transport. Cambridge University Press, Cambridge, U.K.

Feely, R.A., R.H. Gammon, B.A. Taft, P.E. Pullen, L.S. Waterman, T.J. Conway, J.F. Gendron, and D.P. Wisegarver, 1987: Distribution of chemical tracers in the Eastern Equatorial Pacific during and after the 1982-1983 El Niño/Southern Oscillation Event. *J. of Geophys. Res.*, **92**, 6545-6558.

Feely, R.A., R.Wanninkhof, T. Takahashi, and P. Tans, 1999: Influence of El Niño on the equatorial Pacific contribution to atmospheric CO_2 accumulation. *Nature*, **398**, 597-601.

Feely, R.A., C.L. Sabine, T. Takahashi, and R. Wanninkhof, 2001: Uptake and storage of carbon dioxide in the ocean: the global CO_2 survey. *Oceanography*, **14**, 18-32.

Feldstein, S.B., 2000: The timescale, power spectra, and climate noise properties of teleconnection patterns. *J. Climate*, **13**, 4430-4440.

Fyfe, J.C., G.J. Boer, and G.M. Flato, 1999: The Arctic and Antarctic Oscillations and their projected changes under global warming. *Geophys. Res. Lett.*, **26**, 1601-1604.

GLOBALVIEW-CO_2, 2004: Cooperative Atmospheric Data Integration Project - Carbon Dioxide. CD-ROM, NOAA CMDL, Boulder, Colorado (Also available on Internet via anonymous FTP to ftp.cmdl.noaa.gov, Path: ccg/co2/GLOBALVIEW).

Gong, D. and S. Wang, 1999: Definition of Antarctic Oscillation index. *Geophys. Res. Lett.*, **26**, 459-462.

Gu, L., D.D. Baldocchi, S.C. Wofsy, J.W. Munger, J.J. Michalsky, S.P. Urbanski, and T.A. Boden, 2003: Response of a deciduous forest to the Mount Pinatubo eruption: enhanced photosynthesis. *Science*, **299**, 2035-2038.

Gurney, K.R., R.M. Law, A.S. Denning, P.J. Rayner, D. Baker, P. Bousquet, L. Bruhwiler, Y.-H. Chen, P. Ciais, S. Fan, I.Y. Fung, M. Gloor, M. Heimann, K. Higuchi, J. John, T. Maki, S. Maksyutov, K. Masarie, P. Peylin, M. Prather, B.C. Pak, J. Randerson, J. Sarmiento, S. Taguchi, T. Takahashi, and C.-W. Yuen, 2002: : Towards robust regional estimates of CO_2 sources and sinks using atmospheric transport models. *Nature*, **415**, 626-630.

Gurney, K.R., R.M. Law, A.S. Denning, P.J. Rayner, D. Baker, P. Bousquet, L. Bruhwiler, Y.-H. Chen, P. Ciais, S. Fan, I.Y. Fung, M. Gloor, M. Heimann, K. Higuchi, J. John, E. Kowalczyk, T. Maki, S. Maksyutov, P. Peylin, M. Prather, B.C. Pak, J. Sarmiento, S. Taguchi, T. Takahashi, and C.-W. Yuen, 2003: TransCom3 CO_2 inversion intercomparison: 1. Annual mean control results and sensitivity to transport and prior flux information. *Tellus*, **55B**, 555-579.

Gurney, K.R., R.M. Law, A.S. Denning, P.J. Rayner, B.C. Pak, D. Baker, P. Bousquet, L. Bruhwiler, Y.-H. Chen, P. Ciais, I.Y. Fung, M. Heimann, J. John, T. Maki, S. Maksyutov, P. Peylin, M. Prather, and S. Taguchi, 2004: Transcom3 inversion intercomparison: model mean results for the estimation of seasonal carbon sources and sinks. *Glob. Biogeochem. Cycles*, **18**, GB1010, doi:10.1029/2003GB002111.

Gurney, K.R., Y.-H. Chen, T. Maki, S. Randy Kawa, A. Andrews, and Z. Zhu, 2005: Sensitivity of atmospheric CO_2 inversions to seasonal interannual variations in fossil fuel emissions. *J. Geophys. Res.*, **110**, D10308, doi:10.1029/2004JD005373.

Hall, A. and M. Visbeck, 2002: Synchronous variability in the Southern Hemisphere atmosphere, sea ice, and ocean resulting from the annular mode. *J. Climate*, **15**, 3043-3057.

Hartmann, D.L., 1994: Global Physical Climatology. 397 pp., Academic Press, London.

Hartmann, D.L. and F. Lo, 1998: Wave-driven zonal flow vacillation in the Southern Hemisphere. *J. Atmos. Sci.*, **55**, 1303-1315.

Harvey, L.D.D., 2000: Climate and Global Environmental Change. 240 pp., Pearson Education Ltd., United Kingdom.

Heimann, M., C.D. Keeling, and C.J. Tucker, 1989: A three-dimensional model of atmospheric CO_2 transport based on observed winds, 3, Seasonal cycle and synoptic time scale variations, in Aspects of Climate Variability in the Pacific and the Western Americas. *Geophys. Monogr. 55*, edited by D.H. Peterson, 363 pp., AGU, Washington, D.C.

Horel, J.D. and J.M. Wallace, 1981: Planetary-scale atmospheric phenomena associated with the Southern Oscillation. *Monthly Weather Review*, **109**, 813-829.

Hoskins, B.J. and D.J. Karoly, 1981: The steady linear response of a spherical atmosphere in thermal and orographic forcing. *J. Atmos. Sci.*, **38**, 1179-1196.

Houghton, R.A., 2003: Revised estimates of the annual net flux of carbon to the atmosphere from changes in land use and land management 1850-2000. *Tellus*, **55B**, 378-390.

Hurrell, J.W., 1995: Decadal trends in the North Atlantic Oscillation region temperatures and precipitation. *Science*, **269**, 676-679.

Intergovernmental Panel on Climate Change, 2001.

Jones, C.D. and P.M. Cox, 2001: Modeling the volcanic signal in the atmospheric CO_2 record. *Glob. Biogeochem. Cycles*, **15**, 453-465.

Jones, C.D., M. Collins, P.M. Cox, and S.A. Spall, 2001: The carbon cycle response to ENSO: A coupled climate- carbon cycle model study. *J. Climate*, **14**, 4113-4129.

Joos, F., I.C. Prentice, and J.I. House, 2002: Growth enhancement due to global atmospheric change as predicted by terrestrial ecosystem models: consistent with U.S. forest inventory data. *Global Change Biology*, **8**, 299-303.

Kalnay, E., M. Kanamitsu, R. Kistler, W. Collins, D. Deaven, L. Gandin, M. Iredell, S. Saha, G. White, J. Woollen, Y. Zhu, M. Chelliah, W. Ebisuzaki, W. Higgins, J. Janowiak, K.C. Mo, C. Ropelewski, J. Wang, A. Leetmaa, R. Reynolds, R. Jenne, and D. Joseph, 1996: The NCEP/NCAR 40-Year Reanalysis Project. *Bulletin of the American Meteorological Society*, **77**, 437-471.

Keeling, C.D. and R. Revelle, 1985: Effects of El Niño/Southern Oscillation on the atmospheric content of carbon dioxide. *Meteoritics*, **20**, 437-450.

Keeling, C.D., R.B. Bacastow, A.F. Carter, S.C. Piper, T.P. Whorf, M. Heimann, W.G. Mook, and H. Roeloffzen, 1989: A three-dimensional model of atmospheric CO_2

transport based on observed winds, 1, Analysis of observational data, in Aspects of Climate Variability in the Pacific and the Western Americas. *Geophys. Monogr. 55*, edited by D.H. Peterson, 363 pp., AGU, Washington, D.C.

Keeling, C.D. and S.R. Shertz, 1992: Seasonal and interannual variations in atmospheric oxygen and implications for the global carbon cycle. *Nature*, **358**, 723-727.

Keeling, C.D., J.F.S. Chin, and T.P. Whorf, 1996: Increased activity of northern vegetation inferred from atmospheric CO_2 measurements. *Nature*, **382**, 146-149.

Komhyr, W.D., L.S. Waterman, and W.R. Taylor, 1983: Semiautomatic nondispersive infrared analyzer apparatus for CO_2 air sample analyses. *J. Geophys. Res.*, **88**, 1315-1322.

Le Quere, C., J.C. Orr, P. Monfray, and O. Aumont, 2000: Interannual variability of the oceanic sink of CO_2 from 1979 through 1997. *Glob. Biogeochem. Cycles*, **14**, 1247-1265.

Le Quere, C., O. Aumont, L. Bopp, ,P. Bousquet, P. Ciais, R. Francey, M. Heimann, C.D. Keeling, R.F. Keeling, H. Kheshgi, P. Peyline, S.C. Piper, I.C. Prentice, and P.J. Rayner, 2003: Two decades of ocean CO_2 sink and variability. *Tellus*, **55B**, 649-656.

Lefebvre, W., H. Goosse, R. Timmermann, and T. Fichefet, 2004: Influence of the Southern Annular Mode on the sea ice-ocean system. *J. Geophys. Research*, **109**, C09005, doi:10.1029/2004JC002403.

Lorentz, D.J. and D.L. Hartmann, 2001: Eddy-zonal flow feedback in the Southern Hemisphere. *J. Atmos. Sci.,* **58**, 3312-3327.

Lorentz, D.J. and D.L. Hartmann, 2003: Eddy-zonal flow feedback in the Northern Hemisphere winter. *J. Climate*, **16**, 1212-1227.

Lovenduski, N.S. and Gruber, N., 2005: The impact of the Southern Annular Mode on southern ocean circulation and biology. *Geophys. Res. Lett.*, **32**, doi:10.1029/2005GL022727.

Lucht, W., I.C. Prentice, R.B. Myneni, S. Sitch, P. Friedlingstein, W. Cramer, P. Bousquet, W. Buermann, and B. Smith, 2002: Climatic control of the high-latitude vegetation greening trend and Pinatubo effect. *Science*, **296**, 1687-1689.

Machta, L., 1972: Mauna Loa and global trends in air quality. *Bulletin American Meteorological Society*, **53**, 402-420.

Masarie, K.A. and P.P. Tans, 1995: Extension and integration of atmospheric carbon dioxide data into a globally consistent measurement record. *J. Geophys. Res.*, **100**, 11593-11610.

Myneni, R.B., C.D. Keeling, C.J. Tucker, G. Asrar, and R.R. Nemani. 1997: Increased plant growth in the northern high latitudes from 1981 to 1991. *Nature*, **386**, 698-702.

National Oceanic and Atmospheric Administration (NOAA), Carbon Monitoring and Diagnostics Laboratory (CMDL), Carbon Cycle Greenhouse Gases group (CCGG), Update Notes, version 2003-12-01.1518, correspondence to Pieter P. Tans and Thomas J. Conway.

National Oceanic and Atmospheric Administration (NOAA)/National Weather Service (NWS), National Centers for Environmental Prediction (NCEP), Climate Prediction Center (CPC), Teleconnection Pattern Calculation Procedures, http://www.cpc.ncep.noaa.gov/products/precip/CWlink/daily_ao_index/history/method.shtml.

Oren, R., D.S. Ellsworth, K.H. Johnsen, N. Phillips, B.E. Ewers, C. Maier, K. Schafer, H. McCarthy, G. Hendrey, S.G. McNulty, and G.G. Katul, 2001: Soil fertility limits carbon sequestration by forest ecosystems in a CO_2-enriched atmosphere. *Nature*, **411**, 469-472.

Pacala, S.W., G.C. Hurtt, D. Baker, P. Peylin, R.A. Houghton, R.A. Birdsey, L. Heath, E.T. Sundquist, R.F. Stallard, P. Ciais, P. Moorcroft, J.P. Caspersen, E. Shevliakova, B. Moore, G. Kohlmaier, E. Holland, M. Gloor, M.E. Harmon, S.M. Fan, J.L. Sarmiento, C.L. Goodale, D. Schimel, and C.B. Field, 2001: Consistent land- and atmosphere- based U.S. carbon sink estimates. *Science*, **292**, 2316-2320.

Patra, P.K., M. Ishizawa, S. Maksyutov, and G. Inoue, 2005: Role of biomass burning and climate anomalies for land-atmosphere carbon fluxes based on inverse modeling of atmospheric CO_2. *Glob. Biogeochem. Cycles*, **19**, GB3005, doi:10.1029/2004GB002258.

Philander, S.G., 1990: El Niño, La Niña, and the Southern Oscillation. American Press, Inc.

Rasmusson, E.M., 1985: El Niño and variations in climate. *American Scientist*, **73**, 168-177.

Rayner, P.J., R.M. Law, and R.Dargaville, 1999: The relationship between tropical CO_2 fluxes and the El Niño-Southern Oscillation. *Geophys. Res. Letters*, **26**, 493-496.

Robinson, W.A., 2000: A baroclinic mechanism for the eddy feedback on the zonal index. *J. Atmos. Sci.*, **57**, 415-422.

Rodenbeck, C., S. Houwelling, M. Gloor, and M. Heimann, 2003: CO_2 flux history 1982-2001 inferred from atmospheric data using a global inversion of atmospheric transport. *Atmos. Chem. Phys. Discuss.*, **3**, 2575-2659.

Roy, T., P. Rayner, R. Matear, and R. Francey, 2003: Southern hemisphere ocean CO_2 uptake: reconciling atmospheric and oceanic estimates. *Tellus*, **55B**, 701-710.

Russell, J.L., and J.M. Wallace, 2004: Annual carbon dioxide drawdown and the Northern Annular Mode. *Glob. Biogeochem. Cycles*, **18**, GB1012, doi:10.1029/2003GB002044.

Russell, J.L., and J.M. Wallace, 2005: On the nature and causes of year-to-year variability in the carbon cycle. *Glob. Biogeochem. Cycles,* in review.

Sarmiento, J.L. and N. Gruber, 2002: Sinks for anthropogenic carbon. *Physics Today*, 30-36.

Schaefer, K., A.S. Denning, N. Suits, J. Kaduk, I. Baker, S. Los, and L. Prihodko, 2002: Effect of climate on interannual variability of terrestrial CO_2 fluxes. *Glob. Biogeochem. Cycles*, **16**, GB1102, doi:10.1029/2002GB001928.

Shindell, D.T., R.L. Miller, G.A. Schmidt, and L. Pandolfo, 1999: Simulation of recent northern winter climate trends by greenhouse-gas forcing. *Nature*, **399**, 452-455.

Shindell, D.T. and G.A. Schmidt, 2004: Southern hemisphere climate response to ozone changes and greenhouse gas increases. *Geophys. Res. Lett.*, **31**, L18209, doi:10.1029/2004GL020724.

Siegenthaler, U., 1990: El Niño and atmospheric CO_2. *Nature*, **345**, 295-296.

Tans, P.P., I.Y. Fung, and T. Takahashi, 1990: Observational constraints on the global atmospheric CO_2 budget. *Science*, **247**, 1431-1438.

Thompson, D.W.J and J.M. Wallace, 1998: The Arctic Oscillation signature in the wintertime geopotential height and temperature fields. *Geophys. Res. Lett.*, **25**, 1297-1300.

Thompson, D.W.J. and J.M. Wallace, 2000: Annular modes in the extratropical circulation: I. Month-to-month variability. *J. Climate*, **13**, 1000-1016.

Thompson, D.W.J., J.M. Wallace, and G.C. Hegerl, 2000: Annular modes in the extratropical circulation: II. Trends. *J. Climate*, **13**, 1018-1036.

Thompson, D.W.J. and J.M. Wallace, 2001: Regional climate impacts of the Northern Hemisphere Annular Mode. *Science*, **293**, 85-89.

Thompson, D.W.J. and S. Solomon, 2002: Interpretation of recent Southern Hemisphere climate change. *Science*, **296**, 895-899.

Thoning, K.W., P.P. Tans, and W.D. Komhyr, 1989: Atmospheric carbon dioxide at Mauna Loa Observatory 2. Analysis of the NOAA GMCC data, 1974-1985. *J. Geophys. Res.*, **94**, 8549-8565.

Thoning, K.W., P. Tans, T.J. Conway, and L.S. Waterman, 1987: NOAA/GMCC calibrations of CO_2-in-air reference gases: 1979-1985. NOAA Tech. Memo. (ERL ARL-150). Environmental Research Laboratories, Boulder, CO., 63 pp.

Thorncroft, C.D., B.J. Hoskins, and M.E. McIntyre, 1993: Two paradigms of baroclinic wave life-cycle behaviour. *Q.J.R. Meteorol. Soc.*, **119**, 17-55.

Toggweiler, J.R., J.L. Russell, and S.R. Carson, in review: The mid-latitude westerlies, atmospheric CO_2, and climate change during the Ice Ages. *Paleoceanography*, submitted.

Trenberth, K.E., 1976: Spatial and temporal variations in the Southern Oscillation. *Quart. J. Royal Meteorol. Soc.*, **102**, 639-653.

Tucker, C.J., 1980: Remote sensing of leaf water content in the near infrared. *Remote Sensing of Environment*, **10**, 23-32.

Tucker, C.J., J. E. Pinzon, M.E. Brown, D. Slayback, E. W. Pak, R. Mahoney, E. Vermote, and N. El Saleous, 2005: An extended AVHRR 8-km NDVI data set compatible with MODIS and SPOT vegetation NDVI data. *International Journal of Remote Sensing*, in press.

Vitousek, P.M., J.D. Aber, R.W. Howarth, G.E. Likens, P.A. Matson, D.W. Schindler, W.H. Schlesinger, and D.G. Tilman, 1997: Human alteration of the global nitrogen cycle: sources and consequences. *Ecological Applications*, **7**, 737-750.

Wallace, J. M., 2000: On the Arctic and Antarctic Oscillations. Lecture at the 2000 NCAR ASP Summer Colloquium on the Dynamics of Decadal to Centennial Climate Variability. Edited by Eric DeWeaver and Michael Palmer.

Wanninkhof, R. and W.R. McGillis, 1999: A cubic relationship between air-sea CO_2 exchange and wind speed. *Geophys. Res. Letters*, **26**, 1889-1892.

Winguth, A., M. Heimann, K.D. Kurz, E. Maier-Reimer, U. Mikolajewicz, and J. Segschneider, 1994: El Niño-Southern Oscillation related fluctuations of the marine carbon cycle. *Glob. Biogeochem. Cycles*, **8**, 39-63.

Yang, X. and M. Wang, 2000: Monsoon ecosystems control on atmospheric CO_2 interannual variability: inferred from a significant positive correlation between year-to-year changes in land precipitation and atmospheric CO_2 growth rate. *Geophys. Res. Letters*, **27**, 1671-1674.

Zhao, C.L., P.P. Tans, and K.W. Thoning, 1997: A high precision manometric system for absolute calibrations of CO_2 in dry air. *J. Geophys. Res.*, **102**, 5885-5894.